

**Bioorthogonal labeling of neuronal proteins
using super-resolution fluorescence microscopy**



Doctoral thesis for a doctoral degree
at the Julius-Maximilians-Universität Würzburg

submitted by

Alexander Kuhlemann

from Bamberg

Würzburg, 2021

Submitted on:

.....

Office stamp

Members of the Thesis Committee

Chairperson:

.....

Primary Supervisor: Prof. Dr. Markus Sauer

Supervisor (Second): Prof. Dr. Anna-Leena Siren

Supervisor (Third): PD Dr. Sören Doose

Date of Public Defence:

Date of Receipt of Certificates:

Abstract

The synaptic cleft is of central importance for synaptic transmission, neuronal plasticity and memory and thus well studied in neurobiology. To target proteins of interest with high specificity and strong signal to noise conventional immunohistochemistry relies on the use of fluorescently labeled antibodies. However, investigations on synaptic receptors remain challenging due to the defined size of the synaptic cleft of ~20 nm between opposing pre- and postsynaptic membranes. At this limited space, antibodies bear unwanted side effects such as crosslinking, accessibility issues and a considerable linkage error between fluorophore and target of ~10 nm. With recent single molecule localization microscopy (SMLM) methods enabling localization precisions of a few nanometers, the demand for labeling approaches with minimal linkage error and reliable recognition of the target molecules rises.

Within the scope of this work, different labeling techniques for super-resolution fluorescence microscopy were utilized allowing site-specific labeling of a single amino acid in synaptic proteins like kainate receptors (KARs), transmembrane α -amino-3-hydroxy-5-methyl-4-isoxazolepropionic acid receptor regulatory proteins (TARPs), γ -aminobutyric acid type A receptors (GABA-ARs) and neuroligin 2 (NL2). The method exploits the incorporation of unnatural amino acids (uAAs) in the protein of interest using genetic code expansion (GCE) via amber suppression technology and subsequent labeling with tetrazine functionalized fluorophores. Implementing this technique, hard-to-target proteins such as KARs, TARPs and GABA-ARs could be labeled successfully, which could only be imaged insufficiently with conventional labeling approaches. Furthermore, functional studies involving electrophysiological characterization, as well as FRAP and FRET experiments validated that incorporation of uAAs maintains the native character of the targeted proteins. Next, the method was transferred into primary hippocampal neurons and in combination with super-resolution microscopy it was possible to resolve the nanoscale organization of γ 2 and γ 8 TARPs. Cluster analysis of *d*STORM localization data verified synaptic accumulation of γ 2, while γ 8 was homogeneously distributed along the neuron. Additionally, GCE and bioorthogonal labeling allowed visualization of clickable GABA-A receptors located at postsynaptic compartments in dissociated hippocampal neurons. Moreover, saturation experiments and FRET imaging of clickable multimeric receptors revealed successful binding of multiple tetrazine functionalized fluorophores to uAA-modified dimeric GABA-AR α 2 subunits in close proximity (~5 nm). Further utilization of tetrazine-dyes via super-resolution microscopy methods such as *d*STORM and click-ExM will provide insights to subunit arrangement in receptors in the future.

This work investigated the nanoscale organization of synaptic proteins with minimal linkage error enabling new insights into receptor assembly, trafficking and recycling, as well as protein-protein interactions at synapses. Ultimately, bioorthogonal labeling can help to understand pathologies such as the limbic encephalitis associated with GABA-AR autoantibodies and is already in application for cancer therapies.

Zusammenfassung

Der synaptische Spalt ist von zentraler Bedeutung für die synaptische Reizweiterleitung, neuronale Plastizität und Gedächtnis und dadurch neurobiologisch sehr gut charakterisiert. Um Zielproteine mit hoher Spezifität und einem guten Signal-zu-Rauschen Verhältnis zu adressieren, wird konventionell auf Immunhistochemie mittels Fluoreszenzfarbstoff-markierter Antikörper zurückgegriffen. Untersuchungen synaptischer Rezeptoren bleiben dabei jedoch aufgrund der limitierten Zugänglichkeit des synaptischen Spalts mit einem Abstand von ~ 20 nm zwischen gegenüberliegenden pre- und postsynaptischen Membranen herausfordernd. Speziell in einem räumlich begrenzten Umfeld können bei der Verwendung von Antikörpern unerwünschte Artefakte auftreten, die durch Kreuzverlinkung, eine verminderte Zugänglichkeit und einen erheblichen Markierungsabstand zwischen Fluorophor und Probe von ~ 10 nm entstehen. Aktuelle Verfahren der Einzelmolekül-Lokalisations-Mikroskopie (SMLM), die eine Lokalisationsgenauigkeit von wenigen Nanometern ermöglichen, erhöhen die Nachfrage an Markierungsstrategien mit minimalem Markierungsabstand und zuverlässiger Erkennung der Zielstruktur.

Im Rahmen dieser Arbeit wurden daher verschiedene Markierungsmethoden für die hochauflösende Fluoreszenz-Mikroskopie erprobt. Dies ermöglichte die ortsspezifische Markierung einer einzigen Aminosäure in synaptischen Proteinen wie Kainat-Rezeptoren (KARs), Transmembran- α -Amino-3-hydroxy-5-methyl-4-isoxazol-Propionsäure-Rezeptor regulierenden Proteinen (TARPs), γ -Aminobuttersäure-Typ-A-Rezeptoren (GABA-ARs) oder Neuroligin 2 (NL2). Die angewandte Methodik nutzt den Einbau von unnatürlichen Aminosäuren (uAAs) in das Zielprotein mittels Erweiterung des genetischen Codes (GCE) durch Unterdrückung des Amber-Stop-Codons. Durch Anwendung dieser Strategie gelang es, schwer adressierbare Proteine wie KARs, TARPs und GABA-ARs, welche zuvor mittels konventioneller Markierungsversuche nur unzureichend abgebildet werden konnten, erfolgreich zu markieren. Funktionelle Studien wie elektrophysiologische Charakterisierungen, aber auch FRAP und FRET Experimente zeigten, dass dabei der native Zustand der Zielproteine auch nach dem Einbau von uAAs erhalten bleibt. Schließlich wurde die Methode in primäre hippocampale Neuronen überführt und in Kombination mit hochauflösender Mikroskopie konnte die Organisation von $\gamma 2$ und $\gamma 8$ TARPs im Nanobereich aufgelöst werden. Eine Cluster-Analyse von *d*STORM Lokalisationsdaten bestätigte die Anreicherung von $\gamma 2$ in Synapsen, während $\gamma 8$ homogen entlang des Neurons verteilt vorliegt. Die Erweiterung des genetischen Codes in Kombination mit bioorthogonaler Markierung erlaubte zusätzlich die Visualisierung

von clickbaren GABA-A Rezeptoren in Postsynapsen von dissoziierten hippocampalen Neuronen. Außerdem zeigten Saturierungs-Experimente und FRET-Bildgebung die erfolgreiche Bindung von mehreren Tetrazin-gekoppelten Fluorophoren an uAA-modifizierten, dimerischen GABA-AR $\alpha 2$ -Untereinheiten in geringem Abstand (~5 nm). Auf der Basis dieser Resultate werden zukünftig hochauflösende mikroskopische Verfahren, wie *d*STORM und click-ExM, in Kombination mit Tetrazin-Farbstoffen die Visualisierung von multimerischen Rezeptoren ermöglichen.

Im Rahmen dieser Arbeit konnte die Organisation von synaptischen Proteinen mit minimalem Markierungsabstand im Nanobereich untersucht werden und dadurch neue Einsichten in Rezeptor-Zusammenbau, -Bewegungen und -Wiederverwertung, aber auch Protein-Protein Interaktionen in Synapsen gewonnen werden. Die Weiterentwicklung bioorthogonaler Markierungsstrategien kann in Zukunft dazu beitragen Krankheiten, wie die Limbische Enzephalitis, welche mit GABA-AR Autoantikörpern in Verbindung steht, besser zu verstehen und findet zudem bereits heute Anwendung in Krebstherapien.

Contents

| | |
|--|------------|
| Abstract | i |
| Zusammenfassung | iii |
| 1 Introduction | 1 |
| 1.1 Neuronal organization | 1 |
| 1.2 Structure of synaptic receptors | 2 |
| 1.3 Labeling strategies in neuroscience..... | 4 |
| 2 Theoretical background | 8 |
| 2.1 Synaptic proteins | 8 |
| 2.1.1 Excitatory synapses | 8 |
| 2.1.2 Inhibitory synapses | 12 |
| 2.2 Labeling methods | 14 |
| 2.2.1 Fluorescent proteins..... | 14 |
| 2.2.2 Organic dyes | 15 |
| 2.2.3 Immunostaining | 16 |
| 2.2.4 Genetic code expansion and bioorthogonal click chemistry | 17 |
| 2.3 Fluorescence and Microscopy | 20 |
| 2.3.1 Excitation and Emission | 20 |
| 2.3.2 Confocal laser scanning microscopy (CLSM)..... | 20 |
| 2.3.3 Super-resolution fluorescence microscopy | 21 |
| 2.3.4 Expansion microscopy..... | 23 |
| 3 Materials and Methods | 25 |
| 3.1 Chemicals, buffers and consumables | 25 |
| 3.2 Labeling reagents | 27 |
| 3.3 Enzymes | 29 |
| 3.4 DNA constructs | 29 |
| 3.5 Mammalian and neuronal cell culture | 31 |
| 3.6 Laboratory devices | 32 |
| 3.7 Software | 32 |

| | | |
|----------|---|-----------|
| 3.8 | Methods for mutagenesis and amplification of plasmids | 32 |
| 3.9 | Fluorescence labeling methods | 36 |
| 3.10 | Microscopy setups | 37 |
| 3.11 | Click-Expansion microscopy (click-ExM) | 38 |
| 3.12 | Conjugation of tetrazines or antibodies..... | 38 |
| 3.13 | Data analysis | 39 |
| 4 | Results and Discussion | 40 |
| 4.1 | Bioorthogonal click chemistry visualizes ionotropic kainate receptors (KARs)..... | 40 |
| 4.1.1 | Establishment of clickable KAR GluK2 subunits in mammalian cells | 40 |
| 4.1.2 | Comparison of bioorthogonal labeling with antibody labeling | 42 |
| 4.1.3 | Discussion on bioorthogonal labeling of clickable KARs..... | 44 |
| 4.2 | Bioorthogonal click chemistry visualizes TARPs..... | 45 |
| 4.2.1 | Immunohistochemistry of $\gamma 2$ and $\gamma 8$ TARPs in mammalian and neuronal cells..... | 45 |
| 4.2.2 | Establishment of clickable $\gamma 2$ and $\gamma 8$ TARPs in mammalian cells..... | 48 |
| 4.2.3 | GCE and bioorthogonal labeling of clickable TARPs in neurons | 51 |
| 4.2.4 | <i>d</i> STORM imaging and cluster analysis of clickable TARPs in neurons | 52 |
| 4.2.5 | Discussion on clickable $\gamma 2$ and $\gamma 8$ TARPs | 57 |
| 4.3 | Visualization of clickable ionotropic GABA-A receptors and Neuroligin 2 | 58 |
| 4.3.1 | Establishment of clickable $\alpha 1$ and $\alpha 2$ GABA-A receptors in mammalian cells..... | 58 |
| 4.3.2 | Functional analysis of clickable $\alpha 2^{\text{S181TAG}}$ GABA-A receptors..... | 63 |
| 4.3.3 | Visualizing clickable $\alpha 2^{\text{S181TAG}}$ GABA-A receptors in neurons | 65 |
| 4.3.4 | GCE and bioorthogonal labeling of NL2..... | 66 |
| 4.3.5 | Discussion on clickable GABA-A receptors and NL2 | 67 |
| 4.4 | Visualizing clickable dimeric receptors | 70 |
| 4.4.1 | Application of click chemistry to reveal receptor composition..... | 70 |
| 4.4.2 | Single molecule localization microscopy <i>d</i> STORM | 73 |
| 4.4.3 | Click chemistry combined with expansion microscopy | 74 |
| 4.4.4 | Discussion on visualization of monomeric and dimeric receptors | 75 |
| 5 | Conclusion and Outlook | 79 |
| 5.1 | Bioorthogonal labeling of hard-to-access proteins..... | 79 |

| | | |
|----------|---|------------|
| 5.2 | Bioorthogonal labeling to study protein-protein interactions..... | 79 |
| 5.3 | Bioorthogonal labeling to advance trafficking approaches..... | 80 |
| 5.4 | Optimization of bioorthogonal labeling in neuronal cultures..... | 81 |
| 5.5 | Advancing click chemistry to investigate multimeric receptors | 83 |
| 5.6 | Bioorthogonal labeling to tackle pathologies..... | 85 |
| 6 | References | 87 |
| 7 | Appendix | 104 |
| | List of primers | 104 |
| | List of abbreviations..... | 107 |
| | List of publications | 110 |
| | Acknowledgements..... | 111 |
| | Affidavit..... | 112 |
| | Curriculum Vitae | 113 |

1 Introduction

1.1 Neuronal organization

Brain functions involving memory, learning and cognition rely on the communication between neurons along synapses. To communicate, presynaptic neurons release neurotransmitters leading to activation of postsynaptic ionotropic receptors hence conveying excitatory or inhibitory transmission (Figure 1). The most abundant excitatory neurotransmitter glutamate can activate three glutamate receptor families known as α -amino-3-hydroxy-5-methyl-4-isoxazolepropionic acid receptors (AMPA), kainate receptors (KAR) and *N*-Methyl-D-aspartate receptors (NMDAR), whereas the inhibitory neurotransmitters Glycine and GABA control corresponding Glycine and GABA receptors in inhibitory synapses^{1,2}. Persistent activation of synapses is known to induce long term potentiation (LTP) and is associated with learning and memory³. In the central nervous system (CNS) balancing of LTP and its counterpart long term depression (LTD), the continuous weakening of synapses, is crucial to maintain proper brain function⁴. Mechanisms contributing to LTP and LTD include efficacy of neurotransmitter release at the presynapse^{5,6}, biophysical changes of postsynaptic receptors such as conductance and variation of open probability^{7,8}. Additionally, the localization of postsynaptic receptors is affected by lateral diffusion and constant recycling of receptors by exo- and endocytotic processes⁹⁻¹¹ (Figure 1). Compared to highly mobile receptors in extrasynaptic regions, thermal agitation and attachment to stable scaffold and cytoskeletal or extracellular anchoring compartments lead to reversible immobilization and trapping of receptors at synapses¹². Moreover, scaffolding elements and neurotransmitter receptors are not randomly diffusing in the synapses, but are rather organized in stable nanodomains including options to concentrate or disperse receptors by lateral diffusion¹³⁻¹⁵. The synapse is a highly dynamic space, which requires precise coordination between presynaptic release machinery, postsynaptic scaffolds, receptors, cytoskeletal compartments and transsynaptic adhesion proteins to pursue synaptic formation and ultimately function¹². Since variations in the diffusional behavior of synaptic receptors could be linked to pathological conditions¹⁶⁻¹⁸, the modulation of receptor diffusion and hence, synaptic transmission and plasticity via pharmaceutical reagents offers a major opportunity for novel treatment approaches^{19,20}.

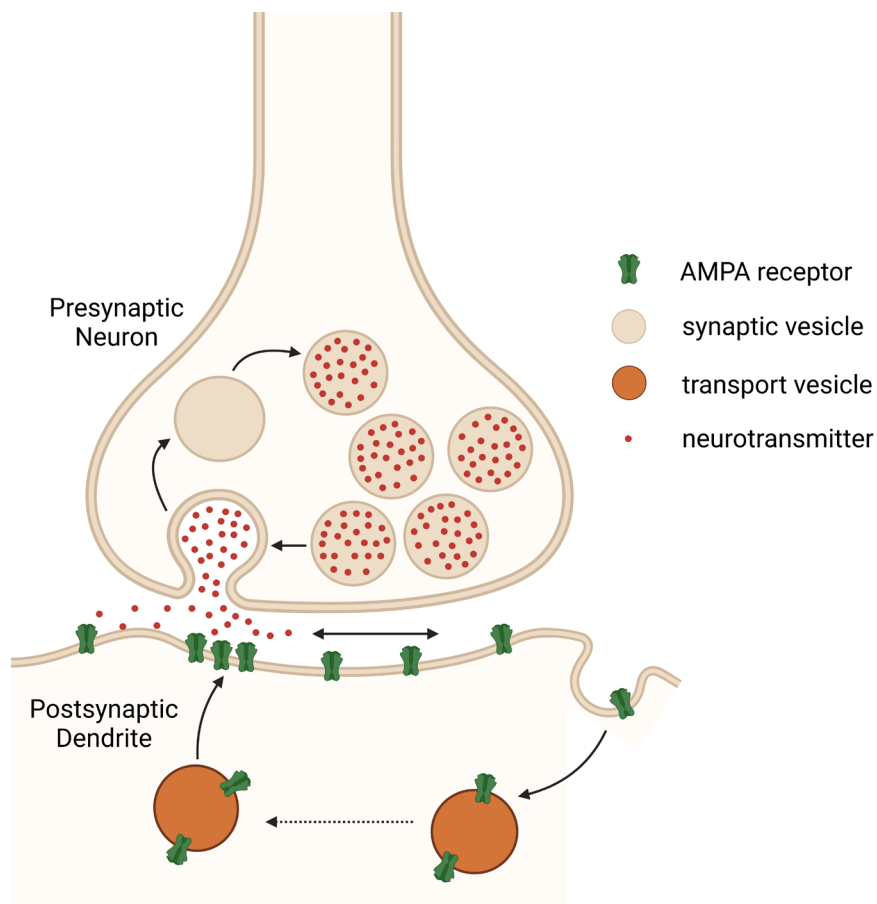


Figure 1 - Simplified view of postsynaptic AMPARs at excitatory synapses. Fusion of presynaptic vesicles with the presynaptic membrane induce neurotransmitter release into the synaptic cleft. Binding of neurotransmitters to postsynaptic receptors triggers postsynaptic signal transmission and promotes exocytosis of new AMPA receptors into the postsynaptic membrane to increase number of receptors and inducing LTP. Vice versa, highly mobile AMPARs diffuse to extra-synaptic sites for endocytosis culminating in LTD. Created with BioRender.com.

1.2 Structure of synaptic receptors

iGluRs. Ionotropic glutamate receptors (iGluRs) function as ion channels for inducing postsynaptic membrane depolarisation in excitatory synapses and, hence, play a critical role in synaptic transmission. All three types of glutamate receptors (AMPA, NMDA and KAR) are composed of an extracellular amino-terminal domain (ATD), a ligand-binding domain (LBD), a trans-membrane domain (TMD) and an intracellular signaling domain (CTD)²¹. The TMD exhibits a four-fold symmetry, whereas the ATDs form dimer of dimers connected via peptide linkers²². The ATD is essential for assembly, trafficking and function of the receptors^{21,23}. KAR and AMPAR ATDs interact through several interfaces and enable tight dimers which are generally separated from the LBD region²⁴. The connection between ATD dimers can be either robust as known for KARs^{25,26} or can be ruptured upon desensitization in

AMPA²⁷. Additionally, KARs exhibit a tetrameric symmetry in the LBD^{26,28} in contrast to the twofold symmetric assembly of the LBD as found in AMPAR²⁹. The LBD layer is located below the ATD providing binding sites to activate, modulate or antagonize the membrane receptor³⁰. Each dimer pair forms a clamshell structure in the LBD, that allows ligand binding in between the lobes and subsequent channel opening mediated by the TMD³¹. The TMD itself consists of three transmembrane helices and an intracellular loop, which reacts to conformational changes in the LBD via flexible polypeptide linkers³¹. Auxiliary subunits binding to AMPARs can either support receptor signaling like transmembrane AMPA regulatory proteins (TARPs)^{29,32} or suppress receptor function such as germ cell-specific gene 1-like (GSG1L) proteins^{33,34}. Various TARP segments enhance AMPAR currents: the transmembrane region is involved in shaping conductance and rectification properties, whereas the extracellular domain is modulating the gating kinetics of the receptor. Furthermore, the C-terminal tail can fulfill both tasks mentioned above²².

GABA-ARs. In inhibitory synapses, ionotropic GABA-A receptors maintain synaptic plasticity¹. GABA-A receptors are structured as pentamers assembled from various combinations of alpha (α 1-6), beta (β 1-3), gamma (γ 1-3), rho (ρ 1-3), epsilon (ϵ), delta (δ), pi (π) and theta (θ) subunits³⁵. Cryo-EM studies revealed the structure of different pentamer compositions of GABA-A receptors such as the pre-dominant isoform in the adult brain α 1 β 2 γ 2³⁶ and the α 1 β 3 γ 2 isoform bound to pharmacological relevant modulators³⁷. All GABA-A subunits share the same topology: An extracellular domain (ECD), a transmembrane domain (TMD) and an extracellular C-terminal domain (CTD)³⁵. The extracellular domain (ECD) of the receptor is target for the neurotransmitter GABA at the β 2- α 1 interfaces and benzodiazepine derivatives at the α 1- γ 2 interface³⁸⁻⁴⁰. GABA binding induces closure of loops-C in β subunits which results in spatial approximation of α and β subunits and thus locks the binding pocket, followed by a counter-clockwise rotation (view from from the synaptic cleft) of the ECDs of all subunits^{37,41}. Conformational changes in the ECDs trigger clockwise rotation of the TMDs modulating the M2-M3 loops and opening of the channel pore³⁷. The transmembrane domain consists of four sequences (M1-M4), whereby M2 forms the chloride channel, while an intracellular loop between M3 and M4 is important for modulation by phosphorylation (M3-M4)³⁵. Interactions from GABA-A receptor associated proteins with the intracellular loop are essential for receptor trafficking as well as anchoring in the membrane or to cytoskeletal compartments^{42,43}.

1.3 Labeling strategies in neuroscience

Cryo-electron microscopy measured the distance between pre- and postsynaptic membranes of approximately 20 nm corroborating the measured size of synaptic cleft in earlier reports^{44,45}. The crowded protein environment inside synaptic clefts limits the access of labeling agents to target epitopes and resulted in the design of various new probes for imaging synaptic proteins^{46,47}. This section will provide an overview of the wide range of labeling strategies available (Figure 2) including their benefits and drawbacks and focusing on the applicability on synaptic targets.

Labeling endogenous proteins. While electron microscopy methods could visualize postsynaptic glutamate and GABA receptors with 20-30 nm precision in the past, all conventional approaches lack the opportunity to investigate living neurons and dynamics⁴⁸. Moreover, 40-nm gold nanoparticles create a considerable linkage error adding to the distance between target region and particle/fluorophore⁴⁹. As an alternative, fluorescent labeling methods allow live imaging and analysis of protein diffusion and synaptic organization. Immunohistochemistry approaches can visualize endogenous protein organization and can provide quantitative estimates of molecules in neurons. This technique utilizes fluorescently labeled primary and secondary antibodies to recognize specific amino acid sequences (epitopes) of endogenous proteins. Advances in antibody-based approaches enabled mapping of multiple compartments of primary neurons and neuronal tissue with DNA-PAINT or sequential labeling^{50,51}. On the downside, antibodies can also create artificial clusters by crosslinking and impede protein diffusion as shown for dynamics of synaptic adhesion proteins like Neuroligin 1⁵². In single-particle tracking studies, bright, fluorescent quantum dots are coupled to primary or secondary antibodies but may induce accessibility issues in the synaptic cleft due to their larger size⁵³. To reduce the linkage error between fluorophore and target and improve accessibility, methods using only parts of the antibody such as the short-chain variable fragment (scFv), the fragment of antigen binding (Fab), nanobodies and amino acid derived aptamers became popular^{54,55}. This progress allowed precise visualization of synaptic proteins like PSD95, HOMER1, α -synuclein and syntaxin 1A. However, the availability of these small binders is still limited to a few targets, making it more attractive to use nanobodies targeting primary antibodies as an alternative to secondary antibodies⁴⁷. Furthermore, small ligands decorated with fluorophores can be used to anchor a fluorophore directly to the target of interest via proximity-driven labeling reaction. Subsequent cleavage of the ligand maintain the native state of the protein⁵⁶. Although, this method allowed imaging of endogenous AMPA and opioid receptors in living neurons, its again only available for a limited number of targets and

functionality of each target receptor needs to be validated^{57,58}. As a conclusion, addressing endogenous levels of proteins is a suitable way of visualizing the native state of synapses. However, many of the approaches were developed individually for only a few targets and are, hence, limited in their application. Another labeling option is genetic incorporation of tags or genetically encode fluorophores to target proteins inside synapses.

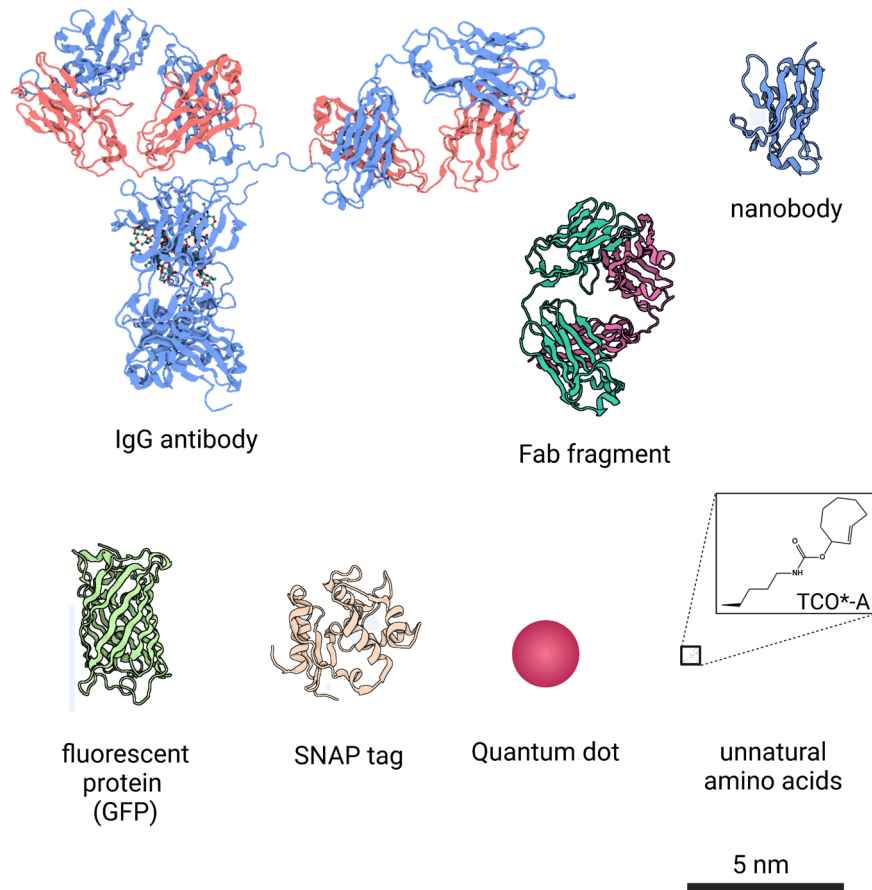


Figure 2 – Strategies to attach a fluorescent label to the target structure. Immunolabeling relies on epitope recognition via the use of IgG antibodies, Fab fragments or nanobodies. Due to their size, Fab fragments (PDB: 2ZKH) and nanobodies (PDB: 5IVO) are preferred over full-size IgG antibodies (PDB: 1HZH). Quantum dots can be conjugated to antibodies and function as fluorescent marker. Fluorescent proteins such as GFP (PDB: 1GFL) or self-labeling SNAP tags (PDB: 3KZZ) are fused to the cDNA of the target of interest. Unnatural amino acids like TCO*-K can be introduced into a protein of interest by GCE and labeled in the following with tetrazine functionalized fluorophores to enable a low linkage error between fluorophore and target. Created with BioRender.com.

Genetic modification of proteins. A common way of visualizing a protein of interest with a 1:1 stoichiometry is the genetic fusion of a fluorescent protein sequence to the cDNA sequence of the target⁴⁷. For instance, this method was applied for analyzing the trafficking of AMPA receptors at excitatory synapses⁵⁹. Constant improvement of fluorescent proteins led to a protein palette covering a wide range of the visible light spectrum with optimized folding,

oligomerization, photostability and intensity properties^{60,61}. In addition, progress on photoactivatable and photoswitchable proteins enabled use of proteins like mEos, Dendra, PA-mCherry, PS-mOrange and various others for single molecule localization microscopy (SMLM)^{62,63}. Unfortunately, large fluorescent proteins can also disturb the native conformation and function of multimeric synaptic receptors and so impede natural receptor diffusion⁵⁹. In order to provide an alternative, smaller genetic tags such as SNAP- and CLIP-tags, where self-labeling enzymes can be addressed by substrates bearing organic dyes, were established^{64,65}. Time-resolved FRET experiments using SNAP-tags gave insights into the dimeric assembly of γ -aminobutyric acid type B (GABA-B) receptors and metabotropic glutamate receptors (mGluRs)⁶⁶. A combination of CLIP and SNAP tags was also used to decipher heterotetrameric formation of ghrelin receptors (GHSR1a) with dopamine receptor 2 (DRD2) in hypothalamic neuronal cells⁶⁷. However, the bulky size of SNAP and CLIP tags with ~20 kDa needs to be considered as it may influence receptor functionality⁴⁶. Another labeling approach is the incorporation of well-established small epitope tags such as HA-, MYC-, Flag and V5-tags in the DNA sequence of the target of interest. These tags can be targeted subsequently with highly specific antibodies carrying fluorophores^{68,69}. Advances in this direction led to the innovation of the ALFA-tag, consisting of 15 amino acids, which can be labeled efficiently with nanobodies⁷⁰. Additionally, implementing an AviTag to the target of interest allows biotinylation of the protein using a bacterial biotin ligase and fluorescent labeling with monomeric streptavidin variants^{52,71}. On the downside, these strategies work under overexpressed conditions and still require antibodies, nanobodies or streptavidin to attach a fluorescent label to the target protein, which again creates a considerable linkage error between fluorescent signal and respective target. Recent labeling strategies focus on introducing single amino acids bearing functional alkene groups (e.g. trans-cyclooctene, TCO) in the target protein, which can be reacted with small tetrazine molecules coupled to fluorophores⁷². A broad range of unnatural amino acids was established for GCE and subsequent click chemistry⁷³. This technique is bioorthogonal, site-specific and offers a small linkage error, which is ideal for live cell imaging⁷⁴. Bioorthogonal click chemistry enabled visualization of NMDA receptors in the past⁷⁵. Additionally, GCE was introduced via adeno-associated viruses into the brain of a living mouse, showing expression of clickable GFP modified with uAAs⁷⁶. Thus, GCE has potential to find application in living animals and can be optimized to address proteins that are more complex. Aim of the work was to target hard-to-label synaptic proteins with bioorthogonal click chemistry to allow subsequent imaging using super-resolution fluorescence microscopy. Moreover, transferring this system into hippocampal primary neurons offers a tool to

investigate complex synaptic proteins such as TARPs and GABA-ARs in neurobiological context.

2 Theoretical background

The following section will provide a theoretical background on synaptic transmembrane proteins, basics of labeling approaches for the fluorescent microscopy and imaging methods to visualize fluorescent targets.

2.1 Synaptic proteins

2.1.1 Excitatory synapses

Synaptic transmission depends on the activation of postsynaptic ionotropic receptors by presynaptically released neurotransmitters. In excitatory synapses, the neurotransmitter glutamate binds to the ionotropic glutamate receptors AMPAR, NMDAR and KAR at the postsynaptic dendritic spines and therefore can promote different variants of synaptic plasticity⁷⁷. Auxiliary proteins from the TARPs family are crucial for AMPAR assembly and function and thus will be also introduced in this chapter^{78,79}.

AMPA receptors. AMPA receptors are responsible for nearly all fast excitatory synaptic transmission in the central nervous system (CNS) of mammals. These membrane proteins form either homo- or heteromeric assemblies of the four subunits GluA1-4^{21,80}. In the hippocampus, the predominant AMPAR tetramer comprises the GluA1-GluA2 and the GluA2-GluA3 heteromers^{81,82}, whereas the GluA4 subunit is prevalent in early developmental stages of the brain⁸³. Neuronal activation induces activation of calcium permeable NMDARs or AMPARs, followed by calcium influx that activates downstream signaling pathways including calcium/calmodulin-dependent protein kinase II (CaMKII) activation as well as trapping and recruiting of AMPA receptors to the synapse in long-term potentiation (LTP)⁸⁴⁻⁸⁶. Investigations on GluA1 receptors identified C-termini of AMPARs as main modulators of AMPAR recruiting and trafficking. Phosphorylation of GluA1 by CaMKII and attachment to postsynaptic density protein 95 (PSD95) containing PDZ domains recruits and traps GluA1-GluA2 AMPARs at synapses and hence induces LTP^{87,88}. However, knockdown and replacement studies on AMPARs could not link LTP to the particular GluA1 subunit of AMPA receptors and LTP even occurs, when all AMPA receptors are replaced with KA receptors^{89,90}. These studies indicate, that the AMPAR composition is not influencing the amount of AMPARs at synapses and sets the focus on scaffolding proteins like PSD95 as driving elements to induce LTP⁸⁰. Indeed, photoactivated localization microscopy (PALM) experiments could provide evidence for colocalization of AMPARs with nanodomains of PSD95 at the postsynapse^{13,91}, but could not identify PSD95 as the individual protein responsible for LTP⁸⁰. Nevertheless, soluble ligands like Syn-GAP were identified to interact with PSD95 and anchor receptors to

the postsynaptic density (PSD)⁹²⁻⁹⁴. Experiments investigating AMPAR dynamics and trafficking observed the following: AMPARs diffuse in the ER, are transported in vesicles along microtubules, get exocytosed to and endocytosed from the cell surface and diffuse laterally on the postsynaptic surface. All of these pathways can be modulated through neuronal activity and hence, influence the number of AMPARs at synapses^{84,94}. In this context, the biosynthesis and stabilization of AMPARs regulate the total amount of receptors in the postsynaptic membrane⁹⁴. AMPARs interact with various auxiliary proteins, which themselves bind to intracellular scaffolding elements and adhesion proteins and affect AMPAR mobility and function⁹⁵⁻⁹⁷. Due to the highly complex interactions it is still unclear how the precise mechanism for AMPAR stabilization and trapping in the membrane works⁹⁴. However, crosslinking of AMPARs in the postsynaptic membrane via neutravidin eliminates LTP, demonstrating the importance of AMPAR diffusion for initial and late phases of synaptic potentiation⁹⁸. Diffusion trapping of preexisting surface pools of AMPARs mediates immediate potentiation of synaptic transmission after neuronal stimulation, whereas exocytosis and lateral diffusion of AMPARs into synapses are required to maintain LTP^{94,99}. Contrary to LTP, AMPAR endocytosis contributes to LTD⁸⁴, driven by synaptotagmin-3 (Syt3)¹⁰⁰ and the molecular motor Myosin VI¹⁰¹. Since endocytotic sites are distributed along the dendrite, AMPA receptors need to diffuse laterally out of the synapse prior to internalization during LTD¹⁰². To guarantee efficient synaptic function in the millisecond range, AMPAR receptors need to be in close proximity to the neurotransmitter release site. This is due to two reasons: first, AMPA receptors show low affinity for glutamate and second, the glutamate concentration drops drastically 100 nm apart from the release site^{103,104}. Super-resolution imaging revealed the organization of AMPAR and PSD95 in nanoclusters of 100 nm inside the PSD^{13,91}. These cluster formations might originate from interaction of AMPAR with Syn-GAP¹⁰⁵ or auxiliary proteins¹⁰⁶. Further investigations on the organization of presynaptic release sites in respect of the postsynaptic nanoclusters revealed a transsynaptic organization between the presynaptic active zone protein RIM1 and postsynaptic PSD95¹⁰⁷. RIM1 forms complexes with the proteins Munc13 and syntaxin that contribute to presynaptic vesicle organization and fusion^{94,108}. Presynaptic neuroligins that are involved in transsynaptic nanocolumns are interacting with postsynaptic ligands such as neuroligins, LRRTMs and cerebellins¹⁰⁹. Neuroligins are able to recruit PSD95 through the PDZ domain, which leads to trapping of AMPAR¹¹⁰. This overall transsynaptic alignment of synaptic proteins increases the efficiency of neuronal transmission. Thus, dysregulation of neuroligins results in decreased co-localization between AMPAR and neuroligins and additionally between AMPAR and opposing presynaptic RIM1 clusters¹¹¹.

TARPs. As mentioned before, AMPA receptors form complexes with various proteins, including the auxiliary proteins TARPs^{112–114}. TARPs are pre-dominantly expressed in the hippocampus, cortex and striatum¹¹⁵. In cerebellar granule cells, TARP $\gamma 2$ promotes AMPAR surface expression¹¹², while TARP $\gamma 8$ regulates number of AMPARs and LTP in hippocampal neurons⁷⁸. Cryo-EM studies on AMPAR-TARP complexes allowed insights into their structural organization^{116–118}. TARPs consist of an intracellular N-terminus, four transmembrane helices (TM1-4), an extracellular domain (ECD) containing five β -strands ($\beta 1$ -5), an extracellular helix (ECH), four flexible loops ($\beta 1$ - $\beta 2$, $\beta 3$ - $\beta 4$, $\beta 4$ -TM2, TM3- $\beta 5$) and an intracellular C-terminal tail bearing a PDZ domain binding peptide¹¹⁹. The C-tail promotes binding of postsynaptic PSD95 and, hence induces AMPAR trapping¹⁰⁶. TARPs bind tetrameric AMPARs with a stoichiometry of one, two and four TARPs per receptor^{116,118,120} with functional studies suggesting stoichiometries of two and four TARPs per AMPAR^{121,122}. Different loops of the TARPs ECD interact with the LBD domain of AMPAR, depending on the binding site¹¹⁹. These interaction sites are crucial for functional gating of the AMPAR^{123,124}, which could be shown by mutations in the interaction sites of the receptor leading to dysregulation of the channel gating^{114,125,126}. Furthermore, TARPs control signal transmission by slowing of AMPAR desensitization and mutations in the TMD of the AMPAR weaken this effect induced by TARP $\gamma 2$ interaction¹²⁶. Additionally, the C-tail of TARP $\gamma 2$ might also regulate gating modulation, though the underlying mechanism remains elusive¹¹⁹. Despite the impact on AMPAR gating properties, the auxiliary subunits TARPs promote AMPAR-mediated synaptic plasticity. Elimination of $\gamma 8$ in the hippocampus for instance, leads to reduced synaptic transmission and LTP⁷⁸. Molecular replacement studies suggest that interaction between the C-terminus of $\gamma 8$ and PSD95 is essential for LTP^{106,127}, even if earlier studies showed that knock-in mice lacking the PDZ domain peptide of $\gamma 8$ exhibit normal LTP¹²⁸. Dysregulation of TARP $\gamma 2$ caused by a mutation in the TM3 region, is associated with intellectual disability¹²⁹. Antagonists targeting AMPAR-TARP $\gamma 8$ complexes were established as potential therapeutics for treatment of epilepsy in animal models^{130–132}.

KARs. KARs are the third class of ionotropic glutamate receptors in the CNS. They can be found in various parts of the brain such as the granule cells in the cerebellum as well as the mossy fibre synapses in the hippocampus and fulfill different tasks at pre-, post- or extrasynaptic sites¹³³. In presynaptic membranes, KARs modulate excitatory (glutamate) and inhibitory (GABA) neurotransmitter release, whereas postsynaptic KARs promote excitatory neurotransmission and extrasynaptic KARs regulate neuronal excitability^{134–136}. The ionotropic KARs comprise three low affinity subunits GluK1-3 and two high affinity subunits GluK4-5.

The subunits GluK1-3 can form functional homo-tetrameric receptors, whereas GluK4-5 can only assemble as hetero-tetrameric ion channels with the low affinity forms^{137,138}. The GluK2-GluK5 tetramer formation is the prevalent KAR complex in the brain due to the preferential interaction of the NTDs between GluK2 and GluK5 compared to homomeric GluK2-GluK2 assembly²⁵. In mossy fiber CA3 (MF-CA3) pyramidal cells, KARs are localized to the postsynaptic membrane. The C-terminal region of the GluK2 subunit is important for synaptic recruitment of KARs¹³⁹ through interaction with the transsynaptic protein N-cadherin¹⁴⁰. Moreover, the C-terminal PDZ peptide of GluK1, GluK2 or GluK5 interact with the scaffold protein PSD95¹⁴¹. Indeed, PSD95 knockout mice exhibit reduced excitatory postsynaptic currents (EPSC) of KARs in the MF-CA3 synapses even though the underlying mechanism between PSD95 and KAR recruitment remains elusive¹⁴². Presynaptically released proteins from the C1q family determine postsynaptic localization of KARs. These proteins bind to postsynaptic KARs as well as presynaptic neurexin 3 and thus trap KARs in the postsynaptic membrane^{143,144}. Besides the synaptic localization, KARs are associated with excitatory and inhibitory transmission regulating short and long-term plasticity^{134,145}. In terms of excitatory synaptic transmission, presynaptic KARs show a bidirectional character either decreasing¹⁴⁶ or promoting glutamate release¹⁴⁷, depending on the extent of their activation¹³⁶. Postsynaptic KARs induce LTD through phosphorylation of GluK2 by protein kinase C (PKC) and subsequent SUMOylation to enhance or decrease surface expression of KARs¹⁴⁸. The amounts of surface KARs can be modulated by agonist binding^{149,150}. Furthermore, postsynaptic KARs can also mediate AMPAR-LTP in CA3-CA1 synapses¹⁵¹. Interestingly, despite the ionotropic character of the receptor, KARs induce AMPAR-LTP using a metabotropic pathway: activation of G proteins, triggers phospholipase C (PLC) and activates PKC, which results in an increased exocytosis of AMPARs from the intracellular pool¹⁵¹. In contrast, KARs also regulate inhibitory neurotransmission. KARs localized at the presynaptic membrane of hippocampal interneurons reduce GABA release via a metabotropic pathway including PKC and PLC, which leads to lower inhibitory postsynaptic currents (IPSCs)¹⁵². Additionally, postsynaptic KARs again use metabotropic signaling to decrease synaptic GABA-ARs and enhance extrasynaptic GABA-ARs. This leads to reduced synaptic inhibition and promotes extrasynaptic inhibition to ultimately protect neurons from over-excitation^{133,153}. Dysregulation of KARs is associated with neurological pathologies such as temporal lobe epilepsy¹⁵⁴, autism¹⁵⁵, depression¹⁵⁶ and schizophrenia¹⁵⁷. Here antagonists targeting KARs were described as specific therapeutics¹⁵⁸.

2.1.2 Inhibitory synapses

The main modulators in inhibitory synapses in the CNS are Glycine and GABA-A receptors^{1,2}. The following paragraph describes the impact of GABA-A receptors on inhibitory neurotransmission and synaptic plasticity as well as their interaction with transsynaptic scaffolding proteins like Neuroligin 2.

GABA-ARs are ionotropic receptors that mediate inhibitory transmission through hyperpolarization of postsynaptic membranes via their chloride channels¹. GABA-ARs are characterized by a benzodiazepine binding-site which can be addressed by benzodiazepines and other ligands inducing an anxiolytic, sedative and muscle relaxant effect¹⁵⁹. The receptors form pentamers consisting of various combinations of subunits ($\alpha 1$ – $\alpha 6$, $\beta 1$ – $\beta 3$, $\gamma 1$ – $\gamma 3$, δ , ϵ , π , τ , $\rho 1$ – $\rho 3$)³⁵. Based on their localization, GABA-A receptors mediate phasic inhibition in the postsynapse or tonic inhibition in the extrasynaptic regions upon activation by the neurotransmitter GABA. Phasic inhibition shows fast, high-amplitude currents, while tonic inhibition exhibits low-amplitude and persistent currents^{160,161}. In the postsynapse, GABA-ARs predominantly comprise $\alpha 1$, $\alpha 2$, $\alpha 3$ and $\gamma 2$ subunits, whereas extrasynaptic receptors are built of $\alpha 4$, $\alpha 5$, $\alpha 6$ along with the δ subunit¹⁵⁹. Although not yet completely understood, interactions between GABA-ARs with scaffolding proteins such as gephyrin are essential for receptor localization in the postsynapse^{162,163}. For instance, the subunits $\alpha 1$ – $\alpha 3$ and $\beta 2$ – $\beta 3$ can attach to gephyrin via their intracellular loop to trap the receptor in the postsynaptic membrane^{164–167}. Gephyrin molecules are organized in trimers¹⁶⁸ which might form a cluster network through auto-aggregation¹⁵⁹ and interact with GABA-ARs, effector proteins such as neuroligin 2 and collybistin, as well as cytoskeletal elements¹⁶⁹ (Figure 3). Collybistin activates the Rho GTPases CDC-42 and TC-10 and thus induces gephyrin clustering in the inhibitory PSD¹⁷⁰. Knockout of collybistin in mice lead to abolishment of GABA-AR and gephyrin clusters, emphasizing its importance for postsynaptic organization^{171,172}. The current understanding of GABA-AR organization in the postsynaptic membrane is the following: Postsynaptic NL2/3 build transsynaptic nanocolumns via interaction with presynaptic α/β -Neurexins. GABA-ARs integrate into the membrane at extrasynaptic sites and then diffuse laterally to the postsynaptic compartment¹⁷³. Here, collybistin interacts with Rho GTPases and gephyrin to ensure trapping of GABA-AR¹⁵⁹. Additional post-translational phosphorylation of various GABA-AR subunits affects channel gating, kinetic properties and trafficking of the receptors^{43,174,175}. Organization of extrasynaptic GABA-ARs is controlled via metabotropic signaling by GABA-BRs^{176,177}. Tonic inhibition in the dentate gyrus and thalamus is regulated by protein kinase A and PKC¹⁷⁸. For instance, PKC-induced phosphorylation of the $\alpha 4$ -GABA-AR subunit promotes surface

expression of the receptors¹⁷⁹. GABA-AR mediated transmission is of central importance in neuronal development, including stem cell proliferation and dendritic growth^{180,181}. Therefore, dysregulation of GABA-ARs is associated with a broad range of neurological disorders such as epilepsy¹⁸², schizophrenia¹⁸³, autism¹⁸⁴ and depression¹⁸⁵. In epilepsy, GABA-AR mutations influence receptor trafficking, surface expression and diffusion¹⁸⁶.

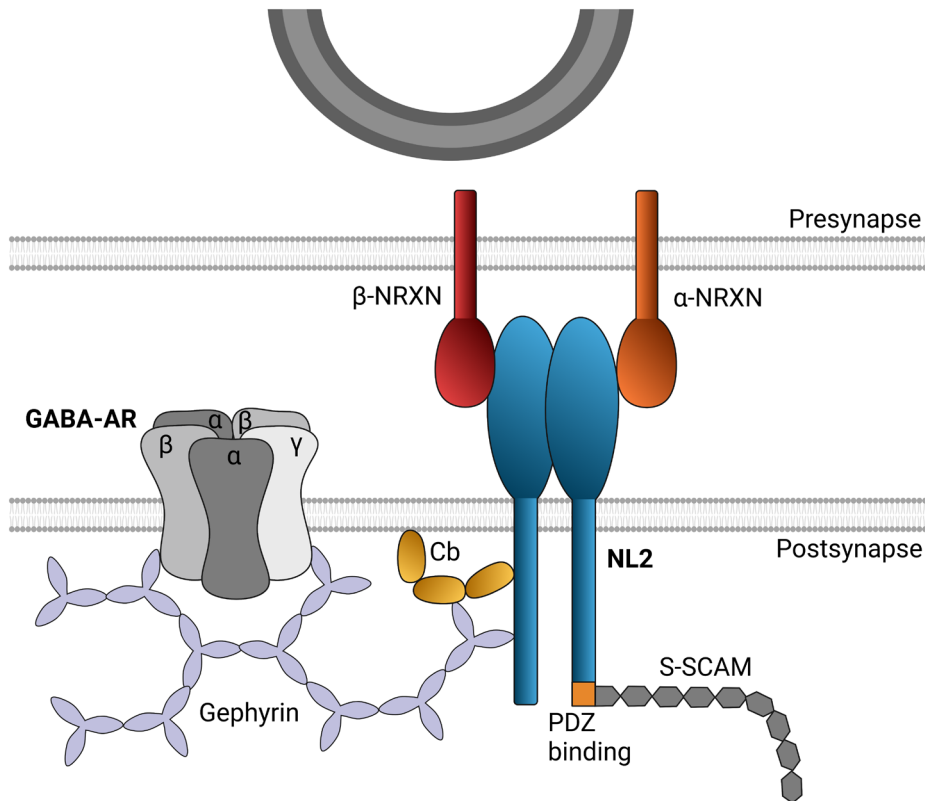


Figure 3 - Synaptic organization at inhibitory synapses. Transsynaptic interaction of postsynaptic NL2 and presynaptic neuexins (α and β) promote linkage between pre- and postsynaptic compartments at inhibitory synapses. In this process, NL2 forms dimers through their extracellular domain. At the postsynapse, C-terminal NL2 interacts with collybistin (Cb) and gephyrin to ensure trapping of pentameric GABA-ARs in the membrane. In addition, the PDZ binding site of NL2 allows interaction with further scaffolding proteins, such as S-SCAM. Created with BioRender.com.

Neuroligins are postsynaptic adhesion proteins that determine synaptic formation and function in inhibitory and excitatory synapses via interaction with presynaptic neuexins. The human neuroligin family comprises five proteins (NL1-3, 4X, 4Y)¹⁸⁷⁻¹⁸⁹. NL1 was identified as a main regulator in excitatory synapses^{190,191}, whereas NL2 functions only at GABAergic inhibitory synapses¹⁹². NL2 is a type I transmembrane protein consisting of an extracellular domain (ECD) for interaction with neuexins and dimerization of NL2, an α -helical transmembrane domain (TMD) and a C-terminal domain promoting GABA-AR recruitment and signaling^{193,194}. NL2 forms dimers in the postsynapse to ensure clustering of neuexin monomers in the presynapse¹⁹⁴

(Figure 3). At the opposing site, the C-terminus of NL2 builds a tripartite complex by interacting with the guanosine-diphosphate/guanosine-triphosphate exchange factor collybistin and the scaffold protein gephyrin, which is necessary for the recruitment of GABA-ARs^{194–196}. Additionally, NL2 contains an intracellular PDZ binding peptide for attachment to the synaptic scaffolding molecule (S-SCAM)¹⁹⁷. Overexpression of NL2 in neurons and transgenic mice promotes inhibitory transmission and implicates the importance of NL2 for synaptic inhibition^{198,199}. Moreover, knockout of NL2 in mice leads to a reduction of postsynaptic GABA-A receptors and gephyrin throughout all brain regions, thus changing the postsynaptic organization, but without influencing the total amount of inhibitory synapses¹⁹⁴. Due to the distinct link between NL2 and inhibitory transmission and plasticity, dysregulation of NL2 results in severe pathologies, including schizophrenia²⁰⁰, anxiety, autism²⁰¹ and depression²⁰². For instance, patients experiencing a major depression exhibited a reduced expression of NL2 in the nucleus accumbens²⁰². Similarly, the amount of NL2 expression dropped in iPSC-derived cortical interneurons of patients with schizophrenia^{194,203}. Additionally, a de novo nonsense mutation in *NL2* led to autism spectrum disorder and anxiety in a male patient^{194,201}.

2.2 Labeling methods

Labeling of a protein of interest with a fluorescent marker is necessary to enable visualization of the protein using fluorescence microscopy. As mentioned in the introduction (1.3), there are numerous ways to attach fluorescence tags to nearly any target structure. The following chapter will focus on the theory behind the use of fluorescent proteins, organic dyes, and immunostaining as well as the principle of genetic code expansion and the subsequent application of bioorthogonal click chemistry.

2.2.1 Fluorescent proteins

The renowned green fluorescent protein (GFP) was isolated from the jellyfish *Aequorea victoria* in 1962²⁰⁴. GFP possesses a β -barrel structure with three amino acids (Ser-Tyr-Gly) forming the chromophore by undergoing cyclization, dehydration and oxidation²⁰⁵. Ever since GFP was discovered, it found various applications in biological and medical approaches, for instance as fusion tag to investigate protein dynamics in living cells²⁰⁶, or as a reporter gene to study gene expression under a promoter of interest²⁰⁷. The field of potential uses has expanded even further, when diverse mutations in the original gene sequence led to the generation of yellow (YFP), cyan (CFP) and blue (BFP) shifted variants of GFP^{208,209}. For instance, the overlapping spectra of e.g. GFP and BFP or CFP and YFP make these fluorescent proteins suitable pairs in FRET

experiments which are performed to determine protein-protein interactions²⁰⁸. pHluorin, another GFP derivate, is a pH sensitive fluorescent protein which exhibits a decrease of fluorescence in acidic solutions. This special feature allows the analysis of proteins navigating between intra- and extracellular compartments²¹⁰. Further modifications of GFP resulted in photoactivatable GFP (PA-GFP)²¹¹ which set the basis for single molecule localization microscopy (SMLM), such as photoactivated localization microscopy (PALM), using fluorescent proteins²¹². Additional investigations along this line enabled a whole palette of mainly photoactivatable (PA-GFP, PA-mCherry), photoswitchable (PS-mOrange, Dendra, mEos) or photochromic (Dronpa) fluorescent proteins with distinct applications in SMLM⁶².

2.2.2 Organic dyes

Organic dyes are small molecules with an extended delocalized π -electron system²¹³. A variety of different classes of fluorescent dyes were synthesized and the dye classes of xanthenes, rhodamines, indoles/imidizoles, coumarins and cyanines find wide biological application based on their chemical (lipophilicity, stability) and photophysical properties (absorption and emission, lifetime and brightness)²¹⁴. One of the first classes of organic dyes are the xanthenes, to this day especially fluorescein²¹⁵ is still very popular in biological and medical research²¹⁴. Fluorescein is highly tunable and hence can be applied as a sensor for pH²¹⁶ and ions such as calcium²¹⁷ and sodium²¹⁸. The dye class of rhodamines, which are isologues of fluorescein, are also used as indicators for ion concentrations²¹⁷ or reactive oxygen species²¹⁹. Further modifications led to silicon-containing rhodamines, such as hydroxy-methyl silicon-rhodamine (HMSiR). These dyes show spontaneous blinking behavior and therefore find application in super-resolution microscopy without the need for switching buffers or high laser powers²²⁰. Another group of dyes, the indoles and imidizoles, are applicable for DNA-labeling, which is achieved by intercalation of the molecules into the minor groove of DNA²²¹. The most prominent derivatives are 4',6-diamidino-2-phenylindole (DAPI) and dibenzimidizoles from the Hoechst AG, which find utilization in fluorescence microscopy, flow cytometry²²² and live cell approaches²²³. The class of coumarins enables monitoring of proteinase activity²²⁴ or the assembly of enzyme substrates such as hydrolases²²⁵. Finally, cyanine derivatives such as the sulfoindocyanines Cy3 and Cy5 are used in FRET experiments²²⁶ and furthermore they are well suited for super-resolution fluorescence microscopy methods like *d*STORM due to their photophysical properties^{227,228}.

2.2.3 Immunostaining

Antibodies are a versatile tool, not only for therapeutic application²²⁹, but also for labeling of proteins and other target structures for fluorescence microscopy via immunohistochemistry²³⁰. Human antibodies are immunoglobulins, which consist of two identical light (LC) and heavy chains (HC), assembled in a heterodimeric Y-shape (Figure 4). In and between the two heterodimers, disulfide bonds connect the HC and the LC as well as the LCs to each other. The LCs consist of a constant domain (CL) and a variable domain (VL) and HCs of the IgG isotype possess three constant (CH) and one variable domain (VH). The functional antibody comprises two fragment antigen binding (Fab) domains that are necessary for recognizing a specific antigen and one fragment crystallizable (Fc) domain, which binds receptor molecules²³¹.

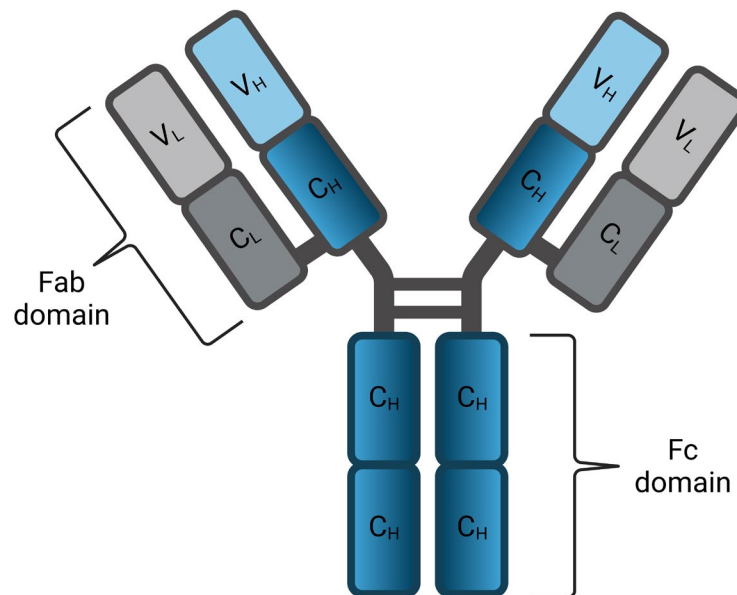


Figure 4 - Schematic heterodimeric illustration of an IgG antibody. Variable (V) and constant (C) domains of two light chains (grey) and two heavy chains (blue) form the IgG antibody. Each chain of the antibody comprises a single variable domain (V_H , V_L). The light chains possess each one constant domain (C_L), while the heavy chains carry each three constant domains (C_H). The fragment antigen binding domain (Fab) consists of two variable (V_L , V_H) and two constant domains (C_L , C_H), whereas the fragment crystallizable (Fc) domain bears four constant domains (C_H). The Fab domain ensures antigen binding and the Fc domain recognizes receptor molecules. Created with BioRender.com.

To easily crosslink any organic dye with an antibody, the primary amino group (NH_2) of the lysine amino acids in the antibody can be reacted with a N-hydroxysuccinimide (NHS) ester attached to the respective dye²³². General immunohistochemistry uses a primary antibody binding the epitope of the target structure and secondary antibodies coupled to fluorophores directed against the primary antibody^{230,233}. To avoid crosslinking and size issues caused by

full-length antibodies, strategies using only fragments of the antibody arose, such as the Fab and scFv fragments or even just a single antibody domain termed nanobody^{54,55}.

2.2.4 Genetic code expansion and bioorthogonal click chemistry

Genetic code expansion. The universal genetic code implies that genetic information in form of deoxyribonucleic acid (DNA) is first transcribed into messenger ribonucleic acid (mRNA) prior to translation into amino acids. There are four different nitrogenous bases resulting in four DNA nucleotides: adenine (A), thymine (T), guanine (G) and cytosine (C). In mRNA, the DNA nucleotide thymine (T) is substituted with the nucleotide uracil (U). During translation, every base triplet (codon) of the mRNA is translated into one of the 20 canonical amino acids present in most living organisms. To achieve this, endogenous transfer-RNAs (tRNAs) are loaded with canonical amino acids via respective aminoacyl-tRNA synthetases. Then, tRNAs bearing amino acids attach to the mRNA/ribosome complex and the ribosome incorporates amino acids in the growing polypeptide chain (Figure 5, blue)²³⁴. The translation terminates at natural occurring opal (UGA), ochre (UAA) and amber (UAG) codons induced by release factors (RF)²³⁵. However, some organism such as the archaea *Methanosarcina mazei* decode the UAG codon with the amino acid Pyrrolysine through an additional 21st tRNA^{Pyl}/tRNA synthetase^{PylRS} pair²³⁶. Mutation studies on the tRNA synthetase^{PylRS} (in the following termed PylRS) allowed successful introduction of unnatural aromatic amino acids at amber stop codon sites and therefore enable expansion of the genetic code (GCE) in eukaryotes with a variety of new amino acids. In this process, the amber stop codon gets suppressed in order to incorporate the unnatural amino acids at a specific protein site^{237–240} (Figure 5, red). The optimized tRNA^{Pyl}/PylRS pair is orthogonal to endogenous tRNA/tRNA synthetase pairs in bacteria²³⁶, eukaryotic cells²⁴¹ and animals²⁴². Hence, its introduction does not result in cross-reactions or interference with the endogenous translational machinery. The amber suppressor-tRNA competes with the termination of the translation through the endogenous RF1²³⁵. Due to this, high amounts of tRNA/tRNA synthetase are required to obtain efficient incorporation of unnatural amino acids into proteins²⁴³. Several aliphatic and aromatic amino acids were established for GCE⁷³ and subsequently used for bioorthogonal labeling of proteins in mammalian cells⁷⁴. Furthermore, the GCE system was introduced via adeno-associated viruses into the brain of a living mouse, showing expression of a GFP version with incorporated amino acids⁷⁶. In the future, the powerful tool of GCE has the potential to find wider-ranging application in living animals and by optimizing protocols it will likely become possible to target more complex proteins as well.

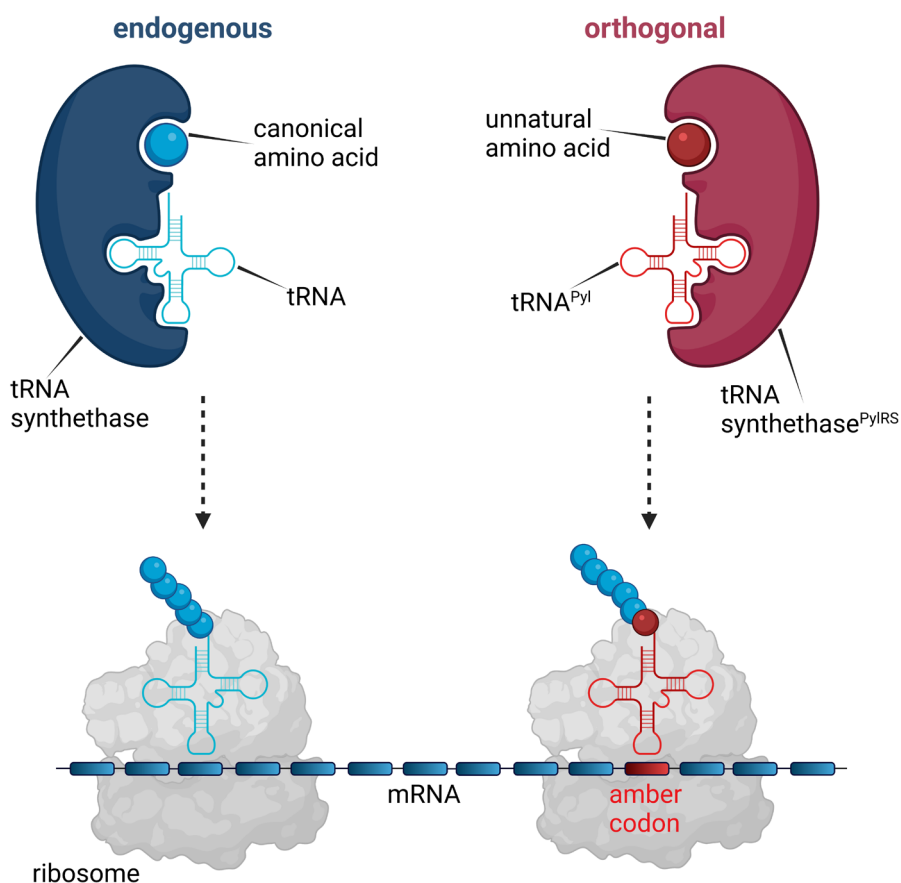


Figure 5 – Principle of genetic code expansion. The endogenous tRNA synthetases (blue) transfer canonical amino acids to endogenous tRNAs. tRNAs carrying amino acids bind to the mRNA/ribosome complex during translation to ensure incorporation of canonical amino acids into the growing polypeptide chain. Introduction of the orthogonal tRNA^{Pyl}/PylRS synthetase pair (red) into the host machinery allows integration of unnatural amino acids at amber codon (UAG) sites. Additionally, the amber stop codon (UAG) can induce termination of translation via the release factor 1 (RF1). Created with BioRender.com.

Bioorthogonal click chemistry. Biomolecules that specifically only react with each other and hence are orthogonal to molecules in biological samples find broad application *in vitro* and *in vivo*^{73,244}. The functional azide group for instance, reacts with phosphines in Staudinger ligations²⁴⁵ which could be used to visualize modified glycans in living cells and animals^{246,247}. However, Staudinger reactions are slow and the phosphine molecules are sensitive to oxidation²⁴⁸. Besides phosphines, azides additionally interact with alkynes via Cu^I-catalyzed alkyne-azide cycloaddition (CuAAC) in a faster manner compared to Staudinger ligation^{249,250} (Figure 6). Since the use of copper as a catalyst can be toxic to living cells²⁵¹, copper-free reactions between azides and strained-alkynes via strain-promoted alkyne-azide cycloaddition (SPAAC) gained popularity^{250,252} (Figure 6). In particular, cyclooctyne-based compounds were established to label living mammalian cells²⁵³ and animals²⁵⁴ in a copper-free environment.

Additionally, the methods CuAAC and SPAAC could be applied in super-resolution fluorescence microscopy to image azide-modified glycoproteins in the plasma membrane labeled with Alexa Fluor 647 coupled alkynes^{255,256}. Moreover, tetrazines react chemoselective with alkynes (not shown) or alkenes, such as trans-cyclooctenes (TCO) via strain-promoted inverse-electron demand Diels-Alder cycloaddition (SPIEDAC)²⁵⁷. All mentioned reactions allow attachment of a fluorophore (Figure 6, blue) to a target of interest (Figure 6, red).

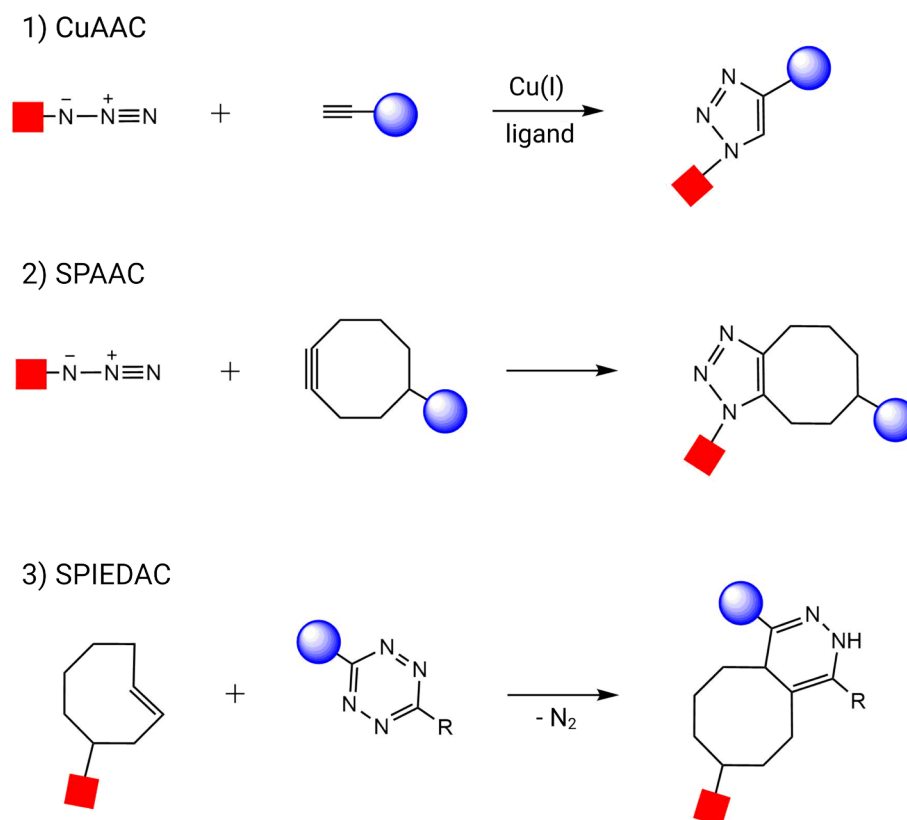


Figure 6 - Bioorthogonal labeling reactions for specific attachment of fluorophores. Bioorthogonal labeling enables attachment of a fluorophore (blue) to a target structure (red). Azides react with alkynes either strain-promoted (SPAAC) or copper catalyzed (CuAAC) via cycloaddition. Tetrazines form complexes with strained alkenes or alkynes through strain-promoted inverse-electron demand Diels-Alder cycloaddition (SPIEDAC). Created with BioRender.com.

SPIEDAC reactions are rapid compared to azide-alkyne conjugation²⁵⁸ and the quenching mechanism of fluorophores by tetrazine leads to an increased fluorescence (turn-on) upon binding to the alkene^{259,260}. This fluorogenic effect can be advanced for intracellular site-specific labeling of proteins tagged with unnatural amino acids²⁶¹. Demonstrating the broad range of application of bioorthogonal labeling once again, compounds consisting of two linked tetrazines (bistetrazines) are also used in crosslinking of TCO-carrying proteins²⁶². Furthermore, amino acids bearing TCOs were successfully used for GCE in living cells and

subsequent labeling with tetrazine dyes²⁶³. Detailed protocols on labeling insulin receptors in mammalian cells using bioorthogonal click chemistry, allow easy application of this method to nearly any protein of interest⁷⁴. NMDA glutamate receptors for instance, can be tagged with unnatural amino acids and subsequently labeled with tetrazine dyes. This process allows super-resolution imaging of surface exposed NMDA receptors in HEK293T cells with electrophysiological studies proving functionality of clicked receptors⁷⁵.

2.3 Fluorescence and Microscopy

2.3.1 Excitation and Emission

Nowadays, a plethora of fluorescent dyes is commercially available for fluorescence microscopy (see 2.2.2). To emit fluorescence, a fluorescent molecule needs to absorb light of a defined wavelength leading to excitation of an electron from the ground state (singlet state S_0) to a higher energy level S_1 , S_2 or S_n . All singlet states possess multiple sub-states with different energy levels. In this excited state, the electron relaxes to the lowest S_1 state through internal conversion (IC). From this location, the electron can return to the singlet state S_0 by emitting a photon (fluorescence) or converting the energy into heat²⁶⁴. The emission process takes place in the temporal range of nanoseconds²⁶⁵. In 1852, George Stokes observed that illumination of the mineral fluor spar with ultraviolet light led to the emission of red-shifted light²⁶⁶. This change of wavelength between the absorption- and emission-spectrum was later termed Stokes shift and is essential for fluorescence microscopy, due to the possibility to separate excitation and emission light from each other. Several fluorescence microscopes have been developed which exploit the general principle of fluorescence. All of them use light sources to excite the respective fluorophores, optical lenses to focus the light on the specimen and collect the fluorescence signal and finally detectors to convert the light information into digital information that can be processed further. In the following, three fluorescence microscopy setups named CLSM, *d*STORM and SIM will be introduced.

2.3.2 Confocal laser scanning microscopy (CLSM)

A confocal microscope is a light microscope that uses solely the fluorescence of the specimen that originates from the focal plane and ignores light besides this plane. In this process, just a subset of the probe is illuminated at a time, which makes it necessary to shift the focal plane and scan pixels sequentially to ensure imaging of the whole probe. The setup is equipped with lasers of different wavelengths to excite the respective fluorophores. A dichromatic mirror and

an objective with a high numeric aperture direct the excitation light to the probe. A pinhole filters the emission light of the specimen to reject out of focus-light and thereby increases image contrast. Finally, a photomultiplier tube detects only the emission light that arises in the focal plane, multiplies the signal and converts the light information into a digital signal²⁶⁷. By 1987, CLSM setups could already image living kidney epithelium cells²⁶⁸. The CLSM allows imaging of cells labeled with multiple dyes and is capable of investigating protein diffusion via fluorescence recovery after photobleaching (FRAP) or protein-protein interactions by fluorescence resonance energy transfer (FRET). However, CLSM microscopes rather enhance the contrast of the image than the actual resolution (~ 250 nm lateral resolution)²⁶⁹. Nevertheless, due to the increased contrast, CLSM setups can be utilized to evaluate protein expression levels on transient transfected cells offering additional 3D information. After this first evaluation, suitable specimen can be analyzed further on a single molecule level using super-resolution microscopy techniques.

2.3.3 Super-resolution fluorescence microscopy

Single molecule localization microscopy *d*STORM. The optical resolution of two point emitters is limited due to diffraction of light to half of the wavelength of the excitation light²⁷⁰. Several super-resolution fluorescence microscopy techniques, including PALM²¹², STED²⁷¹, STORM²⁷² and *d*STORM²²⁷ were established to surpass the diffraction limit of ~ 200 nm and achieve molecular localization. Since the localization of two emitters is restricted when they emit fluorescence simultaneously, widefield-methods such as *d*STORM rely on the sequential recording of isolated emitters over time to ensure precise localization of each fluorophore²⁷³. To achieve this, *d*STORM exploits the ability of fluorophores to enter the triplet state F_T stochastically out of the excited state F_{S1} by intersystem crossing (Figure 7). At this state, reducing agents such as thiol-containing buffers enable reduction of the fluorophore to a non-fluorescent radical form F^* (off-state). The radical fluorophore can be oxidized to return to the ground state F_{S0} , where it is fluorescent through cycling between F_{S0} and F_{S1} (on-state). Reduced fluorophores are stable and stay in the off-state for 0.5-10 s, whereas the on-state offers a lifetime of 10-50 ms. Hence, the majority of fluorophores can be switched off and only a subset of isolated emitters are detected in every frame^{228,274}. Finally, the location of every fluorophore can be determined by fitting the point-spread-function of the emitter with a two-dimensional Gaussian fit prior to reconstructing a final image containing all detected localizations²⁷⁵. Since the localization precision is dependent on the amount of collected photons, bright fluorophores with high photon yield and good switching behavior need to be

selected for *d*STORM experiments²⁷⁶. Furthermore, the Nyquist-Shannon theorem states that a sample needs to be labeled twice as dense as the desired resolution. For instance, to achieve a 20 nm resolution, the sample structure must contain a fluorophore at least every 10 nm²²⁸. Exploiting the *d*STORM technique, cellular structures such as the nuclear pore complex could be resolved on the nanoscale, revealing the eightfold symmetry of these complexes²³⁰. Advancing this method, *d*STORM was utilized for multicolor imaging²⁷⁷ and 3D microscopy²⁷⁸. Another option is the combination of *d*STORM with electron microscopy in correlative approaches²⁷⁹.

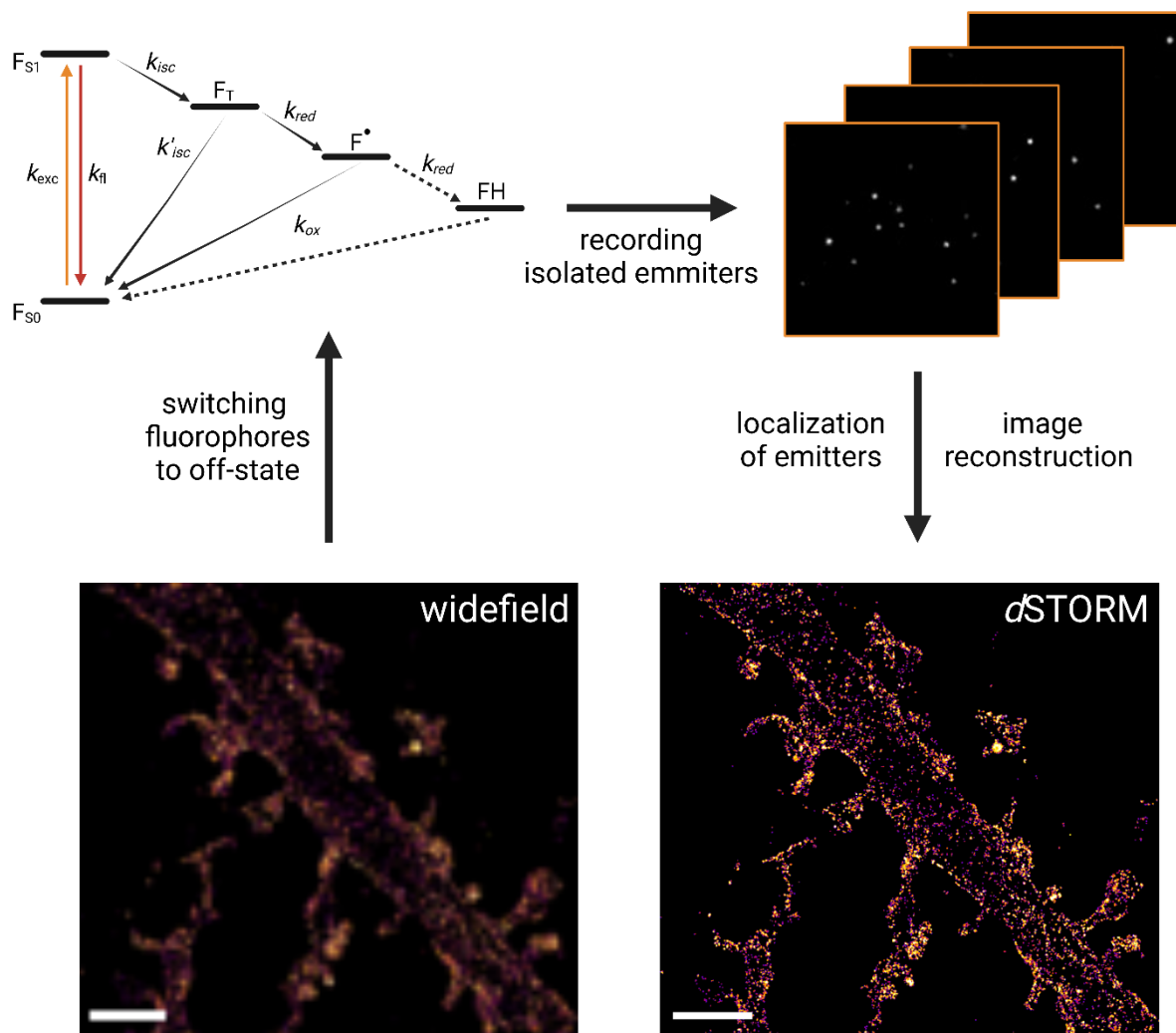


Figure 7 - Principle of *d*STORM. At a widefield microscope, the resolution of the fluorescence image is limited by the diffraction of light. Fluorophores can be excited from the ground state (F_{S0}) to an excited state (F_{S1}) by illumination with laser light (k_{exc}). Excited fluorophores can either relax to the ground state emitting fluorescence with rate (k_{fl}), or enter a triplet state (F_T) with rate (k_{isc}). The fluorophore can return to the ground state with rate (k'_{isc}) or can be switched off by incubation in thiol-buffers reducing the fluorophore to a non-fluorescent radical anion (F^*) (k_{red}). The fluorophore radical can be further reduced to a non-fluorescent state (FH). Oxidation of the non-fluorescent states (k_{ox}) leads to recovering of the fluorophore to the ground state (F_{S0}). This principle enables the separation of emitters in each frame to allow precise fitting of the point-spread-function via a two-dimensional Gaussian fit. After recording of several thousands of frames, the localizations of all emitters are determined and a super-

resolved image can be reconstructed with a lateral resolution of ~ 20 nm. Scalebar 2 μ m. Created with BioRender.com.

Structured illumination microscopy (SIM). SIM utilizes a conventional widefield setup in combination with structured illumination to achieve a resolution of ~ 120 nm. To obtain structured illumination, a grating is placed in the excitation path to induce multiple light patterns. These light patterns interfere with the emission pattern of the target structure (interference patterns) and form moiré fringes. This information can be used to decode otherwise unresolvable information in the following data analysis. Rotation of the grating in different directions leads to a higher number of moiré fringes, equaling more information about the target structure and ultimately higher resolution²⁸⁰. Standard SIM setups use an objective with a high numeric aperture and a CCD camera for signal detection. Images are recorded with multiple grating orientations and several images per orientation. The recordings are finally reconstructed and resampled to one image²⁸¹. The advantages of SIM compared to SMLM techniques are the considerably fast imaging, which can be beneficial for live imaging^{281,282}, the easy multicolor feasibility and resolving 3D axial information of target structures²⁸³. SIM microscopes find application in diverse research fields and can be utilized to study endocytotic processes²⁸⁴, cellular components such as mitochondria²⁸¹, the endoplasmic reticulum²⁸⁵ and nuclear periphery²⁸⁶.

2.3.4 Expansion microscopy

Super-resolution methods such as *d*STORM, STED and PALM enhance the resolution by isolating single emitters from each other, either through a technical approach (STED) or via utilizing photo-physical behavior of fluorophores (*d*STORM, PALM). An alternative approach was established promoting the resolution through physical expansion of the specimen of interest using a hydrogel²⁸⁷. In this procedure, the immunolabeled target structure needs to be tagged with a crosslinker to ensure transfer of this information into the poly-acrylamide gel. Conventional glutaraldehyde²⁸⁸ or AcX²⁸⁹ were established as functional linkers to anchor proteins within the hydrogel. The polymer-gel consists of monomeric acrylamides and acrylates²⁸⁷. To obtain isotropic expansion of the swellable polymer-gel, proteins are digested using proteinase K²⁸⁸ or heat denaturation²⁹⁰ prior to expanding the hydrogel in ddH₂O. Initial protocols achieved lateral resolution of ~ 65 nm through 4.5-fold expansion of the specimen²⁸⁷. The polymerization and digestion steps affect the fluorescent intensity of some dyes and fluorescent proteins dramatically. So it is important to consider the choice of fluorophores used

in ExM or to fluorescent label the probe post gelation²⁸⁹. Additionally, the expansion of the specimen dilutes the fluorescence signal and hence favors amplification protocols using fluorescent labels with multiple fluorophores such as antibodies^{291,292} or biotin-streptavidin complexes^{293,294}. Over the last years, a variety of new optimized expansion protocols arose, such as protein-retention ExM²⁸⁸, Magnified Analysis of Proteome (MAP)²⁹⁰ and Ultrastructure Expansion Microscopy (U-ExM)²⁹². U-ExM for instance, allows to maintain the ultrastructure of centrioles²⁹² and the synaptomenal complex²⁹¹ after expansion. Re-embedding of the hydrogel with an uncharged acrylamide gel enabled combination of ExM with super-resolution fluorescence microscopy *d*STORM²⁹⁵. Furthermore, iterative gelation approaches pushed the expansion factor up to ~20-fold with ~25 nm molecular resolution using confocal microscopes²⁹⁶. Additionally, optimization of gel solutions enabled an applicable protocol for ~10-fold expansion microscopy and achieved also ~25 nm resolution without re-embedding^{297,298}. Finally, expansion microscopy can be applied to reveal ultrastructure in *Caenorhabditis elegans*²⁹⁹ or even the whole brain of *Drosophila melanogaster*³⁰⁰.

3 Materials and Methods

The following tables contain all materials and methods used for experiments. If not stated otherwise all solutions were prepared in double-distilled water (ddH₂O) purified by a Barnstead™ GenPure™ Pro Water Purification System with >18 MOhm.

3.1 Chemicals, buffers and consumables

Table 1 - Chemicals used for molecular biology and cell biology experiments

| Chemical | Company (catalog number) |
|-----------------------------|---------------------------------------|
| 5x Q5 Puffer | New England Biolabs (M0491S) |
| Q5 DNA Polymerase | New England Biolabs (M0491S) |
| dNTPs | Sigma Aldrich (DNTP100-1KT) |
| 6x Gel Loading Dye | New England Biolabs (B7025S) |
| Quick-Load 2-log DNA Ladder | New England Biolabs (N0468S) |
| Agarose | Sigma-Aldrich (A9539) |
| Safeview | Applied Biological Materials (G108) |
| TRIS | Sigma-Aldrich (T1503) |
| Boric acid | Merck (10043-35-3) |
| EDTA | Sigma-Aldrich (60-00-4 and ED2P) |
| Glucose | Sigma-Aldrich (49163) |
| Tryptone | Melford Biolaboratories Ltd. (T60065) |
| Yeast extract | Melford Biolaboratories Ltd. (Y20025) |
| Sodium chloride | Sigma-Aldrich (S9888 and S5886) |
| Bacteriological Agar | Sigma-Aldrich (A5306) |
| Ampicillin | Melford Biolaboratories Ltd. (A40040) |
| Kanamycin | Melford Biolaboratories Ltd. (K22000) |
| Poly-D-Lysine | Sigma-Aldrich (#P6407) |
| DMEM | Sigma-Aldrich (D5796 and D8062) |
| FCS | Sigma-Aldrich (F7524) |
| Penicillin/Streptomycin | Sigma-Aldrich (P4333) |
| HBSS | Sigma-Aldrich (55037C) |
| PBS | Sigma-Aldrich (P549) |
| Formaldehyde | Sigma-Aldrich (50-00-0) |
| Glutaraldehyde | Sigma-Aldrich (354400) |
| β-Mercaptoethylamin (MEA) | Sigma-Aldrich (M6250) |

| | |
|---|----------------------------------|
| Diisopropylethylamine (DIPEA) | Sigma-Aldrich (D125806) |
| Acrylamide/Bis-acrylamide | Sigma-Aldrich (A9926) |
| Sodium acrylate | Sigma-Aldrich (4082220) |
| Ammonium persulfate (APS) | Sigma-Aldrich (A3678) |
| Tetramethylethylenediamine (TEMED) | Sigma-Aldrich (T7024) |
| N,N-Dimethylacrylamide (DMAA) | Sigma-Aldrich (274135) |
| Potassium persulfate (KPS) | Sigma-Aldrich (3798245) |
| Acryloyl-X, Succinimidyl Ester (AcX) | ThermoFisher (A20770) |
| Triton X-100 | ThermoFisher (AM2548) |
| Guanidine HCl | Sigma-Aldrich (50933) |
| Proteinase K | ThermoFisher (AM2548) |
| Sodium hydrogen carbonate (NaHCO ₃) | Fisher Scientific UK (S/4240/60) |
| HEPES solution | Sigma-Aldrich (H0887) |
| Trans-Cyclooct-2-en – L – Lysine (TCO*A) | SiChem (SC-8008) |
| Triton-X | Sigma-Aldrich (T0307) |

Table 2 - Buffers and Solutions

| Buffer/Solution | Contents |
|------------------------------------|---|
| Transformation buffer (pH 6.7) | <ul style="list-style-type: none"> ▪ 10 mM PIPES ▪ 15 mM CaCl₂ ▪ 250 mM KCl ▪ 7.5 % Glucose |
| Switching buffer | 100 mM MEA in PBS |
| Gel electrophoresis buffer | stock solution: 5x TBE (0.5l) <ul style="list-style-type: none"> ▪ 27 g TRIS, ▪ 13.8 g boric acid ▪ 10 ml EDTA (0.5M, pH 8.0) |
| Bacteria culture media | stock solution: 10x TY media (1l, pH 7.4) <ul style="list-style-type: none"> ▪ 80 g tryptone, ▪ 50 g yeast extract, ▪ 25 g NaCl autoclaved (121°C, 15 min) |
| Agar plates for bacteria selection | 2x TY plates 1l <ul style="list-style-type: none"> ▪ 5 g tryptone ▪ 2.5 g yeast extract ▪ 4 g NaCl ▪ 7.5 g agar autoclaved (121°C, 15 min) |

| | |
|---|--|
| Fixation solution | 4% Formaldehyde + 0.25% Glutaraldehyde in PBS |
| Monomer gel solution (4x expansion) ²⁸⁹ | <ul style="list-style-type: none"> ▪ 8.625% sodium acrylate ▪ 2.5% acrylamide ▪ 0.15% N,N'-methylenebisacrylamide ▪ 2 M NaCl ▪ 1x PBS ▪ 0.2% APS ▪ 0.2% TEMED |
| Monomer gel solution (10x expansion) ²⁹⁸ | <ul style="list-style-type: none"> ▪ 0.267 g DMAA ▪ 0.064 g sodium acrylate ▪ 0.57 g ddH₂O ▪ 100 µl KPS (0.036 g/l) ▪ 4 µl TEMED |
| Digestion buffer ²⁹⁸ | <ul style="list-style-type: none"> ▪ 50 mM Tris pH 8.0 ▪ 0.5% Triton X-100 ▪ 0.8 M guanidine HCl ▪ 8 U/ml proteinase K |

3.2 Labeling reagents

Table 3 - Tetrazine derivatives

| Type | Specificity | Conjugate | Company |
|-------------------|-------------|-------------|--|
| H-Tet-Cy5 | TCO*-K | Cy5 | Jena Bioscience (CLK-015-05) |
| H-Tet-Cy3 | TCO*-K | Cy3 | Jena Bioscience (CLK-014-05) |
| Pyr-Tet-ATTO643 | TCO*-K | ATTO643 | Jena Bioscience (CLK-101) |
| H-Tet-Digoxigenin | TCO*-K | Digoxigenin | H-Tet-Amine: Jena Bioscience (CLK-001-5) Digoxigenin-NHS: Sigma-Aldrich (55865) |

Table 4 – Antibodies

| Type | Host | Specificity | Conjugate | Source |
|-------------------------|--------|-------------------------|-------------------------|--|
| Primary (polyclonal) | Rabbit | anti-GluK2 | | Thermo Fisher (#PA5-32427) |
| Primary (polyclonal) | Rabbit | anti-GABA-AR $\alpha 2$ | | Synaptic Systems (224 103) |
| Primary (monoclonal) | Mouse | anti-vGAT | | Synaptic Systems (131 011) |
| Primary (monoclonal) | Rabbit | anti- $\gamma 2$ Ex2 | AF647 | Daniel Choquet (CNRS, Bordeaux) |
| Primary (monoclonal) | Rabbit | anti- $\gamma 8$ Ex1 | AF647 | Daniel Choquet (CNRS, Bordeaux) |
| Primary (monoclonal) | Mouse | anti-GluA | | Synaptic System (182 411) |
| Primary (monoclonal) | Mouse | anti-HA | CF568 | Antibody: Thermo Fisher (26183) CF568-NHS: Sigma-Aldrich (SCJ4600027) |
| Primary (monoclonal) | Mouse | anti-HA | AF488 AF555 AF647 | Thermo Fisher (26183-A488) (26183-A555) (26183-A647) |
| Primary (monoclonal) | Rabbit | anti-Digoxigenin | | Antibody: Sigma-Aldrich (700772) |
| Primary (monoclonal) | Rabbit | anti-Digoxigenin | CF568 | Antibody: Sigma-Aldrich (700772) CF568-NHS: Sigma-Aldrich (SCJ4600027) |
| Primary (monoclonal) | Rabbit | anti-Digoxigenin | AF647 | Antibody: Sigma-Aldrich (700772) AF647-NHS: Thermo Fisher (A-20006) |

| | | | | |
|---------------------------|------|-----------------|-------|-------------------------|
| Secondary (polyclonal) | Goat | anti-mouse IgG | AF647 | Thermo Fisher (A-21235) |
| Secondary (polyclonal) | Goat | anti-rabbit IgG | AF647 | Thermo Fisher (A-21245) |
| Secondary (polyclonal) | Goat | anti-mouse IgG | AF568 | Thermo Fisher (A-21124) |

3.3 Enzymes

Table 5 – Enzymes

| Enzyme | Company (catalog number) |
|-------------------|---------------------------------|
| EcoRI-HF | New England Biolabs (R3101S) |
| AgeI-HF | New England Biolabs (R3552S) |
| DpnI | New England Biolabs (R0176S) |
| BamHI | New England Biolabs (R3136S) |
| EcoRV-HF | New England Biolabs (R3195S) |
| HindIII-HF | New England Biolabs (R0401S) |
| KpnI-HF | New England Biolabs (R3142S) |
| NotI-HF | New England Biolabs (R3189S) |
| XhoI | New England Biolabs (R0146S) |
| NheI-HF | New England Biolabs (R3131S) |
| Q5-DNA Polymerase | New England Biolabs (M0491S) |
| T4 DNA Ligase | New England Biolabs (M0202S) |

3.4 DNA constructs

Table 6 - DNA constructs used for site-directed mutagenesis and transfection

| Coding Protein | Plasmid | Source |
|------------------------------------|-----------------------------|---|
| KAR subunit GluK2 | pcDNA3-GluK2 | Peter Seeburg (MPI, Heidelberg) ¹³⁸ |
| eGFP fusion protein | peGFP-N1 | Clontech #U55762 |
| GABA-A receptor subunit α 1 | pRK5-SEP-GABA-AR α 1 | Tija Jacob & Stephen Moss (Addgene #49168) |
| GABA-A receptor subunit α 2 | pRK5-SEP-GABA-AR α 2 | Tija Jacob & Stephen Moss (Addgene #49169) |

| | | |
|------------------------------------|--|---|
| GABA-A receptor subunit $\alpha 2$ | pCDM8-GABA-AR $\alpha 2$ | Andrea Barberis (IIT, Genova) |
| GABA-A receptor subunit $\beta 1$ | pCDM8-GABA-AR $\beta 1$ | Andrea Barberis (IIT, Genova) (Petrini et al., 2011) |
| GABA-A receptor subunit $\gamma 2$ | pCDM8-GABA-AR $\gamma 2$ | Andrea Barberis (IIT, Genova) (Petrini et al., 2011) |
| Neurologin 2 | pcDNA3-NL2 | Stéphane Jamain (MPI, Göttingen) (Poulopoulos et al., 2009) |
| TARP $\gamma 2$ -mEos2 | pcDNA3- $\gamma 2$ -mEos2 | Daniel Choquet (CNRS, Bordeaux) |
| TARP $\gamma 2$ -eGFP | pcDNA3- $\gamma 2$ -eGFP | Daniel Choquet (CNRS, Bordeaux) |
| TARP $\gamma 2$ | pcDNA3- $\gamma 2$ | Daniel Choquet (CNRS, Bordeaux) |
| TARP $\gamma 8$ -mEos2 | pcDNA3- $\gamma 2$ -mEos2 | Daniel Choquet (CNRS, Bordeaux) |
| TARP $\gamma 8$ -eGFP | pcDNA3- $\gamma 2$ -eGFP | Daniel Choquet (CNRS, Bordeaux) |
| TARP $\gamma 8$ | pcDNA3- $\gamma 2$ | Daniel Choquet (CNRS, Bordeaux) |
| tRNA ^{Pyl} /PylRS | pCMV- tRNA ^{Pyl} /NESPylRS ^{AF} | Edward Lemke (EMBL, Heidelberg) ³⁰¹ |
| 4xtRNA ^{Pyl} /PylRS | pNEU-hMbPylRS- 4xU6M15 | Irene Coin (Addgene, #105830) ³⁰² |
| XPH20-eGFP | Xph20 eGFP CCR5TC | Matthieu Sainlos ³⁰³ |
| pTet-On | pTet-On Advanced Vector | Clontech #630930 |
| pBI-Tet | pBI-Tet Vector | Clontech #6152-1 |
| pBI-Tet-eGFP-GluA2- $\gamma 2$ | pBI-Tet-eGFP-GluA2- $\gamma 2$ | Daniel Choquet (CNRS, Bordeaux) |
| pBI-Tet- $\gamma 2$ -mCherry | pBI-Tet- $\gamma 2$ -mCherry | Daniel Choquet (CNRS, Bordeaux) |

| | | |
|----------------------|-----------------------------|--------------------|
| pTRE3G-BI | pTRE3G-BI Vector | Takara Bio #631332 |
| pEF1 α -Tet3G | pEF1 α -Tet3G Vector | Takara Bio #631336 |

3.5 Mammalian and neuronal cell culture

Mammalian cell culture

Labteks were coated with poly-D-Lysine (PDL, 0.1 mg/ml; Sigma-Aldrich, #P6407,) for 1 h at room temperature to ensure HEK293T adherence. Cells were seeded 24 h before transfection on 4-well Lab-Tek II chambered cover slides (Nunc, #155409) with a concentration of 1×10^5 cells per well. Cell cultures were maintained in an incubator with 5% CO₂ at 37°C.

HEK293T cells were purchased from the German Collection of Microorganisms and Cell Cultures (Germany, #ACC635). Cells were cultured in T25-culture flasks (Thermo Fisher, #156340) supplied with Dulbeccos's Modified Eagle's Medium (DMEM, Sigma-Aldrich, #D5796) supplemented with FCS (10 %; Sigma-Aldrich, #F7524) and Pen-Strep (1 %; Sigma-Aldrich, #P4333).

Hippocampal primary neurons

Primary neurons for clickable GABA-A receptor experiments were prepared in Genova as described previously³⁰⁴. Experiments involving primary neuronal cultures were conducted in agreement with the rules of the European Communities Council (Directive 2010/63/EU of 22 September 2010). All experiments were authorized by the Italian Ministry of Health and in accordance with the guidelines of the Italian Institute of Technology (IIT). Primary hippocampal neurons were isolated from P0-P1 C57BL/6J mice. Neurons were seeded with a density of 70×10^3 cells/cm² on PDL coated high precision coverslips (18 mm diameter; Roth). Cells were cultured in Neurobasal-A medium (Thermo Fisher) supplied with B-27 (2%; Thermo Fisher), Glutamax (1%; Thermo Fisher) and gentamycin (5 μ g/ml; Sigma-Aldrich) in an incubator (37°C, 7.4 % CO₂). Culture medium was exchanged two times a week with pre-equilibrated Neurobasal medium.

Dissociated neurons for clickable TARP experiments were prepared in Bordeaux as described previously^{305, 308}. Gestant rat females were purchased weekly (Janvier Labs, Saint-Berthevin, France). Rats were treated and euthanized in accordance with European ethical guidelines and protocols of the local ethics committee office 50. Hippocampal neurons were prepared from either sex of E18 Sprague-Dawley rat embryos. Primary neurons were seeded at a density of 25×10^4 cells on PLL (0.1 mg/ml) coated coverslips (18 mm diameter; Marienfeld Superior,

#0117580). Neurons were cultured in Neurobasal Plus Medium (Thermo Fisher) supplied with GlutaMAX (0.5 mM; Thermo Fisher) and 1x B-27 Plus Supplement (Thermo Fisher). 72 hours later, Cytosine β -D-arabinofuranoside (2 μ M; Sigma Aldrich) was supplemented to the medium. Neurons were kept in an incubator at 37°C with 5% CO₂ up to 18 days. Astrocytes feeder layers were isolated from the same embryos. 20x10³ to 40x10³ cells were plated and cultured in Minimum Essential Medium (Thermo Fisher) supplied with glucose (4.5 g/L), GlutaMAX (2 mM) and heat-inactivated horse serum (10%) for 14 days.

3.6 Laboratory devices

| Device | Company/Model |
|----------------------------|--------------------------------|
| Autoclave | Zirbus LVSA 50/60 |
| PCR-cycler | Bio-Rad C1000TM Thermal Cycler |
| NanoPhotometer | IMPLEN Pearl NanoPhotometer |
| Incubator shaker | IKA KS 4000i control |
| Scale | Sartorius TE412 |
| Sterile filter 0.2 μ m | Sartorius |
| Syringes | Braun |
| pH-Meter | Mettler TOLEDO |

3.7 Software

OriginPro 2016G (OriginLab, USA)

ZENblack 2.3 (Zeiss, Germany)

Fiji³⁰⁶

Pymol

rapidSTORM 3.3

3.8 Methods for mutagenesis and amplification of plasmids

PCR for site directed mutagenesis

PCR was used for introduction of amber stop codons or modification of restriction sites of plasmids. The reaction solution consisted of the following components:

Table 7 - PCR reaction solution

| Component | Amount |
|----------------------------------|---------------------------------|
| Q5 reaction buffer (5x) | 10 μ l |
| dNTPs (25 mM) | 1 μ l |
| Forward Primer (125 ng/ μ l) | 1 μ l |
| Reverse Primer (125 ng/ μ l) | 1 μ l |
| Plasmid DNA | 100 ng |
| Q5 HF-Polymerase | 1 μ l |
| ddH ₂ O | to a total volume of 50 μ l |

PCRs were conducted using the following protocol of the Thermo-Cycler:

| Step | Phase | Temperature | Duration |
|-------------|----------------------|--------------------|-----------------|
| 1. | Initial denaturation | 98°C | 30 sec |
| 2. | Denaturation | 98°C | 30 sec |
| 3. | Annealing | 55-65°C | 30 sec |
| 4. | Elongation | 72°C | 3 min |
| 5. | Repeat steps 2 to 4 | - | 20x |
| 6. | Cool storage | 4°C | ∞ |

Gel electrophoresis

Gel electrophoresis using an agarose solution (1% in 0.5x TBE buffer) enabled isolation and identification of DNA fragments according to their size. Therefore, the agarose solution was homogenized through heating and subsequently mixed with SafeView, which intercalates with DNA and can be visualized using UV light. The solution was transferred to a gel electrophoresis sled containing a sample comb. The DNA samples were mixed with DNA gel loading dye prior to adding the samples to the gel wells. A DNA ladder with DNA fragments of specific lengths was introduced as reference. The DNA was separated in a running buffer containing 0.5x TBE using an electrical field with \sim 15 V/cm power. Isolated DNA fragments were optically analyzed by an UV-Illuminator.

Molecular cloning

Restriction enzymes were used for insertion or deletion of specific DNA fragments of plasmids. Dependent on the used restriction enzyme, the recommended protocol and buffers as mentioned by the manufacturer were applied. T4 DNA Ligase enabled subsequent ligation of inserted or deleted DNA fragments, when following manufacturer instructions. Subsequently, DNA was amplified by transformation in XL1-Blue E.coli cells.

Transformation and selection of competent bacteria

Transformation was used for selection and amplification of desired DNA constructs in XL1-Blue E.coli cells. Most of the introduced plasmids bear a bacterial origin of replication as well as a gene coding for an antibiotic resistance to ensure an efficient replication. DNA was transformed into XL1-Blue cells using heat shock protocol followed by plating on agar media containing respective antibiotic resistances. Isolated grown colonies were transferred in TY-media containing antibiotic resistances for further amplification prior to DNA isolation.

DNA isolation

Construct DNA was isolated by Mini-preparation or Midi-preparation. The High Pure Plasmid Isolation Kit (Roche) was used for Mini-preparations isolating from 5 ml bacterial culture and subsequent elution in 30 µl. For Midi-preparations the NucleoBond Xtra Midi EF Kit (Macherey-Nagel) was used according to protocol. Concentrations of isolated DNA were determined using a NanoPhotometer (IMPLEN) prior to verification by sequencing (Eurofin Genomics).

Preparation of competent E.coli cells

Chemical competent E.coli cells with high transformation efficiency were produced in collaboration with the group of Dr. Hannes Neuweiler (Biotechnology and Biophysics, Wuerzburg). 8 ml of XL1-Blue start culture were cultivated in TY-medium free from antibiotics, transferred in 800 ml TY-medium and incubated at 37°C. Reaching an optical density (OD_{600nm}) of 0.6 the bacteria solution was cooled at 4°C for 30 min and pelleted subsequently. The pellet was washed in TB-buffer followed by resuspension in 25 ml TB-buffer and adding 25 ml TB-buffer (+ 14 %-DMSO). The suspension was aliquoted in 250 µl sterile reaction tubes, frozen in ethanol-dryed ice and stored at -80°C.

Transfection of mammalian cells

Transfection of HEK293T cells was carried out using the JetPrime Transfection Reagent (Polypus, #114-01) according to manufacturer's protocol. HEK293T cells were seeded on 4-well Lab-Tek II chambered glass slides (Nunc, cat. no. 155409) coated with poly-D-Lysine (Sigma-Aldrich, #P6407, 0.1 mg/ml) the day before transfection. At 70-85% confluency, cells were transfected. A standard transfection solution for expression of target proteins carrying a click site consisted of the following components:

Table 8 - Transfection solution for a single well

| Amount | Component |
|------------|-------------------------------------|
| 500 ng | DNA coding for target protein |
| 500 ng | DNA coding for tRNA/tRNA-Synthetase |
| 2 μ l | JetPrime Transfection Reagent |
| 50 μ l | JetPrime Reaction Buffer |

Additionally, cells were fed the unnatural amino acid (uAA) TCO*-K supplemented to the cell media. Therefore, the uAA was diluted 1:4 with 1M HEPES (pH 8.0) and added at a final concentration of 250 μ M to the cells at the edge of the wells. Transfected cells were maintained in an incubator with 5% CO₂ at 37°C for 24h or 48h depending on transfected constructs and subsequently labeled with tetrazine-fluorophore fusions.

Transfection of hippocampal primary neurons

TARP γ 2 and γ 8: At DIV 3/4, hippocampal primary neurons were transfected with 100 ng Tet3G/tRNA^{Pyl}, 100 ng pTRE3G-BI PylRS/TARPs (γ 2^{S44*} or γ 8^{S72*}), along with 40 ng eGFP or XPH20 eGFP using lipofectamine 2000. Then at DIV16-18, 250 μ M of unnatural amino acid TCO*-K and 100 ng/ml of doxycycline were supplied to the cell medium. 20 hours later, neurons were washed 3 times with warm Tyrode's solution followed by 3 min incubation in Tyrode's solution supplemented with 1% BSA prior to labeling of neurons³⁰⁸.

GABA-A receptors: Hippocampal primary neurons were transfected at DIV14 with the clickable α 2^{S181} GABA-A receptor and tRNA^{Pyl}/PylRS in 1:2 ratio along with EGFP. Effectene (#301425, Qiagen) was used as transfection reagent following the manufacturer's instructions. TCO*-K (250 μ M) was supplemented to the medium at DIV15 and neurons were labeled at DIV16.

3.9 Fluorescence labeling methods

Labeling of target proteins expressed on mammalian or neuronal cells was conducted using different approaches. All of them underlying the following standard live cell labeling protocols for antibody and tetrazine conjugates:

| Live cell labeling protocol on ice | |
|---|--|
| Antibody | Tetrazine |
| 5 min cell incubation at RT | 5 min cell incubation at RT |
| 10 min cell incubation on ice | 10 min cell incubation on ice |
| 1x washing with cell medium | 1x washing with cell medium |
| 60 min primary antibody incubation on ice (5 $\mu\text{g/ml}$) | 10-60 min H-Tetrazine-dye incubation on ice (1.5-6 μM) |
| 3x washing with PBS | 3x washing with PBS |
| If unconjugated primary antibody: 60 min secondary antibody incubation on ice (5 $\mu\text{g/ml}$) and 3x washing with PBS | |
| 15 min fixation in 4% FA + 0.25% GA in PBS at RT | 15 min fixation in 4% FA + 0.25% GA in PBS at RT |

Additionally, the tetrazine labeling protocol was modified for signal amplification using antibodies:

| Signal amplification using antibodies |
|---|
| 5 min cell incubation at RT |
| 10 min cell incubation on ice |
| 1x washing with cell medium |
| 60 min H-Tet-Digoxigenin incubation on ice (3 μM) |
| 3x washing with PBS |
| 60 min anti-Digoxigenin-dye incubation on ice (5 $\mu\text{g/ml}$) |
| 15 min fixation in 4% FA + 0.25% GA in PBS at RT |

3.10 Microscopy setups

Confocal Laser Scanning Microscopy (CLSM)

Confocal images were acquired using a commercial LSM700 (Zeiss) equipped with a 63x oil immersion objective (1.4 NA) and a 63x water-immersion objective (C-Apochromat, 1.2 NA, Zeiss, 441777-9970) which was used for expansion experiments. Excitation lasers and filters were adjusted for the respective fluorophores. The setup contained solid-state lasers with wavelengths of 488 nm (10 mW), 555 nm (5 mW) and 640 nm (5 mW). Finally, the microscope offered a pixel size of 90 nm.

Structured Illumination Microscopy (SIM)

Super-resolved structured illumination microscopy was conducted using a commercial ELYRA S.1 microscope (Zeiss). The microscope was equipped with a 63x oil immersion objective (1.4 NA) and a 63x water-immersion objective. For excitation two OPSL laser with the wavelengths 488 nm and 561 nm as well as a diode laser with a wavelength of 641 nm were used. The filter sets were adjusted for the respective fluorophores. Structured illumination applying five rotational and five phase variations was used for image recording and subsequent reconstruction in ZEN 2.3 (Zeiss).

Single molecule localization microscopy using *d*STORM

*d*STORM experiments were performed using a customized inverse wide-field setup (Olympus IX-71) with an 60x oil-immersion objective (Olympus, 1.45 NA). Two OPSL lasers with 558 nm or 640 nm wavelength (Genesis MX561-500 STM, Genesis MX639-1000 STM, Coherent) were used for excitation of CF568 or Cy5/AF647 applying 4 kW/cm² irradiation intensity. Laser clean-up filter (567/15, Semrock and 640/10, Chroma), dichroic mirror (FF 410/504/582/669 Brightline, Semrock) and bandpass filters (679/41 BrightLine HC or 607/70 Brightline HC, Semrock) were required for filtering excitation and emission lights. Two electron multiplying CCD cameras (Andor Ixon DU 897) detected emitted signal in 15.000 frames at 15 ms exposure time. A final pixel size of 129 nm (Cy5/AF647) and 131 nm (CF568) was yielded by additional lenses in the emission path. Efficient photoswitching of dyes was achieved using thiol-based switching buffer containing 100 mM MEA (pH 7.4). Image reconstruction was performed with rapidSTORM 3.3²⁷⁵. Chromatic aberration was corrected by elastic transformation matrix implemented in Fiji plugin BunwarpJ³⁰⁷ using embedded TetraspeckTM beads (Z7279, Thermo Fisher) for alignment.

3.11 Click-Expansion microscopy (click-ExM)

Expansion microscopy was carried out on HEK293T cells (seeded on 12 mm coverslips (Hartenstein)) expressing clickable membrane proteins. Stained cells (see 2.8) were incubated in 0.1 mg/ml AcX (solved in 200 mM NaHCO₃) overnight at RT using a humidified chamber. To avoid premature gelation of monomer solution all following steps were performed in ice water, when not indicated differently. Monomer solution for 4x hydrogels (see 2.1) was mixed with TEMED and APS to initiate polymerization. Monomer solution for 10x hydrogels (see 2.1) were degassed for 45 min with nitrogen to prevent oxygen in the solution. Then KPS was added followed by degassing for another 15 min prior to supplementing TEMED. Finally, 70 µl monomer solution (4x and 10x gels) were pipetted on parafilm and coverslips bearing cells were flipped cells-facing-down on the gel droplet. Gels were set in a humidified chamber for 30 min at RT and additional 90 min at 37°C to ensure entire polymerization. Then, gels were digested overnight at RT in digestion buffer containing proteinase K. After that, samples were expanded in ddH₂O until fully expanded. Isotropic expansion was verified by measuring the gel size as well as the equatorial membrane of HEK293T cells pre and post expansion. Expanded gels were cut in smaller pieces and transferred to PDL-coated glass slides (Merck, 734-2055) for CLSM and SIM imaging.

3.12 Conjugation of tetrazines or antibodies

Tetrazine coupling

Tetrazine that could not be purchased with Digoxigenin as conjugate was self-labeled by reaction of 10-fold excess of tetrazine-amine with 100 µg of Digoxigenin-NHS in DMSO supplied with DIPEA (0.1%) at room temperature overnight. Afterwards, the conjugated tetrazine was purified at a high-performance liquid chromatography (Phenomenex Kinetex Biphenyl Core-Shell column) using acetonitril supplied with 0.1% formic acid as eluent A and 95% acetonitrile supplied with 0.1% formic acid as eluent B.

Antibody coupling

Antibodies that were not commercially available with respective dyes were self-conjugated via dye-NHS coupling to primary amines of the antibody (see Table 4). Therefore, 5-fold molar excess of dye-NHS was reacted with at least 25 µg of antibody in 100 mM NaHCO₃ buffer solved in 1x PBS for 3 hours. Afterwards, unreacted dye molecules were separated from antibody-dye conjugates by centrifugation through Zeba Spin Desatling Columns with a

molecular weight cutoff of 7 kDa (Thermo Fisher). Antibody concentration and the degree of labeling (DOL) were determined at the NanoPhotometer. The conjugated antibodies were stored in 0.02% NaN₃ in PBS at 4°C or -20°C following supplier recommendation.

3.13 Data analysis

Confocal images were adjusted in brightness and contrast using FIJI. Cluster analysis of *d*STORM data was performed with a custom written python script from PD Dr. Sören Doose and in close collaboration with him. To identify clusters of localizations a DBSCAN was applied with an epsilon of 20 nm and minPoints of 3 points, meaning that a localization need to have at least three neighbor localizations within a 20 nm radius to be considered as a data point in the observed cluster. This algorithm led to information about localizations per cluster, amount of clusters per area, cluster area and localizations per region of interest (ROI). Furthermore, Ripley's H-function was calculated to distinguish between random distributions of localization clusters and cluster formation of respective experimental data.

4 Results and Discussion

In this work, GCE and subsequent bioorthogonal click labeling were applied to visualize excitatory and inhibitory synaptic proteins in mammalian cells as well as in dissociated neurons. In the first three sections (4.1, 4.2 and 4.3), the establishment of click mutants for synaptic proteins such as KARs (4.1), TARPs (4.2) and GABA-ARs (4.3) and the application in mammalian cells and primary neurons will be described. The fourth part of the work (4.4) will focus on advancing bioorthogonal click chemistry to decipher the single subunit visualization of GABA-A receptors (two α -subunits of GABA-ARs) using methods such as FRET, *d*STORM and click-ExM. At the end of each section, the results will be discussed.

4.1 Bioorthogonal click chemistry visualizes ionotropic kainate receptors (KARs)

4.1.1 Establishment of clickable KAR GluK2 subunits in mammalian cells

The KAR subunit 2 (GluK2) forms tetrameric homo-receptors in the synapse. Here, serine residues at the positions S47, S272, S309 and S343 of the GluK2 cDNA were exchanged to amber stop codons (TAG) via site-directed mutagenesis. All the mutation sites were chosen in unstructured regions in the extracellular domain (ECD) of the receptor based on the PDB model 5KUF. Then, mammalian HEK293T cells were transfected with the click constructs and the 4xtRNA^{Pyl}/PylRS plasmid to ensure incorporation of the supplemented unnatural amino acid TCO*-K. The TCO*-K tagged GluK2 receptor could then be labeled with tetrazine-dyes (Figure 8).

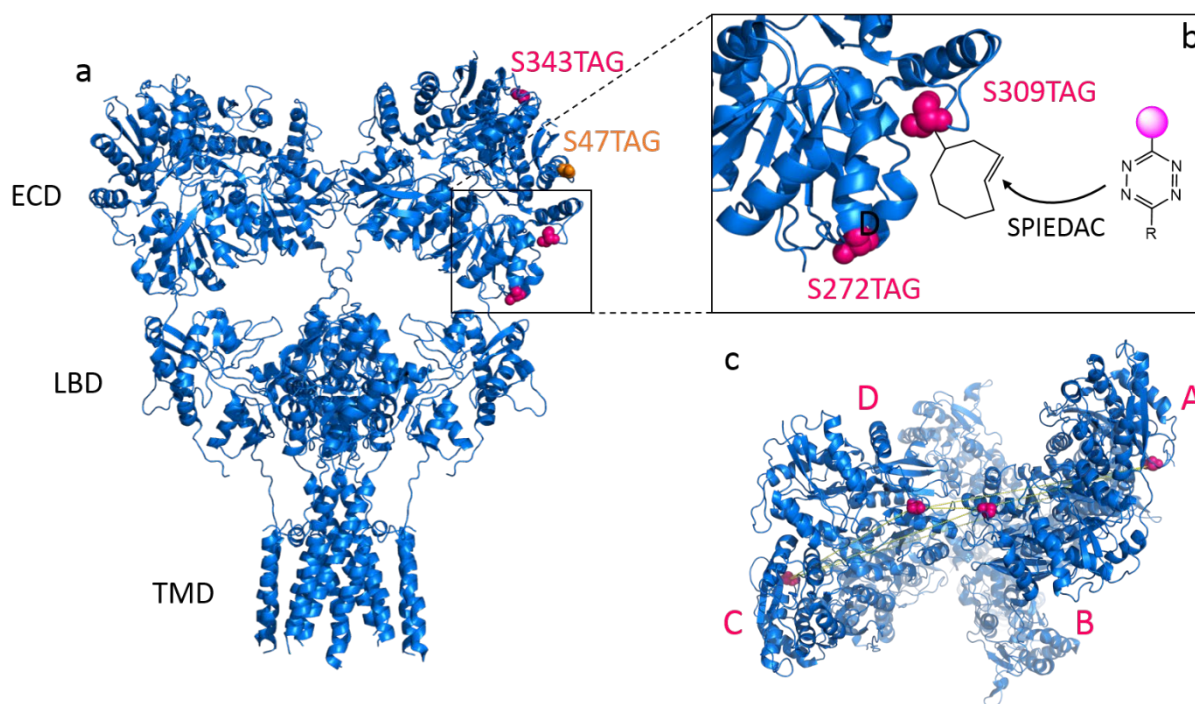


Figure 8 - Bioorthogonal labeling of GluK2 homotetramer. GluK2 receptors comprise a transmembrane domain (TMD), a ligand binding domain (LBD) and an extracellular domain (ECD). (a) Click sites S47TAG, S272TAG, S309TAG and S343TAG were introduced in the ECD of the receptor. Magenta click sites could be labeled sufficiently with tetrazine-dyes, while the orange click site (S47TAG) showed significantly lower fluorescence at the CLSM. (b) Closeup on amber sites S272TAG and S309TAG to illustrate incorporation of the unnatural amino acid TCO*-K and labeling with tetrazine-dyes via SPIEDAC reaction. (c) Distances of S309TAG click sites between GluK2 subunits in the homo-tetramer. Due to the two dimeric formation, the click sites vary in their distances to each other. Measurements in Pymol exhibited the following distances between the four subunits (A, B, C, D): ~1.8 nm (B-D), ~5.8 nm (A-B), ~5.6 nm (C-D), ~7.4 nm (A-D), ~7.4 nm (B-C) and ~11.9 nm (A-C). PDB-ID: 5KUF.

Click mutants were imaged at the confocal laser scanning microscope (CLSM) and evaluated based on the fluorescence signal obtained from click labeled KARs exposed to the surface of HEK293T cells. The mutant S47TAG showed weak surface signal, after labeling with tetrazine Cy5 (H-Tet-Cy5) for 60 min on ice (Figure 9, first panel). All other mutants S272TAG, S309TAG and S343TAG provided strong signal at the cell membrane (Figure 9, first and second panel) with barely unspecific signal in the controls lacking the unnatural amino acid (Figure 9, third panel). eGFP expression of GluK2^{S309}-eGFP provided evidence that only a small amount of clickable receptors was present in the membrane compared to high amounts of receptors in the cytosol. As expected, the GluK2 wildtype (GluK2^{WT}) was predominantly present in the membrane (eGFP channel), but could not be targeted by H-Tet-Cy5 (Figure 9, fourth panel).

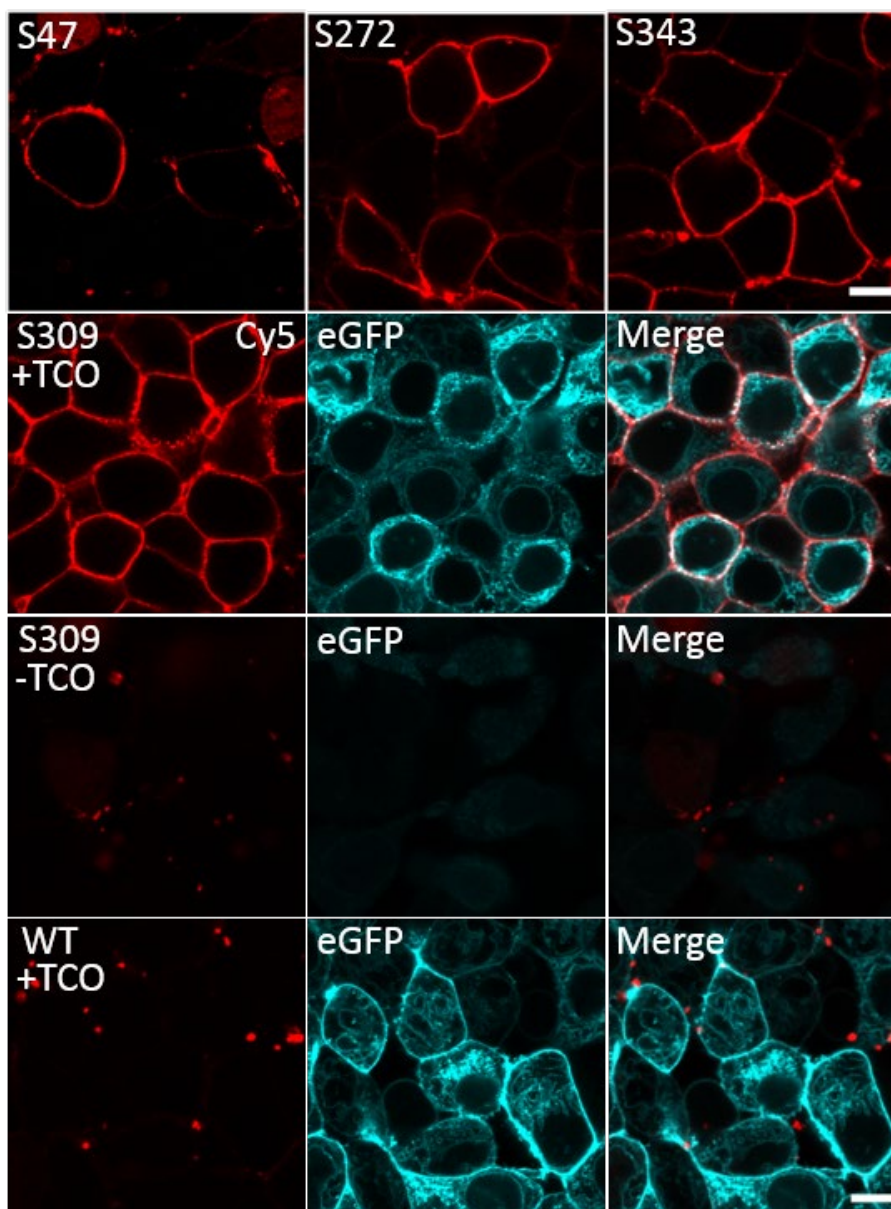


Figure 9 – Specificity of bioorthogonal labeling of clickable GluK2 variants and respective controls. Amber codons were introduced at positions S47TAG, S272TAG, S309TAG and S343TAG. First panel: HEK293T cells expressing clickable GluK2 were labeled with 3 μ M H-Tet-Cy5 (red) for 60 min on ice and imaged at the CLSM. Second panel: HEK293T cells expressing GluK2^{S309}-eGFP and 4xtRNA^{PyI}/PyIRS supplied with TCO*-K were live labeled with H-Tet-Cy5 (red). eGFP fusion protein (cyan) showed high amounts of GluK2 receptors located in the cytosol compared to lower signal in the membrane. Third panel: HEK293T cells lacking the unnatural amino acid TCO*-K exhibited unspecific binding to the cell membrane and only diffuse eGFP expression. Fourth panel: GluK2^{WT}-eGFP constructs exhibited only unspecific labeling when incubated with H-Tet-Cy5 in the presence of TCO*-K, but showed eGFP expression of GluK2 receptors in the membrane. Scale bar 10 μ m.

4.1.2 Comparison of bioorthogonal labeling with antibody labeling

After establishment of suitable click variants, the click labeling approach was compared with conventional antibody labeling of GluK2 in close collaboration with Dr. Gerti Beliu. Most of the commercially available antibodies target GluK2 at C-terminal regions. Due to this, live

labeling of HEK293T cells with H-Tet-Cy5 and primary rabbit-anti-GluK2 antibody (Thermo Fisher, #PA5-32427) followed by secondary goat-anti-rabbit AF488 allowed only sufficient binding of H-Tet-Cy5 to GluK2^{S272} at the cell membrane after fixation with formaldehyde (Figure 10, first panel). To obtain C-terminal antibody-labeling of GluK2, HEK293T cells were first live labeled with H-Tet-Cy5 and then permeabilized with 0.25% Triton prior to primary and secondary antibody labeling of GluK2 (Figure 10, second panel). Besides unspecific binding of the antibody in the cytosol, C-terminal GluK2 was successfully recognized by the antibody in the plasma membrane (cyan).

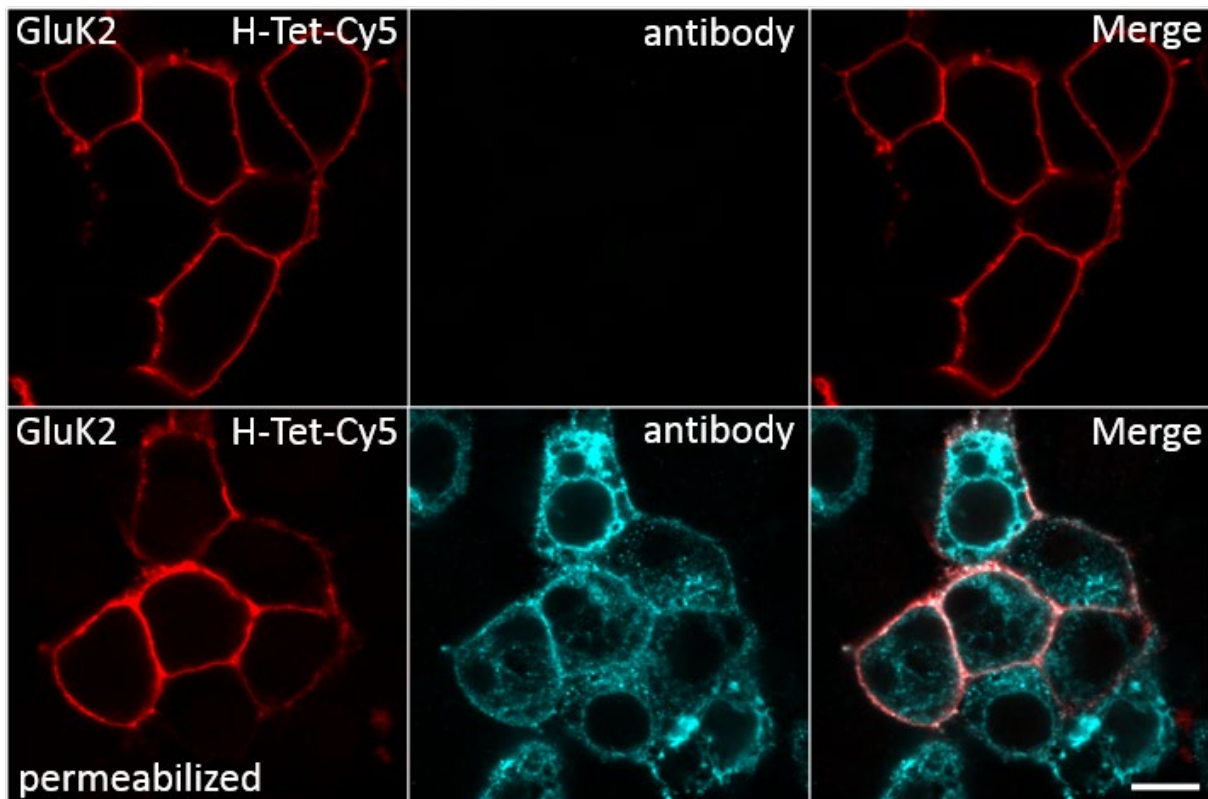


Figure 10 - Comparison of bioorthogonal labeling (red) and antibody labeling (cyan) of GluK2^{S272}. First panel: Live labeling of extracellular GluK2^{S272} with 1.5 μ M H-Tet-Cy5 (left) and 5 μ g/ml anti-GluK2 primary (Thermo Fisher (#PA5-32427)) and 5 μ g/ml goat anti-rabbit AF488 secondary antibody (middle) shows only tetrazine staining in the merged image (right). Second panel: Live labeling with H-Tet-Cy5 prior to permeabilization and anti-GluK2 antibody staining reveals binding of the antibody to C-terminal GluK2 (middle). Additionally, anti-GluK2 antibody binds unspecifically to cytosolic compartments. Scalebar 10 μ m. Adapted with permission²⁵⁹.

The established click variants S272TAG, S309TAG and S343TAG were then used for single molecule localization microscopy to investigate the distribution of GluK2 at the basal membrane of HEK293T cells. To achieve this, GluK2^{S309} receptors were live labeled with H-Tet-Cy5 and fixed with formaldehyde and glutaraldehyde for subsequent *d*STORM imaging

(Figure 11). In the absence of TCO*-K, only unspecific binding of H-Tet-Cy5 to the glass surface and basal membrane was detected (Figure 11, right). Successful incorporation of TCO*-K into GluK2-S309TAG allowed localization of the clickable receptor at the basal membrane with sufficient signal compared to the background (signal to noise) (Figure 11, left).

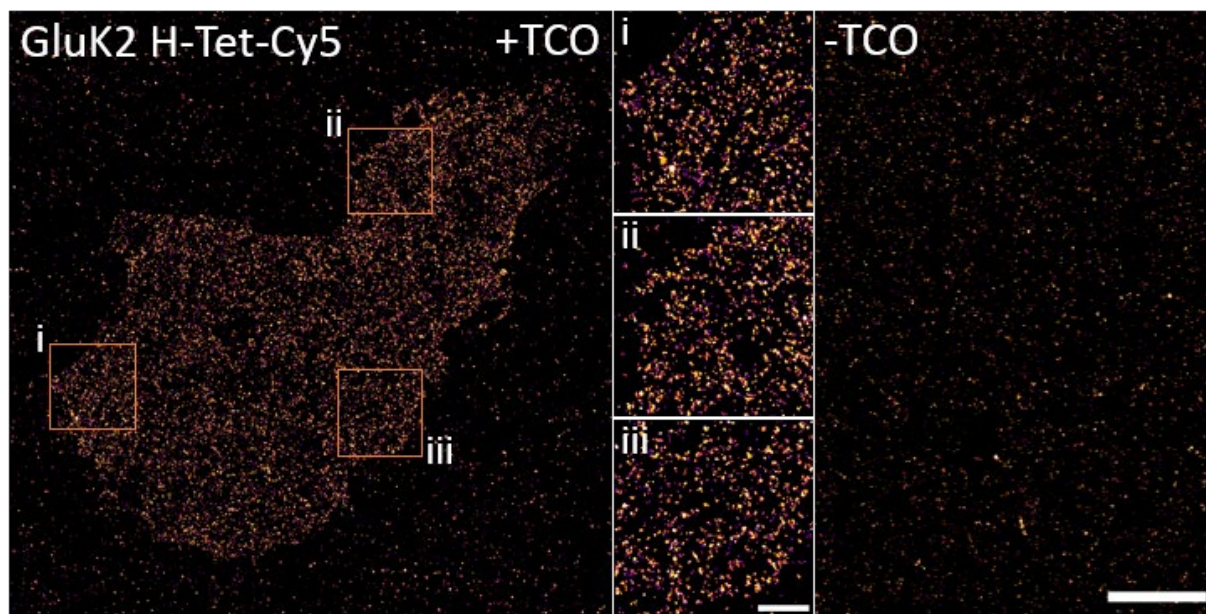


Figure 11 - *d*STORM imaging of click labeled GluK2^{S309} at the basal membrane of HEK293T cells. Left: H-Tet-Cy5 labeled GluK2^{S309} receptors were visualized in the plasma membrane after incorporation of TCO*-K. Insets (i-iii) show distribution of individual GluK2 receptors along the membrane. Right: In the absence of TCO*-K, unspecific signal of H-Tet-Cy5 was localized at the glass surface and basal cell membrane. Imaging was performed in photoswitching buffer containing 100 mM MEA (pH 7.4). Final image reconstruction was conducted with RapidSTORM 3.3. Scalebars 2 μ m; insets 500 nm.

4.1.3 Discussion on bioorthogonal labeling of clickable KARs

GCE allowed successful introduction of the unnatural amino acid TCO*-K into the KAR GluK2 subunit. Importantly, the click sites for amber suppression were introduced at unstructured regions in the extracellular domain for two reasons: First, at unstructured parts of the protein, the risk of impeding the structural and functional properties of the protein by the unnatural amino acid are reduced. Secondly, targeting the extracellular domain of the protein enables extracellular staining with cell-impermeable tetrazine dyes such as H-Tet-Cy5 and therefore prevents unwanted binding of tetrazine-dyes to unbound TCO*-K in the cytosol of the cells. The four clickable-GluK2 constructs were evaluated for labeling specificity with tetrazine-dyes for confocal (Figure 9) as well as super-resolution imaging (Figure 11). Interestingly, the click site closest to the N-terminal region (S47TAG) exhibited the lowest fluorescence signal, when expressed in HEK293T cells and labeled with H-Tet-Cy5 (Figure 9).

This might indicate that incorporation of unnatural amino acids close to the N-terminal signaling peptide of GluK2 is not very efficient and leads to truncated proteins that will not be transported to the cell surface. The amount of truncated intracellular protein as well as surface exposed GluK2 protein could be determined in the future by Western Blot analysis and hence indicate the efficiency of uAA incorporation. When comparing click labeling with conventional antibody labeling, the click approach offers several benefits regarding the target GluK2. Since the antibody recognizes an intracellular epitope of GluK2, living cells cannot be investigated. After permeabilization, the antibody causes severe background in the cytosol besides binding the C-terminal region of GluK2 (Figure 10). In contrast, bioorthogonal labeling enables live cell staining of GluK2 and additionally reduces the linkage-error between fluorophore and receptor down to 1 nm. Furthermore, *d*STORM imaging allowed precise localization of clickable GluK2^{S309} receptors on HEK293T basal membranes. The small H-Tet-Cy5 label creates decent amounts of background signal through sticking to the glass surface (Figure 11). However, GluK2^{S309} molecules exhibited strong signal on basal membranes with a homogenous distribution of the GluK2 receptors and no artificial clustering.

4.2 Bioorthogonal click chemistry visualizes TARPs

In a collaborative effort with Dr. Gerti Beliu and with the group of Prof. Daniel Choquet including Diogo Neto, GCE and bioorthogonal labeling were applied on transmembrane-AMPA-regulatory proteins (TARPs). Cluster analysis was performed with a custom written script from Dr. Sören Doose. In this chapter, γ 2 and γ 8, two TARP proteins that form complexes with AMPA receptors (GluA), were investigated.

4.2.1 Immunohistochemistry of γ 2 and γ 8 TARPs in mammalian and neuronal cells

Conventional immunolabeling using anti- γ 2 Ex2 and anti- γ 8 Ex1 antibodies (red) showed insufficient labeling of extracellular TARP pools of γ 2 (Figure 12, first panel) and γ 8 (Figure 12, second panel) in untransfected hippocampal neurons. Nonetheless, extracellular GluA receptors could be labeled efficiently with anti-GluA1/2/3/4 antibody (cyan) and permeabilization of cells with subsequent labeling of the C-terminus of γ 8 with anti- γ 8 C-tail antibody revealed presence of intracellular γ 8 TARPs (Figure 12, third panel).

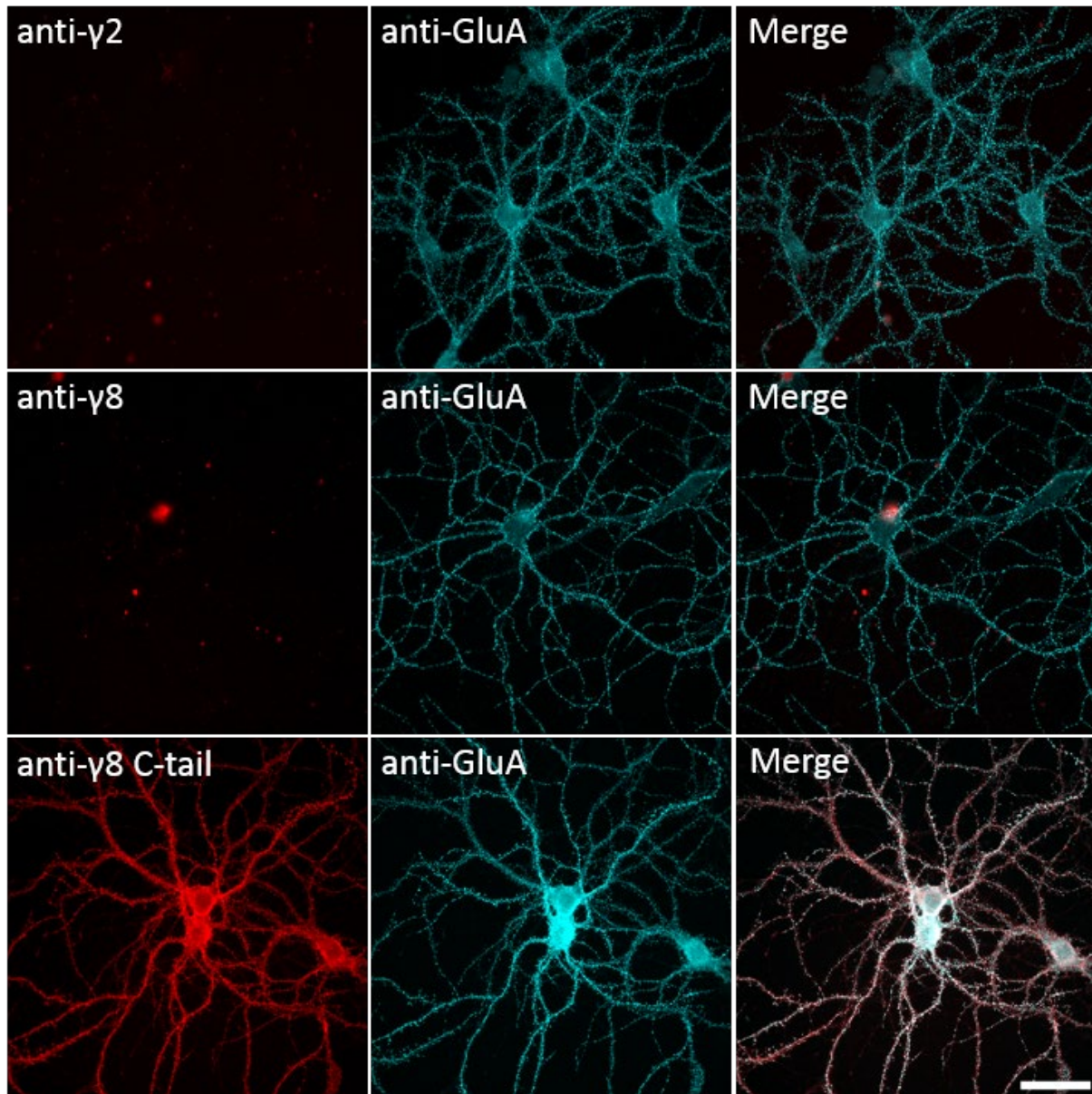


Figure 12 – Antibody labeling of native level of AMPARs (cyan) and TARPs (red) in hippocampal primary neurons imaged on a widefield setup. Native extracellular $\gamma 2$ and $\gamma 8$ TARPs cannot be visualized with anti- $\gamma 2$ AF647 (first panel) or anti- $\gamma 8$ AF647 antibodies (second panel), while extracellular AMPARs were successfully labeled with anti-GluA1/2/3/4 AF568 antibody. Anti- $\gamma 8$ C-tail AF647 antibody, targeting the intracellular epitope of $\gamma 8$ TARPs, allows labeling of intracellular pool of $\gamma 8$ TARPs in untransfected fixed and permeabilized hippocampal neurons (third panel). Scalebar 50 μm . Adapted with permission from³⁰⁸.

To verify the functionality of the antibodies binding the extracellular epitope of $\gamma 2$ (anti- $\gamma 2$ Ex2) and $\gamma 8$ (anti- $\gamma 8$ Ex1), the antibodies were tested in mammalian Cos7 cells overexpressing $\gamma 2^{\text{mEos2}}$ and $\gamma 8^{\text{mEos2}}$. Surface exposed TARPs could be visualized in co-localisation with the mEos2 fusion protein at the basal membrane of Cos7 cells (Figure 13, first and second panel). Additionally, overexpression of $\gamma 2$ -mCherry in hippocampal primary neurons allowed the detection of the mCherry signal and extracellular labeling of $\gamma 2$ with anti- $\gamma 2$ Ex2 antibody

(Figure 13, third panel). However, forcing GluA2 AMPARs to interact with γ 2 TARPs by using the eGFP-GluA2- γ 2 fusion construct, did not result in successful antibody labeling with anti- γ 2 Ex2 (Figure 13, fourth panel).

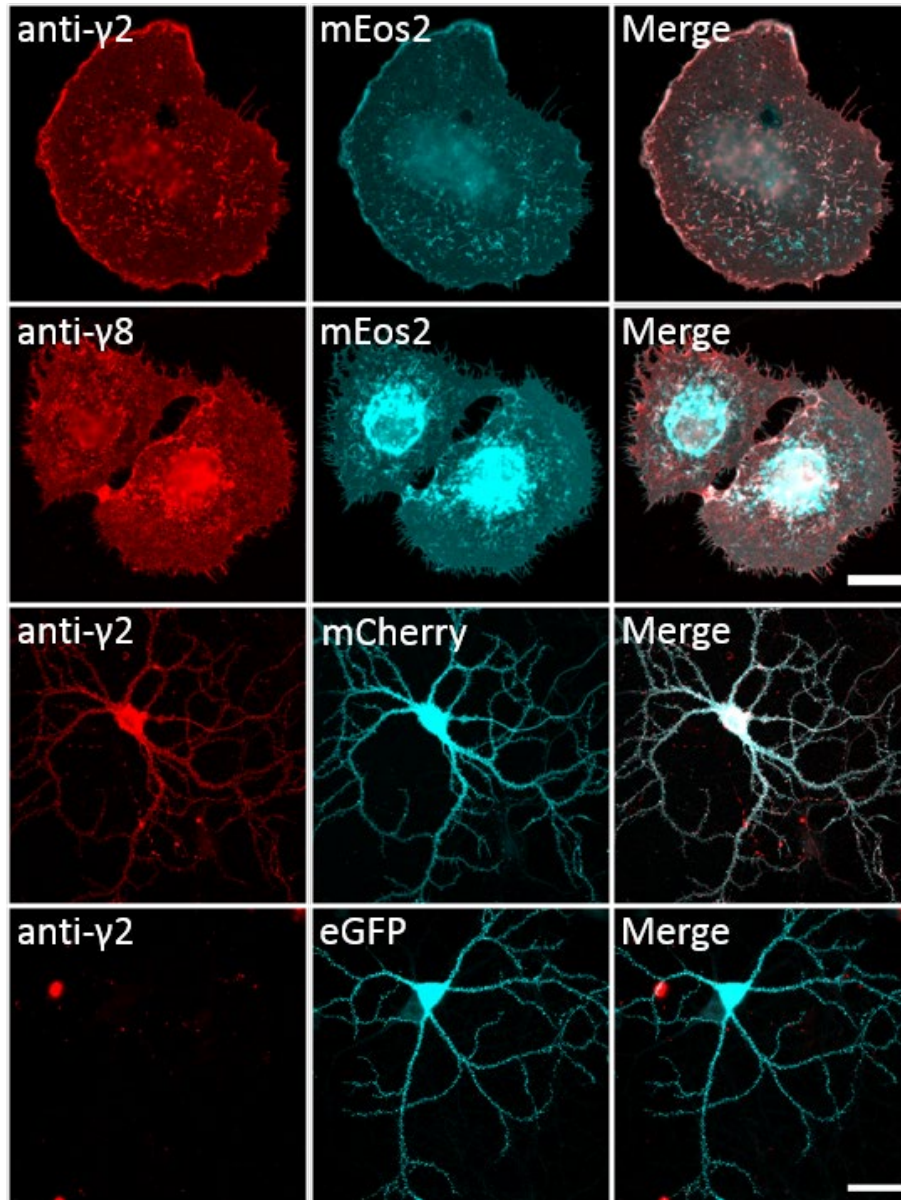


Figure 13 – Specificity of immunohistochemistry of extracellular TARPs overexpressed in mammalian cells and hippocampal primary neurons. Cos7 cells expressing γ 2^{mEos2} (first panel) or γ 8^{mEos2} (second panel) were labeled with anti- γ 2 AF647 antibody or anti- γ 8 AF647 antibody (red). mEos2 fusion protein (cyan) confirmed expression of respective TARPs. Widefield imaging revealed efficient membrane staining of TARPs in Cos7 cells. Neurons overexpressing γ 2-mCherry (third panel) or eGFP-GluA2- γ 2 (fourth panel) were labeled with anti- γ 2 AF647 antibody. Antibody labeling was successful for the γ 2-mCherry construct, while eGFP-GluA2- γ 2 exhibited no anti- γ 2 labeling. eGFP and mCherry (cyan) verified expression of respective constructs. Scalebar 50 μ m. Adapted with permission from³⁰⁸.

4.2.2 Establishment of clickable $\gamma 2$ and $\gamma 8$ TARPs in mammalian cells

Since antibodies showed no success in targeting extracellular TARPs, GCE and bioorthogonal labeling utilizing click chemistry were applied on $\gamma 2$ and $\gamma 8$ TARPs. To achieve site specific labeling of a single unnatural amino acid, amber stop codons were introduced into the extracellular loops of $\gamma 2$ and $\gamma 8$ (Figure 14, right).

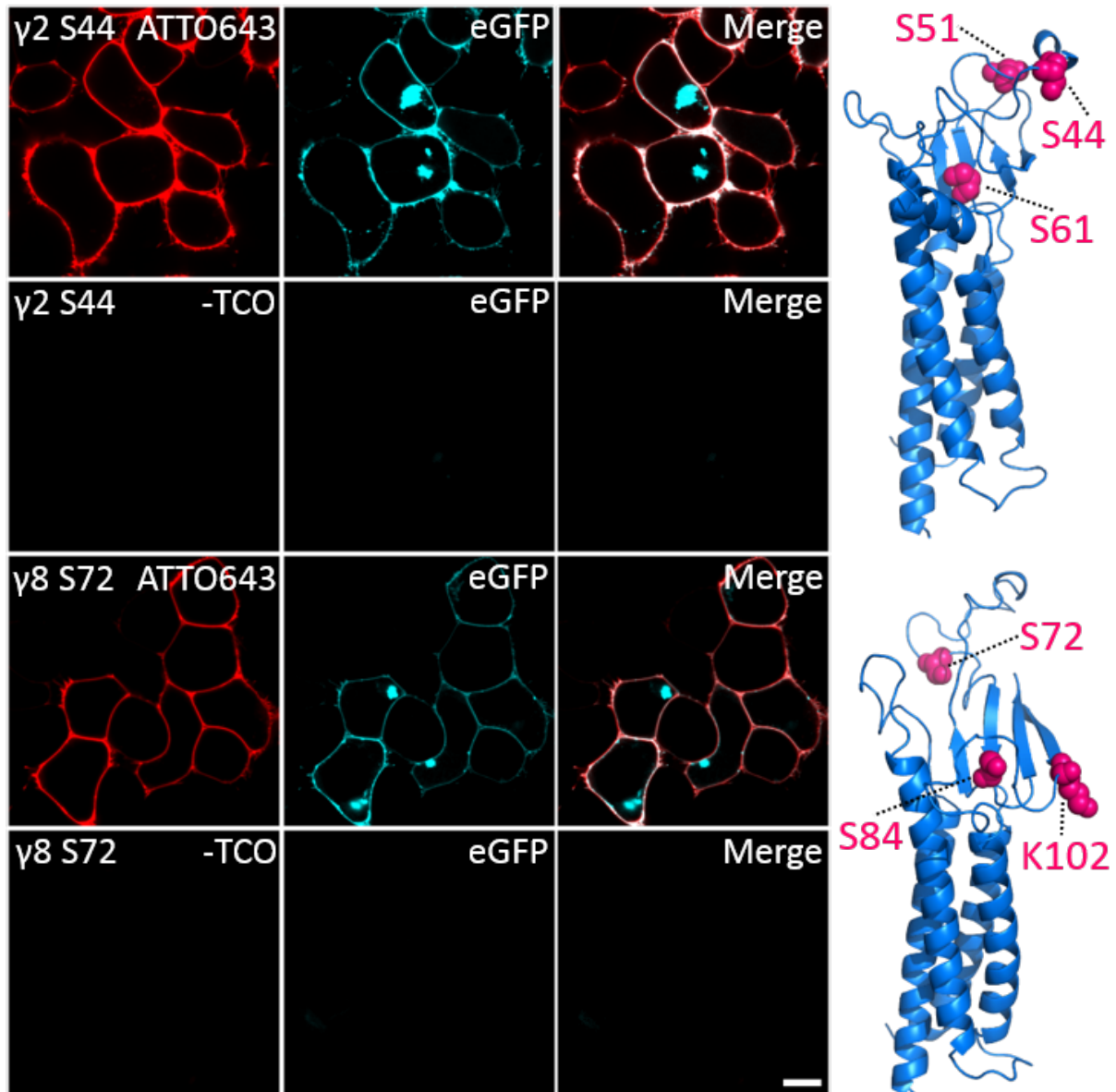


Figure 14 - GCE and bioorthogonal labeling of clickable TARP $\gamma 2$ and $\gamma 8$. Either $\gamma 2^{S44TAG}$ (first panel) or $\gamma 8^{S72TAG}$ TARPs (third panel) expressed on HEK293T cells were live labeled with Pyr-Tet-ATTO643 (red) and live imaged at the CLSM. eGFP fusion protein (cyan) revealed cells with successful incorporation of unnatural amino acid TCO*-K. Control experiments with no TCO*-K supplied to the cell media showed neither tetrazine nor eGFP fluorescence signal of $\gamma 2^{S44TAG}$ (second panel) or $\gamma 8^{S72TAG}$ (fourth panel). Scalebar 10 μm . Click sites for $\gamma 2$ TARPs were introduced at the positions S44TAG, S51TAG and S61TAG based on SWISS model with the PDB template 5WEO (upper model). Protein structure of $\gamma 8$ TARPs was SWISS modelled with the PDB template 5KBT (lower model) and amber stop codons were introduced at the positions S72TAG, S84TAG and K102TAG. Adapted with permission from³⁰⁸.

The protein structure of $\gamma 2$ TARP was SWISS modelled on a template structure (PDB: 5WEO) and then the click positions S44TAG, S51TAG and S61TAG were incorporated by site directed mutagenesis (Figure 14, upper model). All mutants were expressed in mammalian HEK293T cells coexpressed with 4xtRNA/PylRS and supplied with TCO*-K for successful introduction of unnatural amino acids at amber stop sites. The three click sites were all accessible for tetrazine-dye labeling and imaging at the CLSM showing similar overall fluorescence intensities (Figure 15). $\gamma 2^{\text{WT}}$ TARPs were also tested for specificity of tetrazine labeling and showed nearly no unspecific binding to the cell surface (Figure 15, fourth panel).

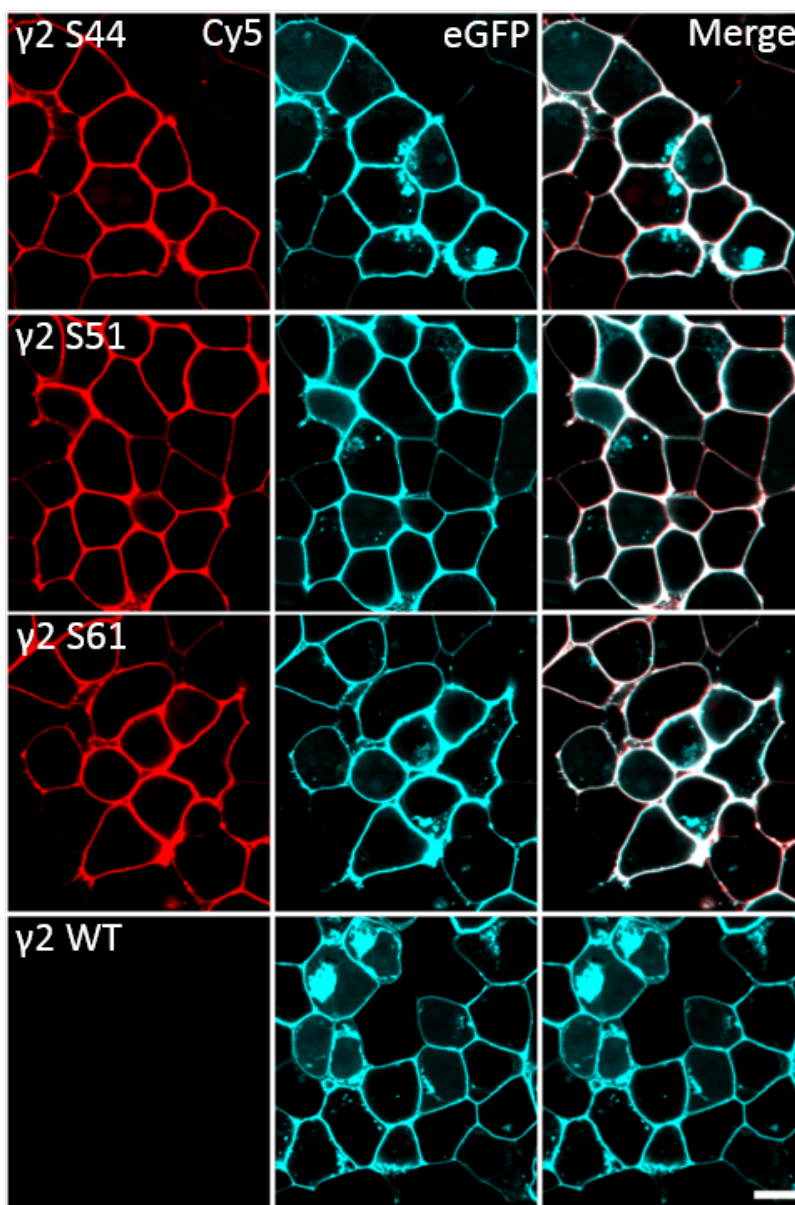


Figure 15 - GCE and bioorthogonal labeling of clickable $\gamma 2$ -eGFP TARPs. HEK293T cells were transfected with eGFP variants of $\gamma 2^{\text{S44TAG}}$ (first panel), $\gamma 2^{\text{S51TAG}}$ (second panel), $\gamma 2^{\text{S61TAG}}$ (third panel) and $\gamma 2^{\text{WT}}$ (fourth panel) together with 4xtRNA^{Pyl}/PylRS in the presence of TCO*-K. TARPs were labeled with 1.5 μM H-Tet-Cy5 (red) and all mutants exhibited similar fluorescence signal in the equatorial membrane of HEK293T cells. The expressed eGFP fusion protein is displayed in cyan. $\gamma 2^{\text{WT}}$

TARPs showed no tetrazine signal even when cells were supplied with TCO*-K, but expression of $\gamma 2^{\text{WT}}$ could be confirmed by eGFP fluorescence. Scalebar 10 μm . Adapted with permission from³⁰⁸.

$\gamma 2^{\text{S44TAG}}$ TARPs on HEK293T cells were live labeled with Pyr-Tet-ATTO643 (red) and recorded under living conditions at the CLSM. The cells showed efficient signal in the cell membrane besides the expression of the eGFP fusion protein (cyan) (Figure 14, first panel). Control experiments with no supplied TCO*-K exhibited neither Pyr-Tet-ATTO643 nor eGFP surface signal (Figure 14, second panel). Similar to generation of clickable $\gamma 2$ TARPs, the protein structure of $\gamma 8$ TARP was also calculated using SWISS model based on the PDB model 5KBT (Figure 14, lower model) and click sites were identified at the extracellular positions S72TAG, S84TAG and K102TAG. All click sites could be labeled with H-Tet-Cy5, when expressed on HEK293T cell surfaces. Cells transfected with $\gamma 8^{\text{K102TAG}}$ showed lower fluorescence compared to the other click variants (Figure 16). Additionally, $\gamma 8^{\text{S72TAG}}$ TARPs were live labeled with Pyr-Tet-ATTO643 and live imaged at the CLSM. When supplied with TCO*-K, HEK293T cells exhibited sufficient membrane labeling of $\gamma 8^{\text{S72TAG}}$ in the eGFP (cyan) and tetrazine channel (red) (Figure 14, third panel). Omitting TCO*-K led to no surface signal (Figure 14, fourth panel).

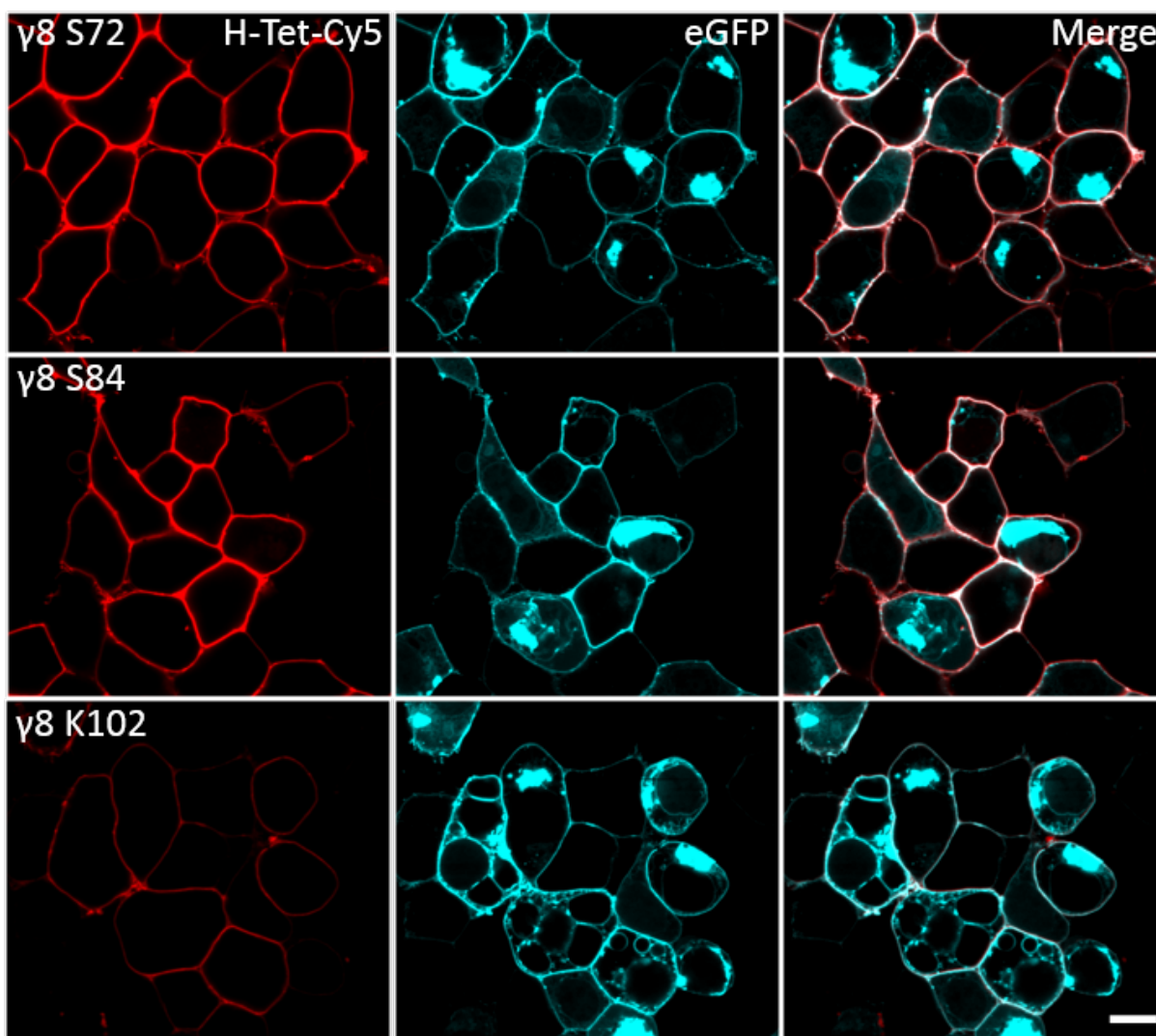


Figure 16 - GCE and bioorthogonal labeling of clickable $\gamma 8$ -eGFP TARPs. HEK293T cells were transfected with eGFP variants of $\gamma 2^{S72TAG}$ (first panel), $\gamma 2^{S84TAG}$ (second panel) and $\gamma 2^{K102AG}$ (third panel), together with 4xtRNA^{Pyl}/PylRS in the presence of TCO*-K. TARPs were labeled with 1.5 μ M H-Tet-Cy5 (red) and the expressed eGFP fusion protein is displayed in cyan. $\gamma 2^{S72TAG}$ and $\gamma 2^{S84TAG}$ revealed efficient expression of clickable TARPs at HEK293T cell surfaces, while $\gamma 2^{K102AG}$ exhibited significantly lower fluorescent signal. In comparison to clickable $\gamma 2$ TARPs, the amount of cytosolic eGFP of clickable $\gamma 8$ TARPs was higher. Scalebar 10 μ m. Adapted with permission from³⁰⁸.

4.2.3 GCE and bioorthogonal labeling of clickable TARPs in neurons

Next, the established click mutants, in particular $\gamma 2^{S44TAG}$ and $\gamma 8^{S72TAG}$, were taken for transfection of hippocampal primary neurons. The neurons were transfected at DIV 3-4 with clickable TARPs and respective 4xtRNA^{Pyl}/PylRS using a doxycycline inducible system. The expression of clickable TARPs was then initiated at DIV 16-17 by application of doxycycline and supplied TCO*-K was subsequently incorporated at the respective amber click sites. 24h later, primary neurons were labeled with Pyr-Tet-AF647 and imaged at a spinning disc confocal microscope (Figure 17). eGFP signal (cyan) confirmed positively transfected neurons and

Pyr-Tet-ATTO643 showed efficient labeling of extracellular $\gamma 2^{S44TAG}$, as well as $\gamma 8^{S72TAG}$ TARPs. Click labeling of $\gamma 2$ TARPs resulted in concentration of tetrazine signal to dendritic spines compared to the rest of dendritic segments (Figure 17, first panel). By contrast, clickable $\gamma 8$ TARPs revealed an overall homogenous distribution in the dendrite and spines (Figure 17, second panel).

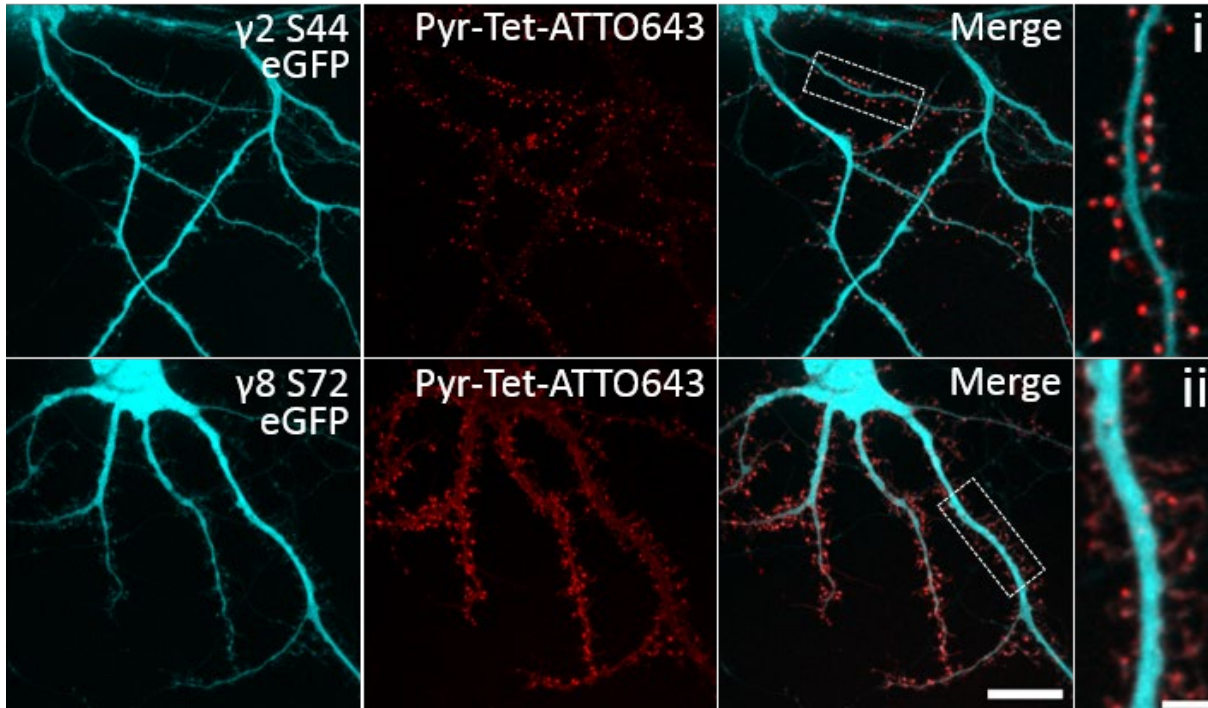


Figure 17 – GCE and bioorthogonal labeling of clickable TARPs in hippocampal primary neurons imaged at a spinning disk confocal setup. Dissociated neurons expressing $\gamma 2^{S44TAG}$ (first panel) or $\gamma 8^{S72TAG}$ (second panel) along with eGFP (cyan) were live labeled with Pyr-Tet-ATTO643 (0.5 μ M; red) and imaged under living conditions. Magnified areas show primary location of $\gamma 2^{S44TAG}$ at dendritic spines (i), while $\gamma 8^{S72TAG}$ was distributed equally in dendrite and spines (ii). Scalebar 20 μ m (overview) and 4 μ m (i, ii). Adapted with permission from³⁰⁸.

4.2.4 dSTORM imaging and cluster analysis of clickable TARPs in neurons

To investigate the distribution of TARPs in primary neuron cultures in higher detail, dSTORM experiments were performed on clickable $\gamma 2$ and $\gamma 8$ TARPs. Hippocampal primary neurons expressing $\gamma 2^{S44TAG}$ or $\gamma 8^{S72TAG}$ and the PSD95 marker XPH20-eGFP were labeled with Pyr-Tet-AF647 and 2D imaging was performed at a dSTORM setup (Figure 18). Again, $\gamma 2^{S44TAG}$ TARPs (5 neurons, 3 independent experiments), showed accumulated localizations in the spinal areas (Figure 18, i-iii), while $\gamma 8^{S72TAG}$ (5 neurons, 4 independent experiments) revealed a similar distribution of TARPs in the dendrites and spines (Figure 18, iv-vi). Pyr-Tet-AF647 signal colocalized with the eGFP fluorescence obtained from XPH20 and allowed identification of positively transfected neurons.

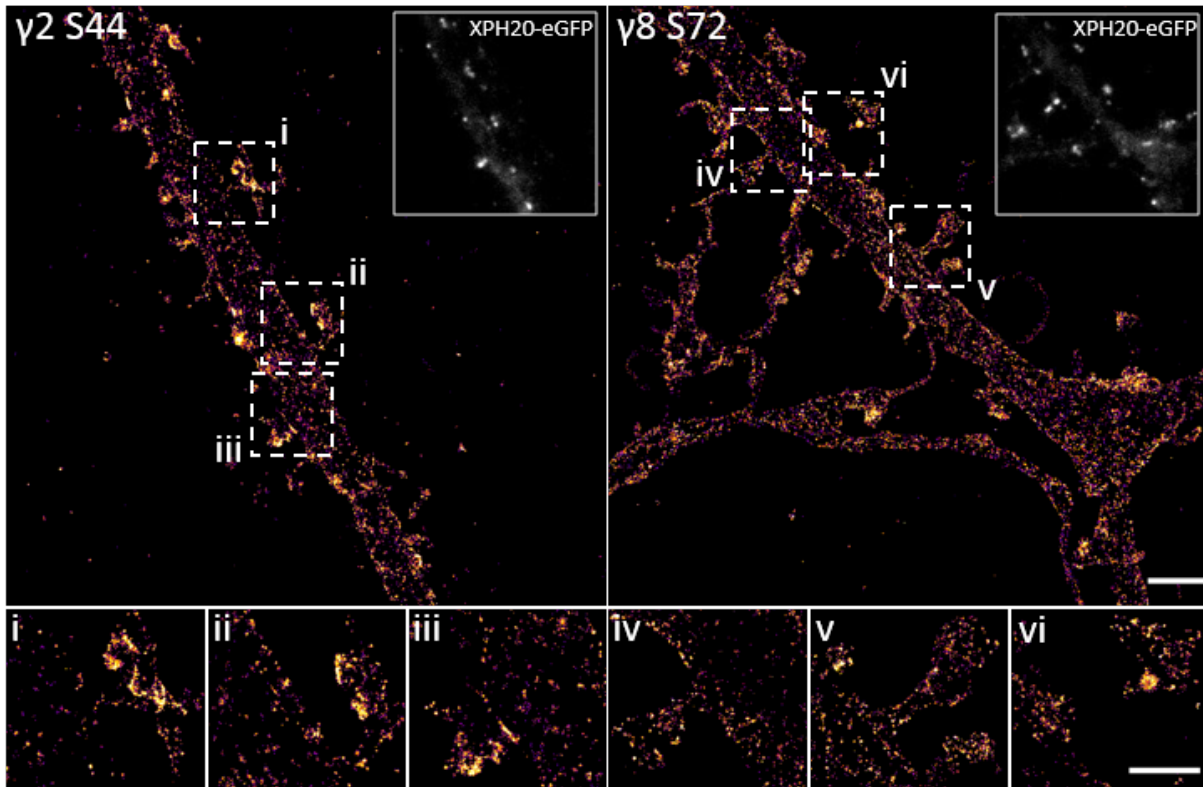


Figure 18 – dSTORM imaging of clickable TARPs in hippocampal primary neurons. Dissociated neurons expressing either $\gamma 2^{S44TAG}$ (left) or $\gamma 8^{S72TAG}$ (right) along with 4xtRNA^{PyI}/PyIRS and XPH20-eGFP were labeled with 0.5 μ M Pyr-Tet-AF647 prior to dSTORM acquisitions. Insets show distribution of $\gamma 2^{S44TAG}$ TARPs (i-iii) and $\gamma 8^{S72TAG}$ TARPs (iv-vi) at spinal areas compared to the dendrite. $\gamma 2$ TARPs showed higher localization density at dendritic spines compared to the respective dendrite, while $\gamma 8$ TARPs were distributed with similar molecule densities all over the neuron. Scalebar: Overview 2 μ m; Insets 1 μ m. Adapted with permission from³⁰⁸.

Next, the dSTORM localization data were subjected to quantitative cluster analysis of clickable $\gamma 2^{S44TAG}$ (here described as $\gamma 2^{S44*}$) (red) and $\gamma 8^{S72TAG}$ (here described as $\gamma 8^{S72*}$) (blue) TARPs at extrasynaptic (light) and synaptic (dark) regions of interest (ROIs) (Figure 19). First, extrasynaptic and synaptic ROIs were selected with a similar size to ensure comparable cluster analysis of clickable $\gamma 2$ and $\gamma 8$ TARPs (Figure 19, d). Localizations per nm² (localization density) were determined and exhibited slightly lower localization densities for $\gamma 2^{S44*}$ ($(0.10 \pm 0.01) \cdot 10E-3 \text{ nm}^{-2}$, n = 50, light red) at extrasynaptic sites compared to $\gamma 8^{S72*}$ ($(0.29 \pm 0.03) \cdot 10E-3 \text{ nm}^{-2}$, n = 52, light blue) (Figure 19, a). Additionally, the localization densities of $\gamma 2^{S44*}$ at synaptic areas ($(0.93 \pm 0.06) \cdot 10E-3 \text{ nm}^{-2}$, n = 104, dark red) were higher in comparison to synaptic $\gamma 8^{S72*}$ ($(0.60 \pm 0.03) \cdot 10E-3 \text{ nm}^{-2}$, n = 102, dark blue). This resulted in an overall localization density ratio between synaptic and extrasynaptic ROIs of 9.0 ± 1.4 for $\gamma 2^{S44*}$ TARPs and of 2.1 ± 0.3 for $\gamma 8^{S72*}$ TARP molecules (Figure 19, a, inset). The higher spine enrichment of $\gamma 2^{S44*}$ compared to $\gamma 8^{S72*}$ led to further investigations on localization clusters

present in synaptic and extrasynaptic areas (Figure 19, b, c). DBSCAN analysis using parameter epsilon of 20 nm and minPoints of 3 allowed identification of localization clusters with the following cluster properties: localization per cluster (Figure 19, b) and cluster size (Figure 19, c). Extrasynaptic $\gamma 2^{S44*}$ and $\gamma 8^{S72*}$ as well as synaptic $\gamma 8^{S72*}$ TARPs exhibited similar localizations per cluster, when displayed as a probability density function (Figure 19, b). Only $\gamma 2^{S44*}$ in synaptic areas (dark red) showed clusters with significantly more localizations per cluster. Interestingly, this can also be observed in the cluster areas per cluster: $\gamma 2^{S44*}$ alone shows clusters with a cluster area $> 0.02 \mu\text{m}^2$ corresponding to cluster sizes with a diameter $> 80 \text{ nm}$ (Figure 19, c). The amount of clusters per μm^2 (cluster density) revealed higher cluster densities for $\gamma 8^{S72*}$ at extrasynaptic ($20 \pm 2 \mu\text{m}^{-2}$) and synaptic ROIs ($38 \pm 1 \mu\text{m}^{-2}$) compared to $\gamma 2^{S44*}$ TARPs (extrasynaptic: $8 \pm 0.8 \mu\text{m}^{-2}$, synaptic: $26 \pm 1 \mu\text{m}^{-2}$), when observing clusters with less than 100 localizations per cluster (Figure 19, b, left inset). Cluster densities with > 100 localizations per cluster could be detected for synaptic $\gamma 2^{S44*}$ ($1.93 \pm 0.19 \mu\text{m}^{-2}$), while synaptic $\gamma 8^{S72*}$ ($0.21 \pm 0.06 \mu\text{m}^{-2}$) and extrasynaptic $\gamma 2^{S44*}$ ($0.01 \pm 0.01 \mu\text{m}^{-2}$) as well as $\gamma 8^{S72*}$ ($0.03 \pm 0.01 \mu\text{m}^{-2}$) showed nearly no clusters (Figure 19, b, right inset).

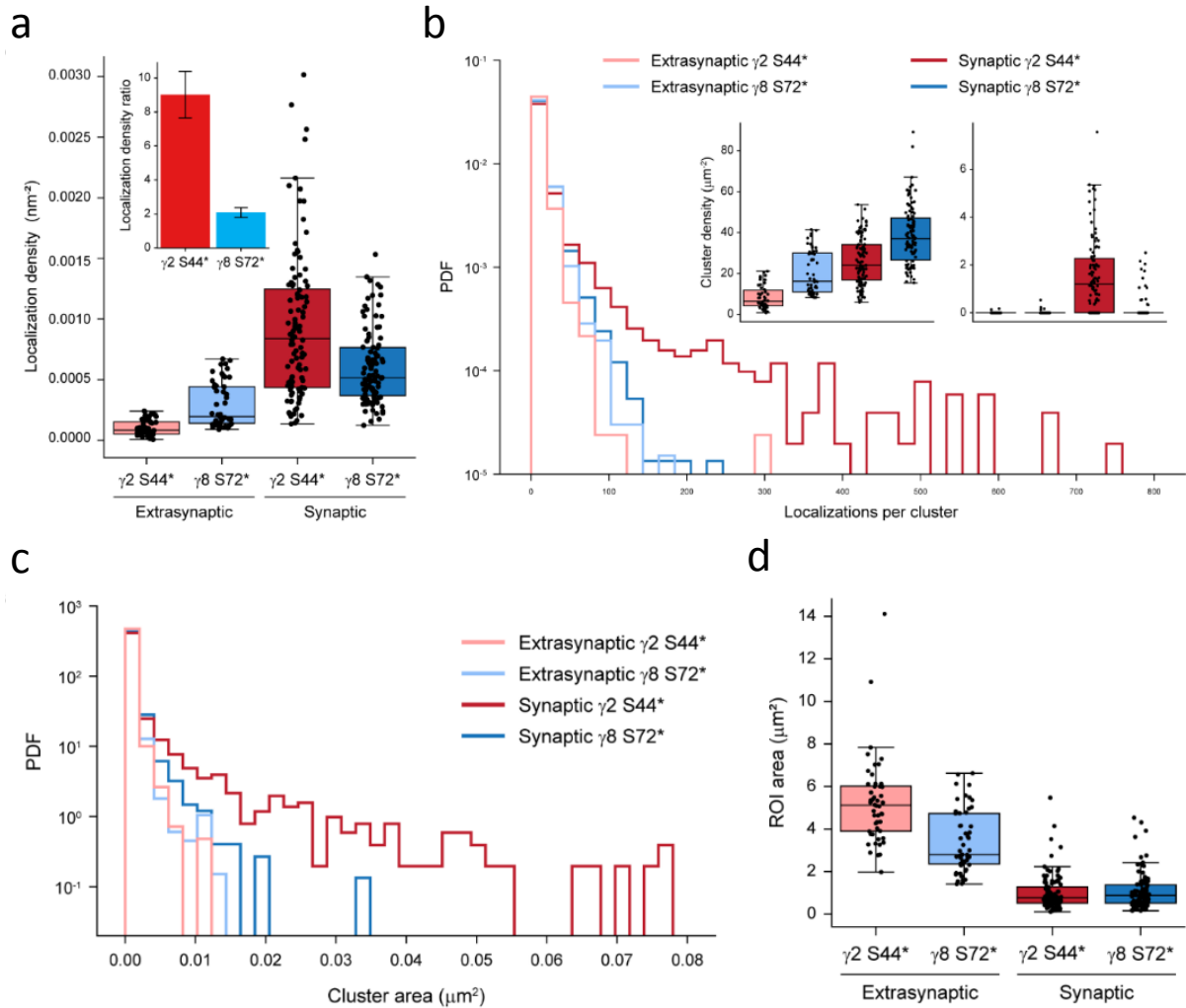


Figure 19 – DBSCAN cluster analysis of clickable TARPs based on dSTORM localizations. (a) Detected localizations per area (localization density (nm²)) for extrasynaptic and synaptic $\gamma 2^{S44^*}$ and $\gamma 8^{S72^*}$. Localization densities were higher in synaptic areas compared to extrasynaptic ROIs for both TARPs. $\gamma 2^{S44^*}$ TARPs revealed higher amounts of localizations in the synapse and lower localization densities at the extrasynapse compared to $\gamma 8^{S72^*}$, leading to a higher synaptic to extrasynaptic ratio of localization densities for $\gamma 2^{S44^*}$ (inset). (b) DBSCAN analysis revealed more localizations per identified localization cluster only for synaptic $\gamma 2^{S44^*}$ TARPs, displayed as probability density function (PDF). Cluster densities were slightly higher for $\gamma 8^{S72^*}$ compared to $\gamma 2^{S44^*}$ in synaptic and extrasynaptic areas when analyzing smaller clusters (0-100 localizations per cluster) (inset left). Clusters that exhibited >100 localizations per cluster could only be detected in synaptic $\gamma 2^{S44^*}$ TARPs (inset right). (c) PDF of cluster areas (μm²) of extrasynaptic and synaptic clickable TARPs. Only synaptic $\gamma 2^{S44^*}$ showed clusters with larger cluster areas compared to all other TARP localization clusters. (d) For comparability, similar sizes of regions of interest (ROI areas) were selected for DBSCAN analysis of extrasynaptic $\gamma 2^{S44^{TAG}}$ and $\gamma 8^{S72^{TAG}}$ as well as synaptic $\gamma 2^{S44^{TAG}}$ and $\gamma 8^{S72^{TAG}}$. Adapted with permission from³⁰⁸.

Additionally, cluster formation of clickable TARPs was analyzed using a Ripley H's function (Figure 20). Experimental data was compared to randomized CSR simulations as well as the Neyman-Scott calculation, which considers the multiple blinking of single fluorophors in the cluster analysis. Clickable extrasynaptic TARPs $\gamma 2^{S44^*}$ and $\gamma 8^{S72^*}$ and also synaptic $\gamma 8^{S72^*}$

exhibited similar distributions as the Neyman-Scott simulations and therefore revealed no clustered molecules in the ROIs. Only $\gamma 2^{S44*}$ TARP molecules at synapses showed clusters with bigger cluster sizes compared to all other approaches.

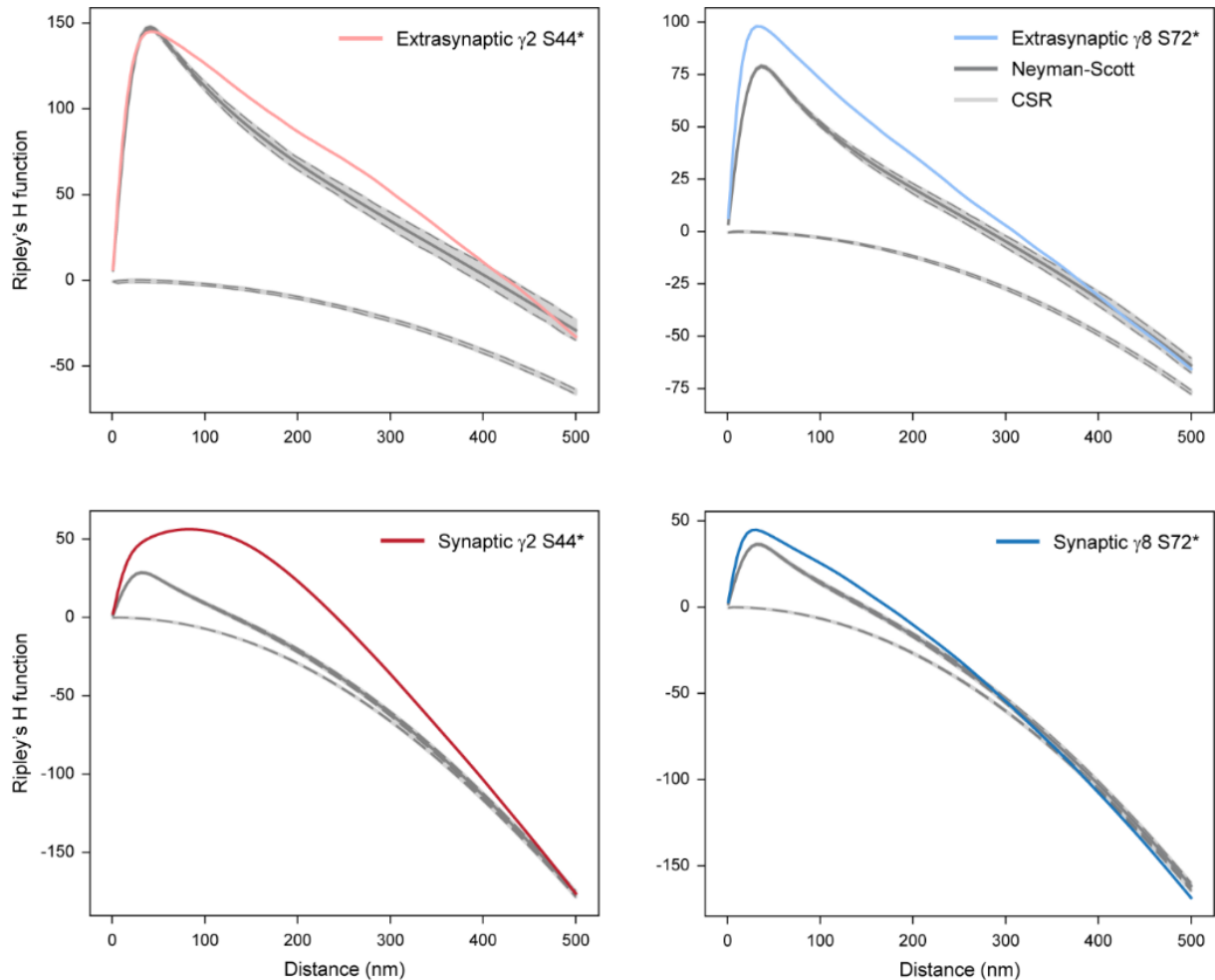


Figure 20 - Ripley's H-function of clickable $\gamma 2$ and $\gamma 8$ TARPs localized in synaptic and extrasynaptic regions of interest. Localization clusters of $\gamma 8^{S72*}$ (blue) exhibit similar cluster sizes in synaptic (dark) and extrasynaptic (light) areas compared to extrasynaptic $\gamma 2^{S44*}$ TARPs (light red). These TARPs show random distributions with a cluster size of ~ 20 nm. Only synaptic $\gamma 2^{S44*}$ TARPs (dark red) reveal non-random cluster distributions with a maximum at ~ 100 nm cluster size compared to all other approaches. Experimental data was verified by clustered Neyman-Scott process (lower grey lines) and complete spatial randomness (CSR) simulations from 100 replicates. Adapted with permission³⁰⁸.

4.2.5 Discussion on clickable $\gamma 2$ and $\gamma 8$ TARPs

Initial experiments focused on establishing efficient labeling of extracellular $\gamma 2$ and $\gamma 8$ TARPs (Figure 12 and 13). In hippocampal primary neurons, anti- $\gamma 2$ and anti- $\gamma 8$ antibodies were not able to specifically bind $\gamma 2$ and $\gamma 8$ TARPs. This suggests non-functional antibodies or masked epitopes of $\gamma 2$ and $\gamma 8$. Follow-up experiments testing the functionality of the same antibodies on Cos7 cells overexpressing $\gamma 2$ and $\gamma 8$ proved efficient binding of the antibodies. However, even in overexpressed conditions, anti- $\gamma 2$ antibody could not recognize the $\gamma 2$ epitope when $\gamma 2$ was expressed as fusion protein with GluA2 in primary neurons. This strengthens the hypothesis that the $\gamma 2$ -GluA2 complex masks the $\gamma 2$ binding epitope. The fact that overexpressed $\gamma 2$ -mCherry could be labeled with anti- $\gamma 2$ antibody might originate from $\gamma 2$ TARPs outnumbering native AMPAR numbers. Thus, overexpressed $\gamma 2$ TARPs that are not complexed with AMPARs could be targeted by anti- $\gamma 2$ antibodies. Overall, the antibody experiments showed that TARP epitopes in the extracellular loops are masked in TARP-AMPA complexes. This observation is in agreement with the cryo-EM studies revealing the structural organization of $\gamma 2$ and $\gamma 8$ TARPs complexed with AMPA receptors^{116,118,309}. Moreover, the fact that endogenous level of TARPs can not be labeled at extracellular loops with antibodies indicates that all TARPs may be bound in complex with AMPA receptors in neurons. $\gamma 2$ TARPs, for instance, interact solely with GluA receptors and thereby strengthen this hypothesis³¹⁰. To circumvent the labeling issues, small tags such as HA (9 amino acids) or an acceptor peptide (bAP, 15 amino acids) that allows subsequent biotinylation were utilized to target overexpressed TARPs in dissociated neurons at extracellular loops. While these approaches enabled visualization of $\gamma 2$ with monovalent streptavidin (mSA)⁵² and tracking of $\gamma 2$ with anti-HA antibodies^{311,312}, it is likely that these labels targeted overexpressed $\gamma 2$ showing no interaction with AMPA receptors. These labeling methods require overexpression of $\gamma 2$ and additionally target a considerably large epitope (9 or 15 amino acids) with an even bulkier mSA (~4 nm) or antibodies (~10 nm). To circumvent this issue, an advanced labeling technique was established, exploiting GCE and unnatural amino acids in combination with bioorthogonal labeling with tetrazine dyes. This method allowed site-specific labeling of a single amino acid in TARP molecules with an overall linkage error of ~1 nm. Three click sites of $\gamma 2$ and $\gamma 8$ were characterized showing good signal to noise in mammalian HEK293T and hippocampal primary neurons (Figure 14 and 15). Since transfection of neurons is a challenging task and in many cases leads to cellular stress in primary neurons, the click approach applying transfection of two plasmids was a non-trivial experiment. Especially the expression of TARPs for a longer time period resulted in toxicity and neuronal death. To circumvent this issue, the orthogonal tRNA^{Py1}

was transferred into a doxycyclin inducible vector. Primary neurons were transfected early (DIV3-4), as neurons show lower stress levels upon transfection at that time point. Furthermore, the expression of tRNA^{PyI} was induced at the stage of mature neurons (DIV16-18) to successfully express clickable TARPs. Interestingly, $\gamma 8$ TARPs showed a homogenous distribution along the whole neuron, while $\gamma 2$ TARPs were predominantly localized to synaptic areas. *d*STORM imaging and cluster analysis confirmed this accumulation of $\gamma 2$ at synapses on a molecular basis (Figure 18 and 19). This phenomenon was already demonstrated by the total amount of localizations per area (localization density) as well. The amount of localizations in synapses was higher for $\gamma 2$ compared to $\gamma 8$ and vice versa in extrasynaptic regions (lower amounts for $\gamma 2$ compared to $\gamma 8$). As hypothesized, $\gamma 2$ clusters in synapses exhibited more localizations per cluster and larger cluster areas compared to other labeling techniques. These results underline previous electron microscopy studies that prove predominant localization of $\gamma 2$ TARPs at synapses, while $\gamma 8$ TARPs showed synaptic and extrasynaptic distribution in hippocampal neurons^{313,314}. In the same context, functional findings revealed that $\gamma 2$ enhances synaptic targeting of AMPARs^{112,315}, while $\gamma 8$ regulates extrasynaptic pools of AMPARs and their transport to synapses^{78,313}.

4.3 Visualization of clickable ionotropic GABA-A receptors and Neuroligin 2

4.3.1 Establishment of clickable $\alpha 1$ and $\alpha 2$ GABA-A receptors in mammalian cells

In addition to the work conducted on KARs and TARPs, GABA receptor type A and in particular the subunits $\alpha 1$ and $\alpha 2$ were identified as potential targets for GCE and bioorthogonal labeling. The respective wildtype plasmids were purchased from Addgene (#49168, #49169). In these constructs, the sequence of the fusion protein super-ecliptic phluorin (SEP) is attached in front of the GABA-AR α -subunit cDNA. The SEP fusion protein impeded the GABA-AR expression (data not shown) and hence was removed by introducing a XhoI restriction site with subsequent cutting via XhoI restriction enzymes. All experiments shown in the figures were conducted using GABA-AR plasmids without the SEP sequence. Six click sites (K73TAG, S171TAG, A171TAG, S181 TAG, S201TAG and K274TAG) were introduced into the extracellular part of the $\alpha 1$ -GABA-AR receptor after identifying unstructured regions in the cryo-EM structure of the $\alpha 1\beta 3\gamma 2$ GABA-A receptor (Figure 21, a). Since the crystal structure of the $\alpha 2$ subunit has not been resolved yet, the protein structure was modeled via SWISS

modeling³¹⁶ and identical amino acids as in the $\alpha 1$ subunit were replaced in $\alpha 2$ by amber stop codons (Figure 21, b).

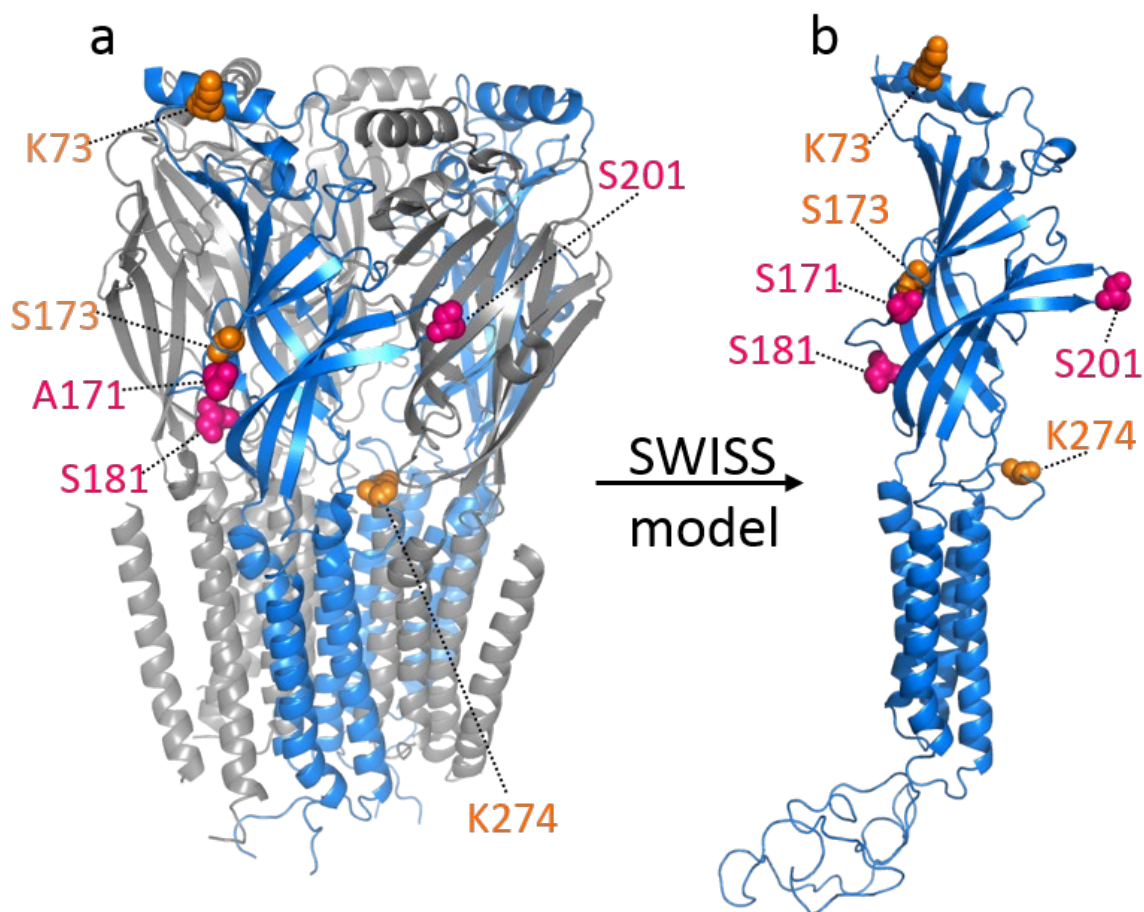


Figure 21 – Click sites at α -subunits of GABA-A receptors. (a) Click positions were identified for $\alpha 1$ -subunits (blue) in unstructured regions at the extracellular part of the $\alpha 1\beta 3\gamma 2$ GABA-A receptor (PDB: 6HUG). (b) Based on the template, the $\alpha 2$ GABA-A receptor was modeled using SWISS modeling³¹⁶ and identical click sites as for $\alpha 1$ were introduced. At the positions S171TAG, S181TAG and S201TAG (magenta) the unnatural amino acid was successfully incorporated, while K73TAG, S173TAG and K274TAG (orange) showed significantly lower fluorescence, when labeled with tetrazine dyes.

The various click mutants were tested for successful incorporation of the unnatural amino acid TCO*-K. To achieve this HEK293T cells were transfected with the respective $\alpha 2$ -click subunits co-transfected with $\beta 1$ and $\gamma 2$ subunit (ratio 2:2:1) and the tRNA^{Pyl}/PylRS plasmid in the presence of TCO*-K. Three click mutants (S171TAG, S181TAG and S201TAG) showed sufficient membrane signal at the CLSM after live labeling with H-Tet-Cy5. The $\alpha 2^{S181}$ showed the strongest fluorescence signal and hence was chosen as the appropriate candidate for further evaluation of clickable GABA-ARs (Figure 22, first panel). The click variant $\alpha 2^{S171}$ showed only weak membrane staining after labeling with H-Tet-Cy5 and the mutants K73TAG,

S173TAG and K274TAG exhibited even lower fluorescence signal (not shown). Additionally, the influence of the co-expressed $\gamma 2$ -subunit on expression of GABA-ARs containing clickable $\alpha 2$ -subunits was investigated. CLSM experiments on HEK293T cells expressing different amounts of $\gamma 2$ subunit (250/500/1000 ng) together with 500 ng $\alpha 2^{S181}$ and 500 ng $\beta 1$ revealed that lower amounts of $\gamma 2$ (250 ng) resulted in significantly stronger fluorescent H-Tet-Cy5 signal of $\alpha 2^{S181}$ compared to high concentrations of $\gamma 2$ (500 ng and 1000 ng). Highest fluorescence was achieved using 250 ng of $\gamma 2$, which was taken as concentration for all further experiments (Figure 22, second panel).

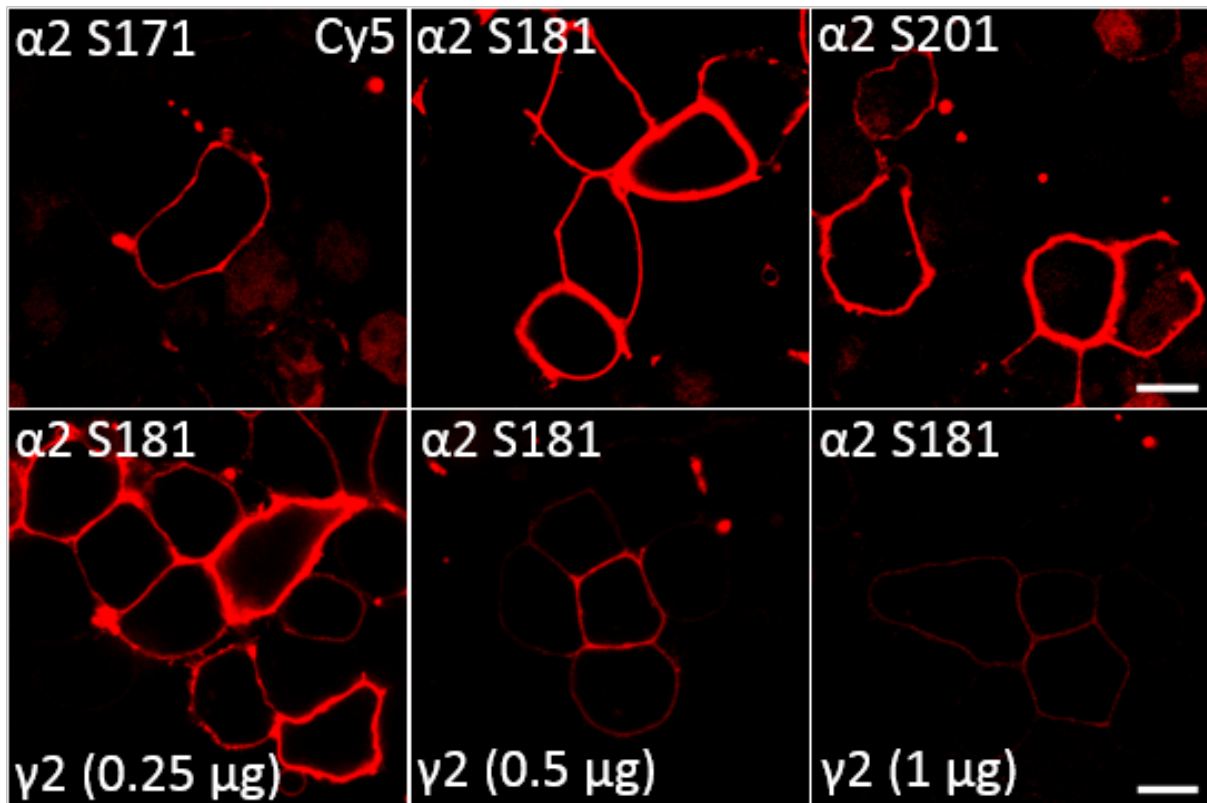


Figure 22 - CLSM imaging of clickable $\alpha 2$ GABA-A receptors at HEK293T surface membrane in dependency of $\gamma 2$ subunit concentration. First panel: Amber stop codons were introduced at positions S171, S181 and S201. HEK293T cells were co-transfected with $\alpha 2$, $\beta 1$, $\gamma 2$ (ratio 2:2:1) and the tRNA^{PyI}/PyIRS plasmid. Live labeling of cells with 1.5 μ M H-Tet-Cy5 was performed for 30 min on ice prior to fixation. $\alpha 2^{S181}$ GABA-ARs showed stronger fluorescence signal in the equatorial membrane compared to $\alpha 2^{S201}$ and $\alpha 2^{S171}$. Second panel: HEK293T cells were transfected with 500 ng $\alpha 2^{S181}$, 500 ng $\beta 1$ and 500 ng tRNA^{PyI}/PyIRS and respective 250/500/1000 ng $\gamma 2$ cDNA and live labeled with H-Tet-Cy5 two days after transfection. Low concentration of $\gamma 2$ (250 ng) resulted in stronger H-Tet-Cy5 signal of $\alpha 2^{S181}$ GABA-ARs compared to high $\gamma 2$ concentrations (500/1000 ng). Scalebar 10 μ m.

The established $\alpha 2^{S181}$ GABA-AR variant was then taken for comparison to anti-HA antibody labeling and control experiments to determine unspecific binding of H-Tet-Cy5. HEK293T cells expressing $\alpha 2^{S181}$ GABA-ARs showed sufficient membrane staining of H-Tet-Cy5 and anti-HA AF488 in the presence of TCO*-K (Figure 23, first panel). Unspecific tetrazine binding

to $\alpha 2^{\text{WT}}$ GABA-ARs could be neglected (Figure 23, third panel). In the absence of TCO*-K, $\alpha 2^{\text{S181}}$ GABA-AR could not be visualized by H-Tet-Cy5 or anti-HA AF488 (Figure 23, second panel). Targeting an endogenous $\alpha 2$ epitope with anti- $\alpha 2$ antibody (Synaptic Systems; 224 103) followed by secondary antibody goat anti-rabbit AF647 showed insufficient binding of $\alpha 2^{\text{S181}}$ GABA-ARs, while tetrazine labeling with H-Tet-Cy3 exhibited homogenous fluorescence signal in HEK293T membranes (Figure 23, fourth panel).

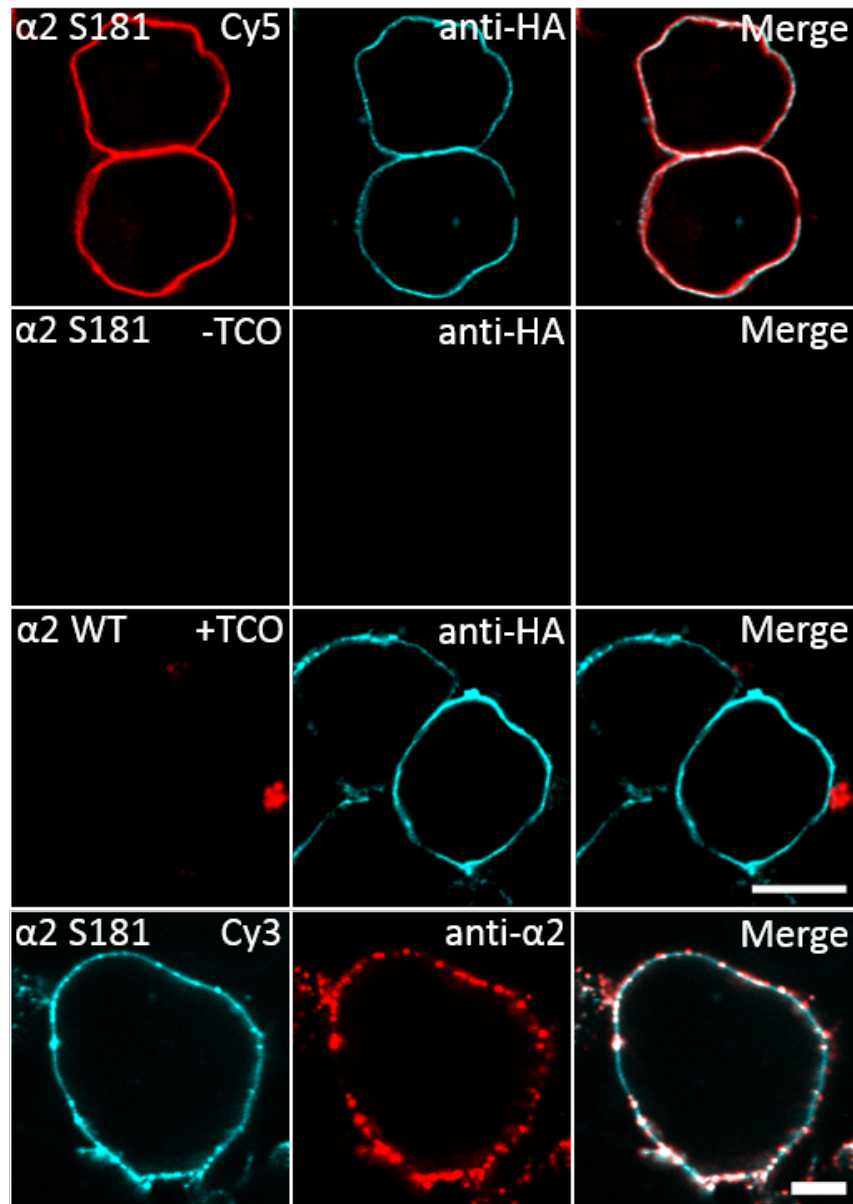


Figure 23 - Specificity of click labeling of $\alpha 2^{\text{S181TAG}}$ GABA-ARs in comparison with antibody labeling. HEK293T cells expressing $\alpha 2^{\text{S181TAG}}$ GABA-ARs (first and second panel) or $\alpha 2^{\text{WT}}$ GABA-ARs (third panel) were live labeled with H-Tet-Cy5 (red) or anti-HA AF488 antibody (cyan) prior to imaging at the CLSM. First panel: Supplied with TCO*-K, clickable GABA-ARs can be visualized in the equatorial membrane by H-Tet-Cy5 as well as anti-HA AF488 antibody. Second panel: Cells lacking the unnatural amino acid TCO*-K showed neither tetrazine nor antibody labeling in the membrane. Third panel: $\alpha 2^{\text{WT}}$ GABA-ARs could be labeled with anti-HA AF488 antibody with barely unspecific binding of H-Tet-Cy5. Scalebar 10 μm . Fourth panel: HEK293T cells expressing clickable $\alpha 2^{\text{S181}}$

GABA-ARs were labeled with 1.5 μM H-Tet-Cy3 (cyan) and 5 $\mu\text{g/ml}$ rabbit anti- $\alpha 2$ antibody (Synaptic Systems; 224 103) for 30 min followed by 5 $\mu\text{g/ml}$ goat anti-rabbit AF647 (red) for another 30 min. Antibody labeling showed spotty signal and insufficient binding to the equatorial membrane, while tetrazine binding visualized a homogenous equatorial membrane corresponding to clicked $\alpha 2^{\text{S181}}$ GABA-A receptors. For the fourth panel, the $\alpha 2$ -subunit gifted by Andrea Barberis was used. Scalebar 5 μm . Adapted with permission from Kuhlemann et al. (under review).

Equivalent experiments were applied for $\alpha 1^{\text{S181}}$ GABA-AR labeled with H-Tet-Cy5 and anti-HA AF555. The overall signal of $\alpha 1^{\text{S181}}$ was lower compared to $\alpha 2^{\text{S181}}$. Nevertheless, the controls showed identical results and $\alpha 1^{\text{S181}}$ GABA-AR could be displayed with both, tetrazine and antibody labeling (data not shown).

Next, tetrazine and antibody labeling were compared on a molecular level using single molecule localization microscopy *d*STORM. $\alpha 2^{\text{S181}}$ GABA-A receptors on basal HEK293T cells were labeled with H-Tet-Cy5 and anti-HA CF568 for 60 min on ice and fixed with 4% formaldehyde and 0.25% glutaraldehyde. Both labeling methods revealed an efficient labeling of $\alpha 2^{\text{S181}}$ GABA-A receptors in a homogenous distribution at the cell membrane (Figure 24, left). To quantify the amount of receptors present on the basal membrane, DBSCAN analysis was performed on the localization data and showed higher amounts of localization clusters for H-Tet-Cy5 labeled $\alpha 2^{\text{S181}}$ GABA-A receptors (29.2 ± 2.1 cluster/ μm^2) compared to anti-HA CF568 labeled receptors (21.7 ± 2.8 cluster/ μm^2) (Figure 24, right).

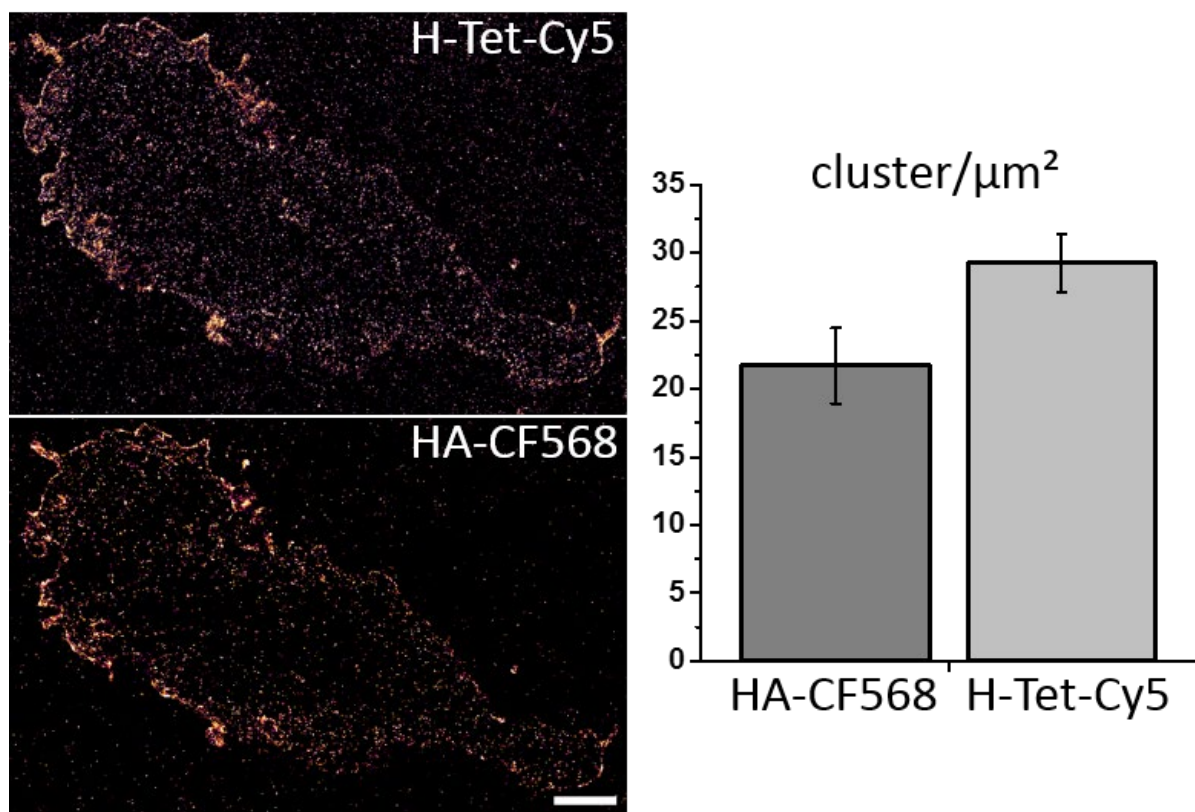


Figure 24 - *d*STORM imaging and analysis of $\alpha 2^{\text{S181}}$ GABA-A receptors. Left: Basal membranes of HEK293T cells expressing clickable $\alpha 2^{\text{S181}}$ GABA-A receptors labeled with H-Tet-Cy5 (top) and anti-HA CF568 (bottom). Receptors show homogenous distribution on the basal membrane. Scalebar 2 μm . Right: DBSCAN analysis of localization data with parameters set: epsilon = 20 nm and minPoints = 3 and respective data showing cluster/ μm^2 . Higher amounts of cluster/ μm^2 for H-Tet-Cy5 compared to HA-CF568 were confirmed in 17 independent experiments. Adapted with permission from Kuhlemann et al. (under review).

4.3.2 Functional analysis of clickable $\alpha 2^{\text{S181TAG}}$ GABA-A receptors

The studies above demonstrate the application of GCE and bioorthogonal labeling of GABA-A receptors in CLSM and *d*STORM imaging. However, the overall functionality of the modified receptor carrying an unnatural amino acid remained to be confirmed. To test the physiological behavior of modified receptors, the electrophysiological properties as well as the diffusion behavior of the clickable receptor ($\alpha 2^{\text{S181}}$ GABA-AR) were compared to the wildtype receptor ($\alpha 2^{\text{WT}}$ GABA-AR). In close collaboration with Dieter Janzen (Institute of Clinical Neurobiology, Wuerzburg), patch-clamp recordings were performed on HEK293T cells expressing pentameric $\alpha 2\beta 1\gamma 2$ GABA-A receptors comprising either the clickable $\alpha 2^{\text{S181}}$ or the $\alpha 2^{\text{WT}}$ subunit (Figure 25, a and b). Current amplitudes of GABA-ARs in the presence of 30 μM GABA were similar for clicked and wildtype receptors. Addition of 30 μM ZnCl_2 and subsequent binding of divalent Zn^{2+} cations to GABA-AR sites induced slightly lower amplitudes. Supplying 100 μM of the GABA-AR ligand picrotoxin resulted in significantly

blocked currents through binding of picrotoxin close to the GABA-AR chloride channel (Figure 25, a). The normalized I-V-curves showed also similar values for click mutant and wildtype GABA-ARs (Figure 25, b). In cooperation with Dr. Christian Werner, FRAP experiments were conducted on $\alpha 2^{S181}$ and $\alpha 2^{WT}$ GABA-ARs on HEK293T cells labeled with anti-HA AF488 (Figure 25, c and d). After photobleaching of a region of interest at the membrane surface, the relative fluorescence in the GCE modified- and wildtype receptor recovers equally (Figure 25, c). Furthermore, the recovery time necessary to reach half of the recovered fluorescence (tau) shows similar values for $\alpha 2^{S181}$ (19.51 ± 6.78 s) and $\alpha 2^{WT}$ GABA-ARs (19.50 ± 4.38 s) indicating identical diffusion behavior of both variants.

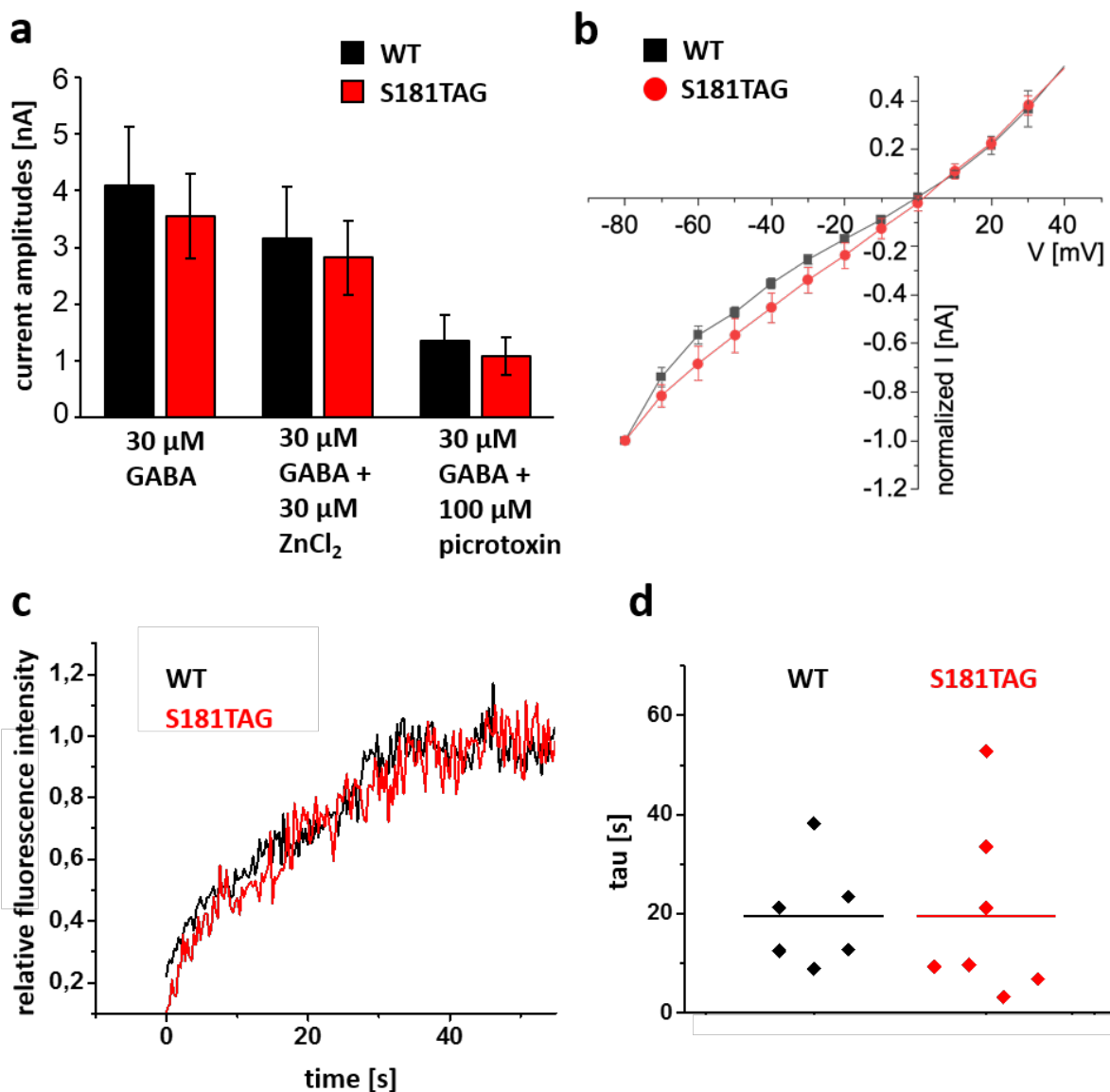


Figure 25 - Functionality analysis of clickable $\alpha 2^{S181}$ and $\alpha 2^{WT}$ GABA-ARs. (a) Patch-clamp recordings of pentameric $\alpha 2\beta 1\gamma 2$ GABA-ARs in the presence of 30 μ M GABA, 30 μ M ZnCl₂ or 100 μ M picrotoxin. Clickable $\alpha 2^{S181}$ GABA-ARs show similar current amplitudes compared to $\alpha 2^{WT}$. Presence of divalent Zn²⁺ cations reduce current amplitudes slightly, while supplying 100 μ M picrotoxin blocks

GABA-AR currents significantly. (b) Normalized I-V-currents of GABA-AR WT or click mutant. (c) FRAP experiments of HEK293T cells expressing $\alpha 2^{S181}$ or $\alpha 2^{WT}$ labeled with anti-HA AF488. Both constructs display similar relative fluorescence intensity over time. (d) Tau values of respective FRAP measurements for $\alpha 2^{S181}$ and $\alpha 2^{WT}$. The tau value equals the time required to reach 50% of the recovered fluorescence. Adapted with permission from Kuhlemann et al. (under review).

4.3.3 Visualizing clickable $\alpha 2^{S181TAG}$ GABA-A receptors in neurons

First validation experiments in mammalian cells as well as the functionality analysis formed the basis for using clickable $\alpha 2^{S181TAG}$ GABA-A receptors in a neurobiological context. In close collaboration with Enrica Petrini, Andrea Barberis and Martina Bruno, hippocampal primary neurons were transfected at DIV14 with $\alpha 2^{S181TAG}$ GABA-AR subunits together with the respective tRNA^{Pyl}/PylRS plasmid and eGFP in the presence of unnatural amino acid TCO*-K. At DIV16, postsynaptic $\alpha 2^{S181TAG}$ GABA-AR was labeled with Pyr-Tet-ATTO643 and presynaptic vesicular GABA transporter (vGAT) was labeled with anti-vGAT antibody and subsequently stained with secondary antibody goat anti-mouse AF568. Positively transfected neurons were identified by eGFP signal. Pyr-Tet-ATTO643 signal was juxtaposed to presynaptic vGAT fluorescence indicating successful incorporation at synapse and efficient labeling of clickable GABA-A receptors in hippocampal primary neurons (Figure 26).

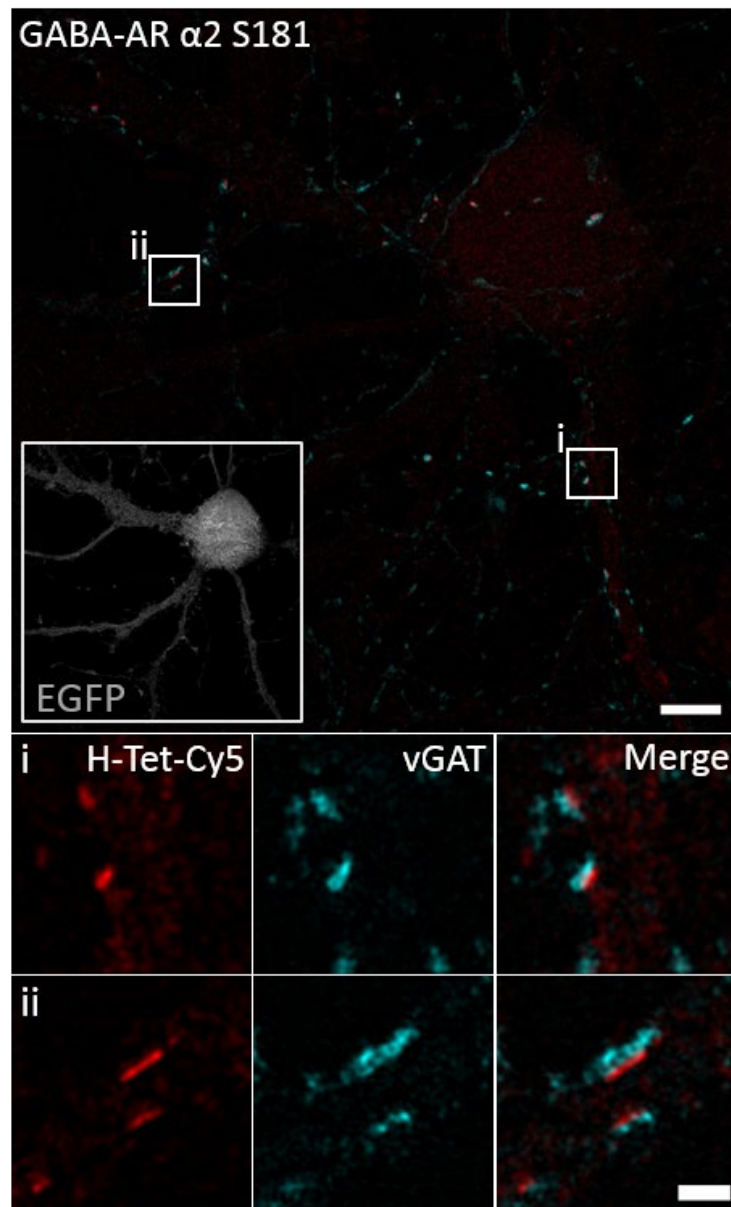


Figure 26 - Bioorthogonal labeling of $\alpha 2^{S181}$ GABA-ARs in hippocampal primary neurons (DIV16). Neurons expressing clickable $\alpha 2^{S181}$ GABA-ARs were labeled with Pyr-Tet-ATTO643 (red) and anti-vGAT antibody and secondary antibody goat anti-mouse AF568 (cyan). eGFP coexpression confirms successful transfection of the respective neuron. (i, ii) Magnified insets display postsynaptic clickable GABA-ARs (red) juxtaposed to presynaptic GABA transporter vesicles (cyan). Scalebar: top 5 μm ; insets 1 μm . Image acquired by Dr. Christian Werner. Adapted with permission from Kuhlemann et al. (under review).

4.3.4 GCE and bioorthogonal labeling of NL2

Additionally, the click system was implemented to Neuroligin 2 (NL2), an interaction partner of GABA-A receptors in inhibitory synapses. Suitable click sites were identified in unstructured regions in the extracellular domain of NL2 at the positions E61TAG, A113TAG and Q227TAG (Figure 27, left). Best fluorescence signal was obtained from the NL2^{A113TAG} click variant in HEK293T cells labeled with H-Tet-Cy5 and anti-HA AF555 (Figure 27, first panel). In the

absence of TCO*-K neither tetrazine nor antibody signal was detected (Figure 27, second panel). Even in the presence of TCO*-K, NL2^{WT} showed only antibody signal (Figure 27, third panel).

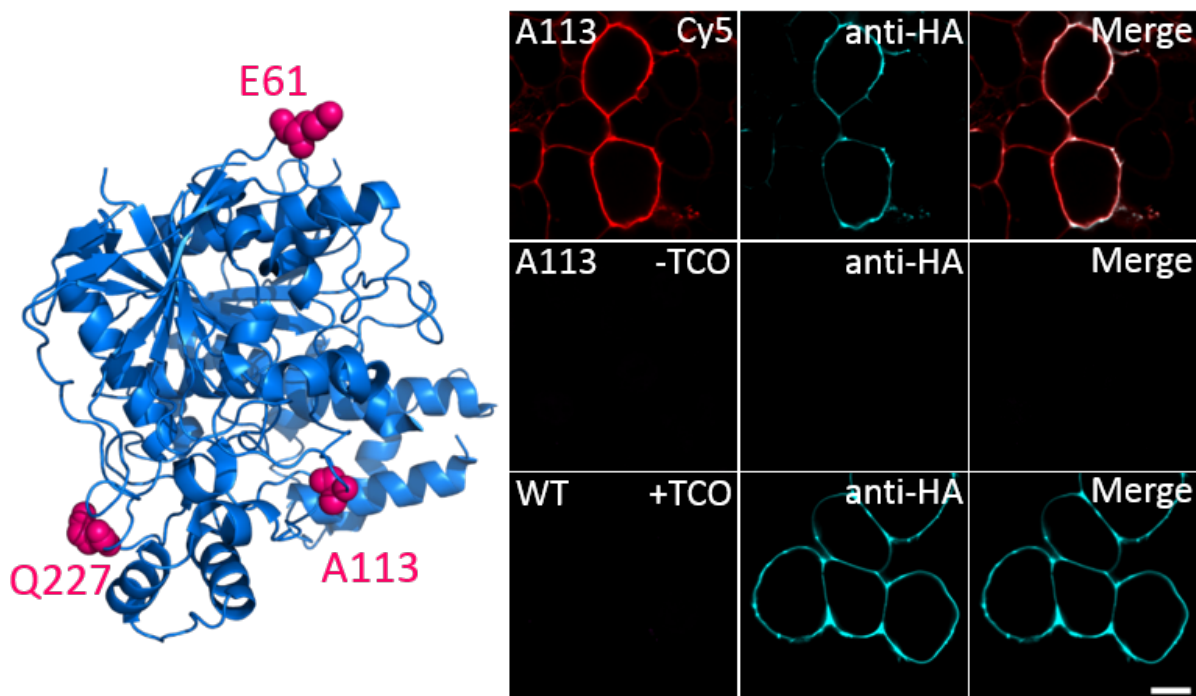


Figure 27 – Click sites of NL2 and specificity of bioorthogonal labeling. Left: Amber stop codons were introduced into the extracellular part of NL2 at positions E61TAG, A113TAG and Q227TAG based on the PDB model 5XEQ. Right: HEK293T cells expressing NL2^{A113} and respective tRNA/tRNA synthetase pair were labeled with H-Tet-Cy5 (red) and anti-HA AF555 (cyan). First panel: In the presence of TCO*-K, HEK293T cells showed sufficient H-Tet-Cy5 and anti-HA AF555 fluorescence of NL2 in the equatorial membrane. Second panel: Absence of TCO*-K resulted in neither tetrazine nor antibody signal. Third panel: NL2^{WT} was treated identical as the clickable NL2 supplied with TCO*-K and exhibited neglectable unspecific binding of H-Tet-Cy5, but clear anti-HA AF555 fluorescence along the membrane. Scalebar 10 μ m.

4.3.5 Discussion on clickable GABA-A receptors and NL2

In this chapter, clickable variants of GABA-AR $\alpha 1$ and $\alpha 2$ subunits and NL2, a transsynaptic organizer of inhibitory synapses, were established in mammalian cells. The best click mutants of GABA-A receptors were identified and the coexpression of the necessary subunits $\beta 1$ and $\gamma 2$ was optimized using fluorescence microscopy such as CLSM. Since expression was performed with three subunits ($\alpha\beta\gamma$) and the tRNA^{Pyl}/PylRS, several concentrations especially for the $\gamma 2$ subunit (250 ng) and expression times (2 days) needed optimization. Additionally, the advantage of click chemistry labeling of GCE modified GABA-A receptors could be visualized utilizing *d*STORM imaging at narrow compartments like the basal membrane close to the coverslip. Comparison of H-Tet-Cy5 labeled receptors with anti-HA-CF568 targeted GABA-

ARs on the same cells revealed higher density of receptors per area for click labeled GABA-A receptors (Figure 23). This indicates, that antibody binding can be influenced by the size of the antibody itself and might fail to recognize all surface-exposed epitopes due to steric hinderance. In this case, the small size of tetrazine-dyes may be beneficial to ensure more efficient binding to the target protein. However, antibody binding using anti-HA antibodies can also be applied on HEK293T cells expressing the GABA-AR wildtype and hence could lead to higher amounts of clusters even compared to the clicked GABA-ARs. This might originate from the better expression of the wildtype compared to the click variant (see HA-signal, Figure 23), since the incorporation of an unnatural amino acid competes with the release factor 1 and is not as efficient as a canonical amino acid. Furthermore, antibodies targeting endogenous epitopes of GABA-A receptor would be a straightforward approach to circumvent artificial overexpression. However, only a limited number of antibodies targeting the extracellular domain of GABA-A receptors are available and one commercial antibody tested here showed inhomogenous and spotty binding to GABA-A receptors (Figure 23). Currently, imaging of GABA-A receptors relies on these immunolabeling antibodies either targeting endogenous level of GABA-A receptors or overexpressed GABA-ARs carrying small genetic tags such as hemagglutinin (HA)^{317,318}. Besides the limited availability of antibodies targeting endogenous epitopes, there are further drawbacks associated with the usage of antibodies: crosslinking and internalization effects induced by antibodies and the influence of their size (~10 nm) on the diffusion behavior of receptors^{319,320}. Especially in crowded compartments such as the synaptic cleft, the size of antibodies coupled to quantum dots causes steric hinderance when extrasynaptic receptors try to reach synaptic areas⁵³. Hence, establishing an alternative smaller label for GABA-A receptors, such as bioorthogonal labeling of unnatural amino acids with tetrazine dyes will reduce the listed issues. In this context, it needs to be highlighted, that the introduction of an unnatural amino acid did not lead to perturbation of channel properties or diffusion of the receptor. This has been validated by electrophysiological studies as well as FRAP experiments. The optimal $\gamma 2$ subunit concentration was verified to be 250 ng $\gamma 2$ plasmid (Figure 22) while all other plasmids were used with 500 ng per plasmid. Since GABA-A receptors can form functional $\alpha 2\beta 2$ receptors without $\gamma 2$ ³²¹, $\gamma 2$ subunit expression needed to be proven. The electrophysiological data correspond to a functional $\alpha 2\beta 1\gamma 2$ GABA-A receptor. Current amplitudes were slightly reduced in the presence of Zn^{2+} ions indicating $\gamma 2$ existence. Full blocking occurred through the inhibitor picrotoxin (Figure 25)^{322,323}. Positively transfected cells were identified by anti-HA AF488 labeling. Since cells lacking the unnatural amino acid TCO*-K showed neither click- nor HA-signal (Figure 23) these identified cells also corresponded to

cells with an incorporated unnatural amino acid. However, it would be interesting to investigate clickable GABA-AR currents bound to tetrazine-dyes solely because the antibody binding might already influence the electrophysiological behavior of the GABA-A receptor wildtype and click mutant. Unfortunately, within the scope of this dissertation these studies could not be performed. The reason for this were the limited imaging capabilities at the electrophysiological setup, which required a strong fluorescence signal obtained from multiple fluorophores coupled to the HA-antibody. Interestingly, the FRAP experiments confirmed similar diffusional behavior of wildtype and clickable GABA-A receptors. For comparability, both variants were labeled with anti-HA AF488 antibodies but again, the antibody binding itself might interfere with the natural diffusion of the receptors. Hence, receptors only clicked with tetrazine-dyes should be taken in consideration to analyze native receptor diffusion. Characterization of clickable GABA-A receptors in mammalian cells allow fast establishment of click sites and subsequent analysis of functionality. Nevertheless, GABA-A receptors need to be studied in a neuronal context to understand their role in synaptic inhibition and plasticity. GCE and bioorthogonal labeling were already applied to tackle challenging neuronal questions. For instance, clickable PIRK potassium channels could be controlled in hippocampal neurons and in mouse neocortex in vivo through photoreleasable unnatural amino acids³²⁴. Additionally, the tRNA^{Pyl}/PylRS pair was utilized to transfect and express clickable GFP in brain slices and living mice⁷⁶. However, applying amber suppression technique to target synaptic receptors with super-resolution microscopy remained to be demonstrated. Due to this, GABA-ARs were selected as targets for successful expression of clickable variants in hippocampal neuronal cells with subsequent super-resolution microscopy (Figure 26). Transfection of hippocampal primary neurons is a challenging task since neurons are not as robust as standardized cell lines and the transfection of plasmids reduces the viability of the neurons significantly. In this context, the click approach requires the clickable $\alpha 2^{S181}$ GABA-AR plasmid and a second plasmid carrying the tRNA^{Pyl}/PylRS which increases the stress for neuronal cells. However, clickable $\alpha 2^{S181}$ GABA-ARs could be expressed at low transfection efficiency on DIV14 neurons. Tetrazine labeling of clickable GABA-ARs visualized the receptors at postsynapses juxtaposed to presynaptic vGAT signal. Interestingly, the receptors showed only diffuse signal along the dendrite and strong signal at the synapses, which might speak for a predominantly localization at synapses. GABA-A receptors interact with multiple interaction partners in the synaptic cleft. As mentioned in the theoretical background, the most important partners are gephyrin, collybistin and neuroligins. A clickable version of NL2 was created to allow investigation of

GABA-AR-NL2 interaction in the future. The click variant NL2^{A113} showed sufficient expression in HEK293T cells and could be labeled efficiently with H-Tet-Cy5 (Figure 27).

4.4 Visualizing clickable dimeric receptors

The previous chapter demonstrated that GCE in combination with click chemistry can be advantageous for labeling hard-to-target proteins instead of using conventional antibody approaches. In the following it was investigated whether the small size of the tetrazine label can additionally be beneficial for studying multimeric receptor structures in the context of super-resolution fluorescence imaging.

4.4.1 Application of click chemistry to reveal receptor composition

The binding efficiency of tetrazine functionalized dyes to TCO*-K modified neuronal receptors was evaluated in a control experiment in mammalian cells. The functional $\alpha 2\beta 1\gamma 2$ GABA-AR pentamer comprises two $\alpha 2$, two $\beta 1$, and one $\gamma 2$ subunits. The two clickable $\alpha 2$ subunits ($\alpha 2^{\text{S181}}$ GABA-AR) can be treated as a dimeric receptor. In this context, click sites were introduced in the $\gamma 2$ subunit at the positions L198 and S217 to obtain a monomeric receptor for comparison with the dimeric $\alpha 2$ subunits (Figure 28).

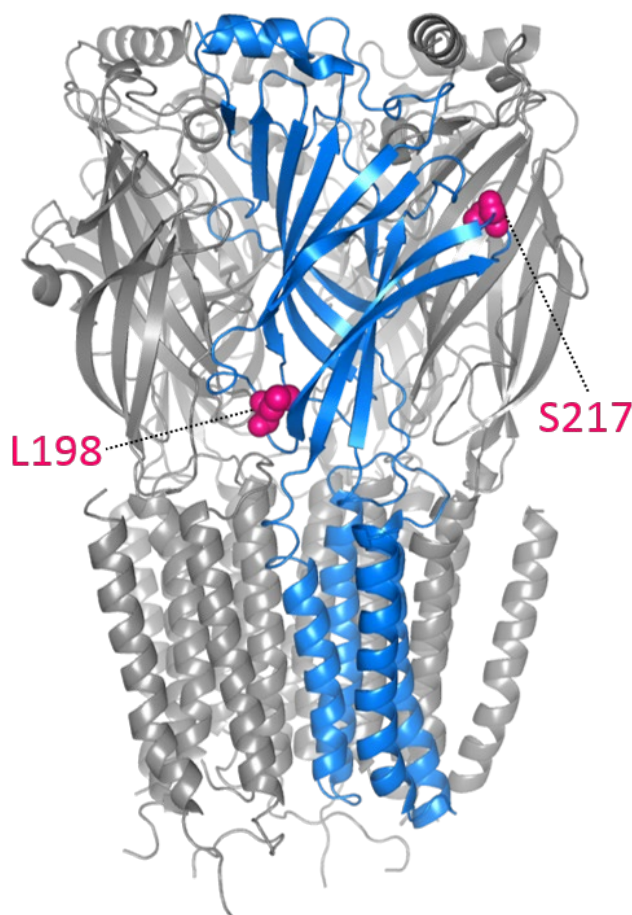


Figure 28 - Click sites at GABA-AR $\gamma 2$ subunit (blue) of pentameric $\alpha 2\beta 1\gamma 2$ GABA-AR (grey). The pentameric $\alpha 2\beta 1\gamma 2$ GABA-AR comprises one $\gamma 2$, one $\beta 1$ and two $\alpha 2$ subunits. Amber stop codons were introduced by site-directed mutagenesis into the extracellular domain of the $\gamma 2$ subunit at positions L198TAG and S217TAG. Click sites were chosen at positions similar to established $\alpha 1$ and $\alpha 2$ clickable variants. PDB-ID: 6HUG.

Next, the required tetrazine dye concentration to saturate all surface exposed GABA-A receptors expressed on HEK293T cell membranes was determined. HEK293T cells were transfected with clickable versions of either $\alpha 2^{S181}$ or $\gamma 2^{L198}$ co-transfected with the necessary GABA-AR subunits together with the tRNA^{Pyl}/PylRS. After 48 hours of expression, clickable receptors were labeled with 1.5 μM , 3 μM or 6 μM H-Tet-Cy5 for 60 min on ice followed by labeling with 1.5 μM H-Tet-Cy3 for another 30 min on ice. Labeled cells were imaged at the CLSM for evaluating signal intensity (Figure 29). Cy3 signal could only be detected at cells pre-labeled with 1.5 μM H-Tet-Cy5 (Figure 29, left), while 3 μM and 6 μM H-Tet-Cy5 enabled saturation of surface exposed clickable GABA-A receptors. Since saturation could be achieved with 3 μM H-Tet-Cy5, all following experiments used 3 μM as standard tetrazine concentration.

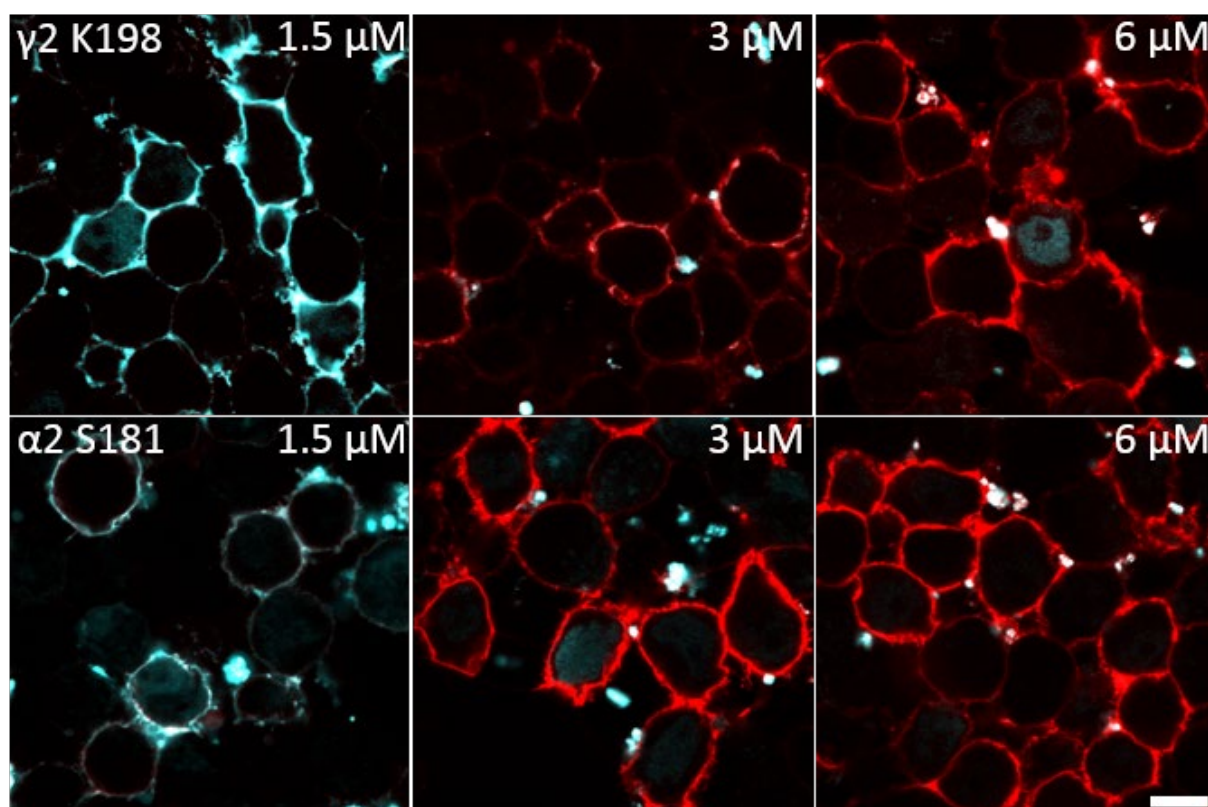


Figure 29 – Saturation experiment for evaluation of required tetrazine-dye concentration. HEK293T cells expressing clickable $\gamma 2^{L198}$ (a) or $\alpha 2^{S181}$ (b) GABA-A receptors ($\alpha 2\beta 1\gamma 2$) together with tRNA^{Pyl}/PylRS were labeled with 1.5 μM (left), 3 μM (middle) or 6 μM H-Tet-Cy5 (red) for 60 min on ice following by 1.5 μM H-Tet-Cy3 (cyan) for 30 min on ice. Images show merged fluorescence channels of H-Tet-Cy5 and H-Tet-Cy3. When pre-labeling with 1.5 μM H-Tet-Cy5 some cells still showed strong H-Tet-Cy3 signal after post-labeling with H-Tet-Cy3 (left). Concentrations of at least

3 μM H-Tet-Cy5 (middle and right) saturated all incorporated TCO*-K amino acids, so that nearly no H-Tet-Cy3 signal could be detected after post-labeling with H-Tet-Cy3. Scalebar: 10 μm .

In the following experiments, binding of tetrazine functionalized fluorophore to the dimeric $\alpha 2^{\text{S181}}$ or monomeric $\gamma 2^{\text{L198}}$ GABA-A receptors was investigated further. To obtain an increased signal of the FRET-donor, the acceptor fluorophore was bleached in this FRET approach. Again, HEK293T cells expressing either clickable $\alpha 2^{\text{S181}}$ or $\gamma 2^{\text{L198}}$ GABA-A receptors were labeled with H-Tet-Cy3 (donor) or H-Tet-Cy5 (acceptor) in equal amounts (1.5 μM each) for 60 min on ice and then live imaged (Figure 30, a). A region of interest was selected at the equatorial membrane and analyzed over the whole FRET image series (60 frames). The intensity in the first 20 frames was averaged and set as fluorescence baseline. Bleaching of H-Tet-Cy5 resulted in an intensity increase of H-Tet-Cy3 labeled $\alpha 2^{\text{S181}}$ GABA-A receptors by a factor of ~ 1.4 (Figure 30, b, red). H-Tet-Cy3 signal of clickable $\gamma 2^{\text{L198}}$ GABA-ARs showed no increase of intensity after bleaching of the H-Tet-Cy5 acceptor (Figure 30, blue).

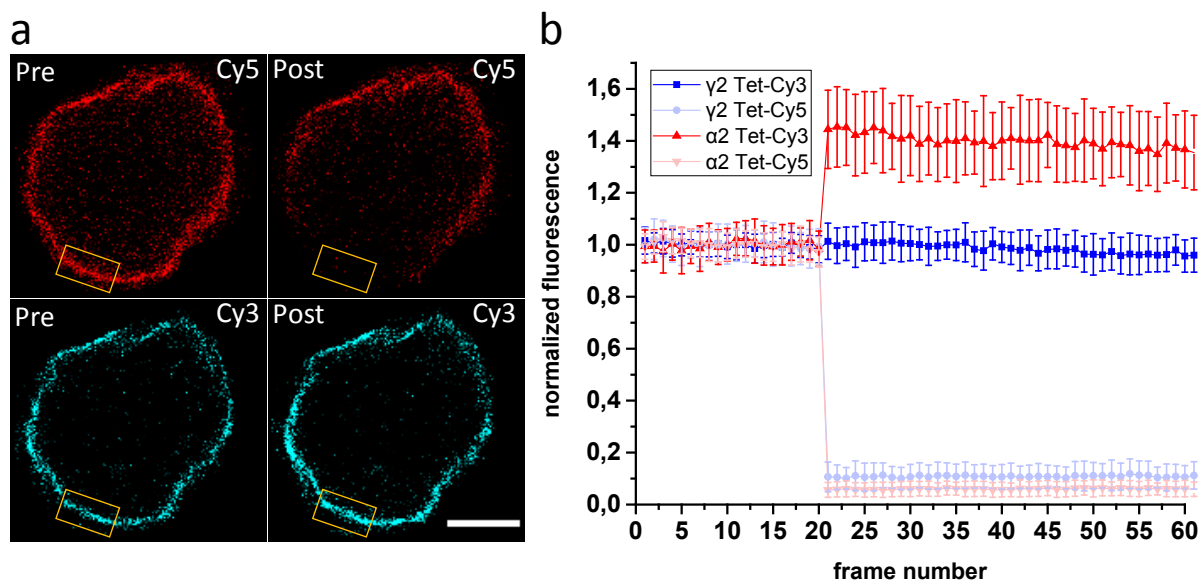


Figure 30 – FRET imaging of clickable $\alpha 2^{\text{S181}}$ and $\gamma 2^{\text{L198}}$ GABA-A receptors based on the principle of acceptor bleaching. (a) Display of FRET procedure: HEK293T cells expressing $\alpha 2^{\text{S181}}$ GABA-ARs were labeled with equal amounts of H-Tet-Cy3 (cyan; 1.5 μM) and H-Tet-Cy5 (red; 1.5 μM) for 60 min on ice and then live imaged at the CLSM. Left images represent Cy5 and Cy3 signal - pre-bleaching - in the equatorial membrane in frame number one. Right images display Cy5 and Cy3 signal directly post-bleaching of the FRET-acceptor H-Tet-Cy5 at frame number 21. Tagged area was selected for bleaching and FRET analysis. Scalebar: 5 μm . (b) Analysis of fluorescence intensity of H-Tet-Cy5 (light) and H-Tet-Cy3 (dark) during FRAP experiment. Intensity was normalized to the mean value of the first 20 frames (pre-bleach). Cy5 intensities drop dramatically after bleaching post frame 20. Cy3 intensity of $\gamma 2^{\text{L198}}$ is unaffected by bleaching, while Cy3 labeled $\alpha 2^{\text{S181}}$ show a significant increase in normalized fluorescence ($n = 40$).

4.4.2 Single molecule localization microscopy *d*STORM

The previous experiments confirmed that all clickable GABA-A receptors can be targeted with 3 μM tetrazine functionalized fluorophores (Figure 29). Additionally, more than one GABA-AR $\alpha 2$ subunit in the $\alpha 2\beta 1\gamma 2$ pentamer can be targeted with tetrazines (Figure 30). As a next step the dimeric character of clickable $\alpha 2^{\text{S181}}$ GABA-A receptors was examined in *d*STORM experiments and cluster analysis (Figure 31). DBSCAN algorithm was applied for determination of clustered $\alpha 2^{\text{S181}}$ GABA-AR localizations for varying concentrations (50 nM to 6 μM) of H-Tet-Cy5. Probability distributions showed no differences in localization per clusters independent of the tetrazine dye concentration (Figure 31, a). Next, the localizations per cluster were compared between dimeric $\alpha 2^{\text{S181}}$ GABA-A receptors (red) and monomeric $\gamma 2^{\text{L198}}$ receptors (blue) (Figure 31, b). 3 μM H-Tet-Cy5 (light) were used to label HEK293T cells expressing the respective click variant and both approaches showed similar localizations per cluster on clickable GABA-A receptors at the basal membrane. As an additional experiment, clickable GABA-ARs were labeled with 3 μM H-Tet-Digoxigenin and subsequently targeted with anti-Digoxigenin-AF647 (dark). However, this procedure resulted in similar distributions of localizations per cluster for monomeric (blue) and dimeric GABA-ARs (red). Finally, these experiments were compared to labeling of $\alpha 2^{\text{S181}}$ GABA-ARs with 10 $\mu\text{g/ml}$ anti-HA AF647 (grey). Overall, the approaches exhibited similar cluster properties based on the localizations per cluster calculated for one GABA-A receptor.

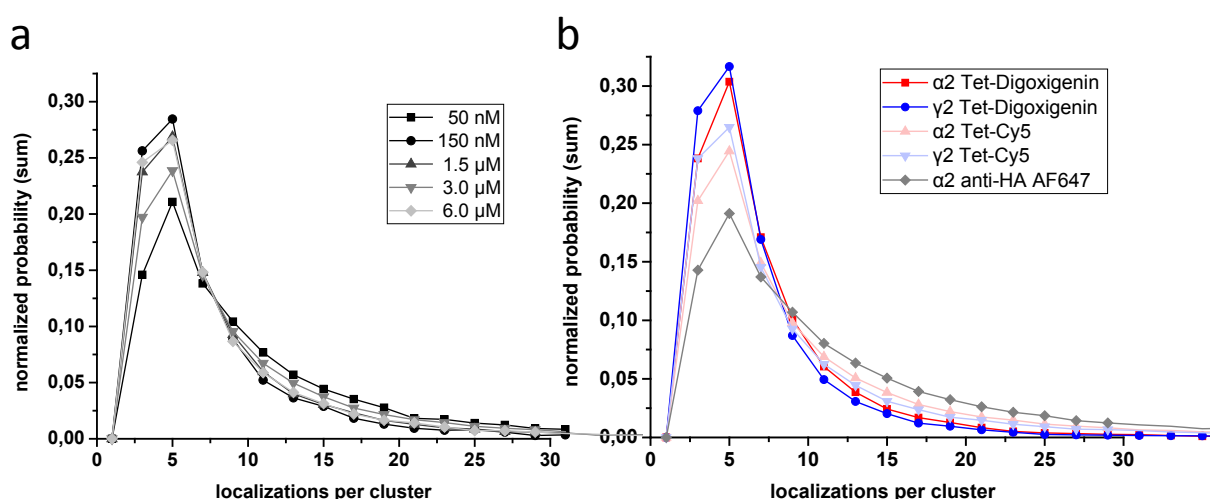


Figure 31 – DBSCAN cluster analysis of *d*STORM localization data of clickable GABA-A $\alpha 2^{\text{S181}}$ and $\gamma 2^{\text{L198}}$ receptors. (a) Determination of localizations per cluster of clickable $\alpha 2^{\text{S181}}$ GABA-A receptors expressed on HEK293T cells labeled with varying concentrations of H-Tet-Cy5 (50 nM, 150 nM, 1.5 μM , 3.0 μM and 6.0 μM) for 60 min on ice. Probability was normalized by the sum of all clusters. (b) Localizations per cluster of clickable $\alpha 2^{\text{S181}}$ (red and grey) and $\gamma 2^{\text{L198}}$ GABA-ARs (blue) labeled either with 3 μM H-Tet-Digoxigenin followed by 5 $\mu\text{g/ml}$ anti-Digoxigenin-AF647 (dark) or 3 μM H-Tet-Cy5 (light) or 10 $\mu\text{g/ml}$ anti-HA AF647 (grey) with each step conducted for 60 min on ice. For *d*STORM images over 15000 frames were acquired with 15 ms exposure time. Each experiment was conducted at least $n = 7$ times.

4.4.3 Click chemistry combined with expansion microscopy

Intriguingly, *d*STORM experiments could not resolve differences between monomeric and dimeric receptors (Figure, 27). As an alternate approach providing better separation of single epitopes click chemistry was combined with expansion microscopy to visualize monomeric and dimeric receptors. In this process, two labeling strategies were tested. In a first approach, HEK293T cells expressing either $\gamma 2^{L198}$ or $\alpha 2^{S181}$ GABA-A receptors were labeled with 3 μ M Pyr-Tet-ATTO643 followed by fixation and crosslinking with AcX. ATTO-643 labeled receptors could be detected at the CLSM directly after the digestion in a 2-fold expanded polyacrylamide gel (Figure 32, left). The signal of $\gamma 2^{L198}$ was weaker compared to $\alpha 2^{S181}$ and barely no fluorescence signal could be found for both clickable receptors in fully expanded gels (factor ~ 8). In parallel, the second approach exploited labeling with 3 μ M H-Tet-Digoxigenin followed by anti-Digoxigenin-CF568 (5 μ g/ml). Again, fluorescence signal of $\alpha 2^{S181}$ receptors was higher compared to $\gamma 2^{L198}$ in 2-fold and in 8-fold expanded hydrogels (Figure 32, middle and right). In the future, 8-fold expanded gels containing clickable GABA-ARs will be investigated with super-resolution microscopy using structured illumination microscopy (SIM).

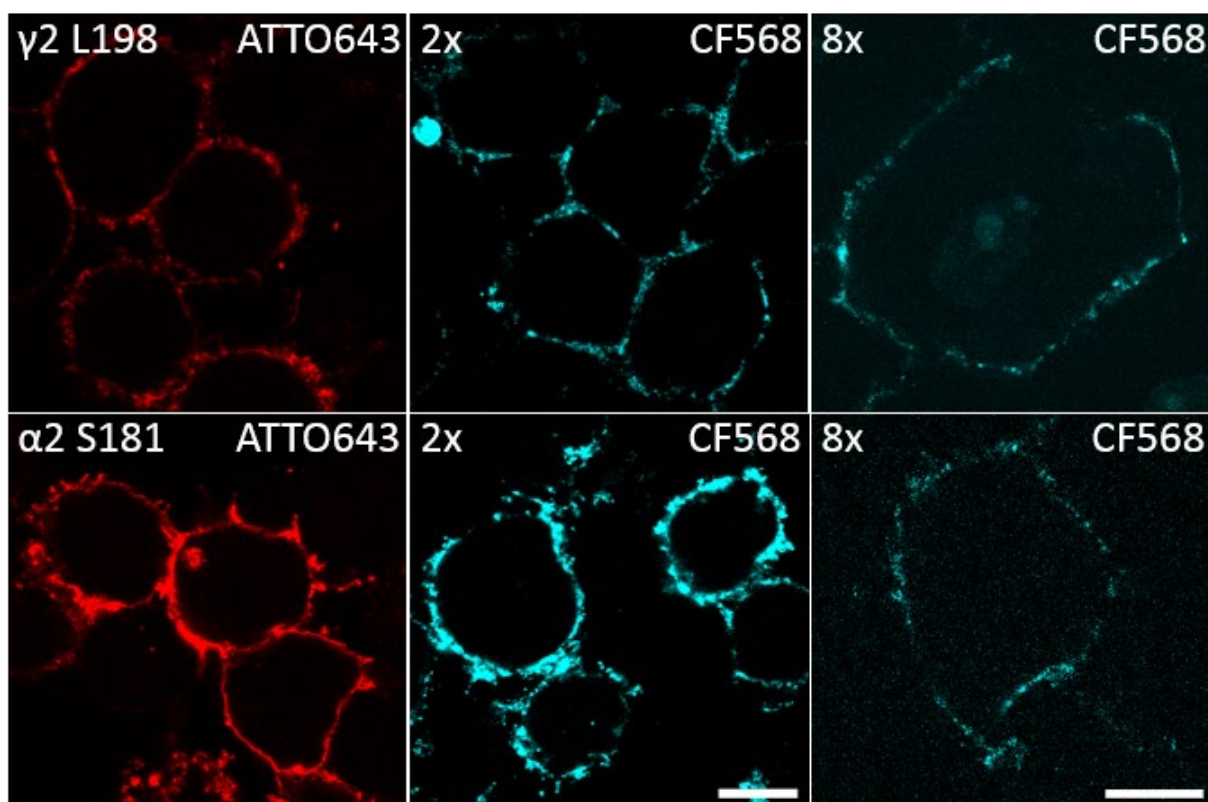


Figure 32 – CLSM imaging of clickable $\gamma 2^{L198}$ and $\alpha 2^{S181}$ GABA-A receptors labeled with Pyr-Tet-ATTO643 or anti-Digoxigenin-CF568. HEK293T cells expressing $\gamma 2^{L198}$ or $\alpha 2^{S181}$ GABA-ARs were labeled either with 3 μ M Pyr-Tet-ATTO643 (red) or 3 μ M H-Tet-Digoxigenin and 5 μ g/ml anti-Digoxigenin-CF568 (cyan) prior to fixation and crosslinking with AcX. The positional information was transferred into a hydrogel and protein crosslinks were digested with Proteinase K. Immediately after digestion, labeling efficiency was evaluated at the CLSM with a 2-fold expanded hydrogel (left and

middle). The fluorescence intensity of $\alpha 2^{S181}$ GABA-A receptors was higher compared to $\gamma 2^{L198}$ receptors. Only anti-Digoxigenin-CF568 could be detected in fully expanded gels and with decreased fluorescence signal (right) compared to 2-fold expanded gels. Expansion factor was determined via physical size of the hydrogel and cell diameter based on the equatorial fluorescence signal of HEK293T cells. Scalebar: 2x, 20 μm ; 8x, 50 μm .

4.4.4 Discussion on visualization of monomeric and dimeric receptors

Visualization of multimeric proteins with fluorescence microscopy requires addressing every single subunit of a multimeric receptor. Application of antibodies might lead to steric hinderance and thus, to reduced labeling efficiency of epitopes positioned in close proximity to each other. To circumvent this accessibility issue and to investigate dimeric and monomeric subunits of the GABA-A receptor, characterization of the clickable variants of GABA-A $\alpha 2^{S181}$ and $\gamma 2^{L198}$ using CLSM, FRET, *d*STORM and click-ExM was performed. First, saturation experiments were conducted with two tetrazine dyes (H-Tet-Cy5 and H-Tet-Cy3). Subsequent labeling with H-Tet-Cy3 showed saturation of all surface-exposed GABA-A $\alpha 2$ and $\gamma 2$ receptors at 3 μM tetrazine concentration (Figure 29). However, this experiment rather confirmed that all accessible TCO*-K modified GABA-A receptors were addressed than proving that both clickable $\alpha 2$ subunits within one receptor could be labeled. Consequently, intra- and intermolecular FRET experiments of tetrazine labeled GABA-A receptors were conducted to test whether one or two tetrazine functionalized fluorophores can bind to the two $\alpha 2$ subunits in the pentameric receptors. FRET signal could be observed between H-Tet-Cy3 and H-Tet-Cy5 at the equatorial membrane of GABA-ARs expressing HEK293T cells. $\alpha 2^{S181}$ GABA-ARs showed an ~ 1.4 increase of H-Tet-Cy3 signal post acceptor bleaching, whereas H-Tet-Cy3 fluorescence of $\gamma 2^{L198}$ GABA-ARs remained on the pre-bleached intensity. The $\gamma 2^{L198}$ control represents a monomeric receptor and could only show FRET, when two monomeric receptors were in close FRET distance. Since we were working under overexpressed conditions of GABA-A receptors, this effect called inter-molecular FRET is probalistic. However, the FRET data revealed that inter-molecular FRET was neglectable (Figure 30). The significant increase of the H-Tet-Cy3 signal for $\alpha 2^{S181}$ GABA-A receptors indicated the binding of H-Tet-Cy3 and H-Tet-Cy5 within the same receptor. This proves that tetrazine functionalized fluorophores can label two individual subunits in the range of ~ 5 nm distance between two click sites (based on the S181-click sites in the α -subunits of the PDB model 6HUG). The two fluorophores Cy3 and Cy5 show 50% FRET efficiency at a Förster radius of R_0 5.27 nm. Under these circumstances, the H-Tet-Cy3 signal should theoretically increase to a factor of two post photobleaching of the H-Tet-Cy5 acceptor fluorophore. The lower increase of H-Tet-Cy3 (factor 1.4) in the $\alpha 2^{S181}$ GABA-AR approach can be explained

by several reasons. On the one hand, the distance between two $\alpha 2^{S181}$ click sites is smaller than the Förster radius, which can influence the FRET signal. On the other hand, there were differences in the intensities obtained from H-Tet-Cy3 and H-Tet-Cy5, which indicate better binding of either H-Tet-Cy3 or H-Tet-Cy5 caused by random diffusion effects. This could entail a reduction in the obtained FRET signal. Furthermore, it has to be taken into account that both tetrazine-dyes, H-Tet-Cy3 and H-Tet-Cy5, compete for binding to the unnatural amino acid TCO*-K. H-Tet-Cy3 and H-Tet-Cy5 are characterized by a similar reaction rate to TCO*-K²⁵⁹ and hence enable four statistical possibilities to fluorescently label the $\alpha 2^{S181}$ GABA-A receptor dimer. Either both subunits were labeled with Cy5 (Cy5-Cy5) or Cy3 (Cy3-Cy3) or each subunit was labeled with one Cy3 and one Cy5 fluorophore (Cy3-Cy5 or Cy5-Cy3). Considering this, 25% of dimeric receptors are stochastically labeled with Cy3-Cy3, which can increase the initial fluorescence of Cy3 (pre-bleaching) but cannot show FRET signal after acceptor bleaching. Therefore, a FRET factor of ~ 1.4 seems reasonable for the dimeric $\alpha 2^{S181}$ GABA-A receptors. Next, the clickable $\alpha 2^{S181}$ dimer was characterized applying the super-resolution microscopy method *d*STORM (Figure 31). Surprisingly, the determined localization per cluster for $\alpha 2^{S181}$ GABA-A receptors was independent of the H-Tet-Cy5 concentration. Theoretically, an $\alpha 2$ dimer labeled with two Cy5 fluorophores should exhibit a higher number of localizations per cluster compared to an $\alpha 2$ dimer with just one Cy5 dye. Nonetheless, even underlabeling of GABA-A receptor dimers with low H-Tet-Cy5 concentrations (50 nM or 150 nM) revealed the same number of localizations per cluster compared to H-Tet-Cy5 saturation concentrations (3 μ M and 6 μ M). To follow up on this observation, the clickable variant of the single subunit $\gamma 2$ of GABA-A receptors was compared to clickable $\alpha 2$ dimers concerning the localizations per cluster. Again, monomeric $\gamma 2$ and dimeric $\alpha 2$ dimers showed similar localizations per cluster when labeled with H-Tet-Cy5. These observations indicate that even when two tetrazines can successfully label the $\alpha 2$ dimer (confirmed by FRET), it is not possible to resolve its dimeric character by localization microscopy such as *d*STORM. This phenomenon might be explained by the fact that fluorophores communicate with each other in the nearfield (≤ 5 nm) via HOMO-FRET, which results in two fluorophores behaving like one single emitter³²⁵. Interestingly, the attempt to increase the distance between the two fluorophores binding the $\alpha 2$ GABA-A receptor dimer by using H-Tet-Digoxigenin and anti-Digoxigenin antibodies exhibited still the same number of localizations per cluster. In addition, comparison to clickable $\alpha 2$ GABA-A receptors labeled with anti-HA antibody showed similar results. Overall, the observations revealed that labeling of multimeric complexes with binding sites close together (~ 5 nm) brings along two issues: first, antibodies might fail to detect more than

one binding site due to steric hindrance; second, small labels such as tetrazine functionalized fluorophores might come too close to each other, resulting in fluorophore annihilation. Consequently, the blinking behavior of the clickable $\alpha 2$ GABA-A receptor labeled with two H-Tet-Cy5 molecules is influenced by these effects. This results in identical localizations per cluster compared to the clickable $\gamma 2$ GABA-A receptor carrying just one H-Tet-Cy5.

Finally, the issues associated with fluorophores being in too close contact was circumvented by physically expanding the membrane receptors using expansion microscopy. To achieve this the X10 expansion protocol was utilized as described previously²⁹⁸. In a first attempt HEK293T cells expressing either clickable $\alpha 2^{S181}$ or $\gamma 2^{L198}$ GABA-A receptors were labeled with 3 μ M Pyr-Tet-ATTO643 prior gelation and digestion with Proteinase K. Fluorescence signal was checked post-digestion, when gels were expanded approximately to a factor of ~ 2 , showing clear signal in the equatorial membrane of $\alpha 2^{S181}$ and lower signal for $\gamma 2^{L198}$ receptors (Figure 32). However, fluorescence signal could not be detected in fully expanded gels (factor ~ 8), neither at the CLSM nor with single-molecule sensitive detectors at the SIM (data not shown) even with maximal laser power. Concerning labeling stoichiometry, bioorthogonal labeling offers a 1:1 ratio with one fluorophore per tetrazine molecule (degree of labeling (DOL) = 1). This might be advantageous in cluster analysis since every fluorescent signal corresponds to a single click labeled protein of interest. Unfortunately, in expansion microscopy the fluorescent signal is diluted by the physical expansion of the specimen. That is, an 8-fold expanded hydrogel offers a dilution factor of ~ 512 (8 times in three dimensions = $8^3 = 512$), reducing the fluorescence intensity significantly. Furthermore fluorophores lose intensity during the gelation process through destruction by monomer radicals²⁸⁹. To avoid this fluorescence loss, receptors bearing incorporated TCO*-K were labeled post-gelation with Pyr-Tet-ATTO643. Again, no fluorescence was detected in 2-fold and 8-fold expanded specimen. One explanation might be that the C-C double bond in the alkene was attacked during the radical polymerization. Similar effects are reported to cause the fluorescence decrease of cyanine dyes such as Alexa Fluor 647²⁸⁹. Therefore, the TCO*-K group cannot react with tetrazine-dyes which results in only unspecific fluorescence. Since these experiments demonstrated that pre-labeling with tetrazine conjugates is the more reliable way to achieve sufficient labeling of clickable receptors, the fluorescent signal was amplified using tetrazines coupled to digoxigenin. These dyes were then subsequently labeled with anti-digoxigenin antibodies (anti-Digoxigenin CF568, DOL = 2.3). The dye CF568 was used for this approach since fluorescence signal was maintained after gelation and digestion similar to ATTO643. Utilizing anti-Digoxigenin antibodies, clickable $\alpha 2^{S181}$ and $\gamma 2^{L198}$ GABA-A receptors could be successfully visualized at the equatorial

membrane of 2- and 8-fold expanded HEK293T cells (Figure 32). Taking into consideration that the click sites between two $\alpha 2$ GABA-A subunits are ~ 5 nm apart and each of the two anti-digoxigenin antibodies add ~ 9 nm distance on top, the total distance between the fluorophores attached to both $\alpha 2$ subunits amount to 23 nm. Depending on where the fluorophore is conjugated to the antibody, the maximal distance between the two fluorophores in a GABA-A receptor dimer in an 8-fold expanded gel would be ~ 184 nm. This is below the resolution limit of a CLSM microscope but could be imaged via SIM microscopy in the future.

5 Conclusion and Outlook

In this work GCE and bioorthogonal labeling were applied on synaptic KARs, TARPs and GABA-ARs. All of the proteins could be labeled by incorporation of the unnatural amino acid TCO*-K and subsequent targeting via tetrazine functionalized fluorophores. Finally, the opportunities and challenges associated with bioorthogonal labeling and possible future directions of this approach will be discussed.

5.1 Bioorthogonal labeling of hard-to-access proteins

Due to the small label size and feasibility to address a single unnatural amino acid, click chemistry can be a powerful tool to target proteins in narrow or protein dense compartments. While labeling of KARs was only possible with conventional antibodies targeting an intracellular epitope, GCE and bioorthogonal labeling allowed attachment of a fluorescent label to various click sites at the extracellular domain of GluK2 homo-tetramers outcompeting conventional immunolabeling using antibodies. Similarly, anti- $\alpha 2$ antibodies targeting GABA-A receptors showed insufficient binding to overexpressed GABA-ARs compared to click labeled receptors (Figure 23). More interestingly, anti-TARP antibodies revealed efficient labeling of overexpressed TARPs, but failed to bind TARPs complexed with AMPARs. It can be speculated that this effect is caused by steric hindrance of complexed proteins. Here, targeting a single amino acid via click chemistry is advantageous compared to antibody epitope recognition of multiple amino acids and hence allows efficient labeling of clickable $\gamma 2$ and $\gamma 8$ TARPs associated with AMPARs. Since GCE and bioorthogonal labeling were applied to multiple hard-to-target proteins of interest, the technique can be transferred to further proteins targets that face similar constraints regarding epitope accessibility.

5.2 Bioorthogonal labeling to study protein-protein interactions

Protein interactions are essential for signal transduction and therefore their investigation is key to understanding cellular processes³²⁶. Fluorescence lifetime imaging in combination with fluorescence resonance energy transfer (FLIM-FRET) experiments can be utilized to study interactions of proteins in close contact³²⁷. Since the Förster radius of the FRET pair Alexa Fluor 488 and Cy3 is ~6.8 nm, it is crucial to have a minimal linkage error between the two fluorophores to obtain optimal FRET signal. Combination of clickable TARPs (H-Tet-Cy3) and SNAP-tagged GluA1 AMPARs (BG-AF488) showed significant reduction of the fluorescence

lifetime of the acceptor fluorophore AF488³⁰⁸. This validated close contact between clicked $\gamma 2$ or $\gamma 8$ TARPs and SNAP-tagged GluA1 AMPARs. Even if an antibody-accessible epitope would be present in TARP-AMPA complexes, substitution of the tetrazine functionalized FRET donor (~ 1 nm) with an antibody (~ 10 nm) would increase the linkage error by a factor of ~ 10 and could influence the FRET efficiency. Hence, FRET approaches using tetrazine-fluorophores together with SNAP-ligands can help to understand protein complexes in a more precise manner. This method can also be applied on other multi-protein complexes such as functional GluK2-GluK5 hetero-tetramers²⁵. Furthermore, KAR interaction with Neto proteins (Neto1, Neto2) or PSD95 could be further investigated. Clickable KARs and SNAP-tagged GluK5 receptors or SNAP-tagged auxiliary subunits like Neto1 and Neto2 can help to understand the intra-molecular organization of GluK2-GluK5 tetramers and the interaction of KARs with Neto proteins³²⁸ and PSD95¹⁴¹. Even though various interaction partners of GABA-A receptors such as gephyrin, collybistin and neuroligins were identified previously^{163,169}, dynamics of these protein-protein interactions still remain elusive. FRET experiments with clickable GABA-A receptor subunits and SNAP-tagged interaction partners can help to understand the underlying mechanisms. Besides FRET imaging, protein-protein complexes can be studied with multi-color *d*STORM imaging by labeling with two tetrazine-dyes such as H-Tet-Cy5 and H-Tet-CF568, in 1:1 stoichiometry. This could enable co-localization of adjacent proteins by reducing the linkage error between the two molecules to a minimum. However, both tetrazines target the unnatural amino acid TCO*-K incorporated into the two different proteins, which can impede the co-localization. A potential tradeoff could be to use one click label (H-Tet-Cy5) in combination with a SNAP-ligand (BG-AF532) as second label. Additionally, there are approaches to introduce multiple unnatural amino acids into a protein of interest by utilizing orthogonal ribosomes that can decode quadruplet codons³²⁹. In the future, this will precise and site-specific labeling of either multiple sites within a single protein or between interacting proteins. Most definitely, this novel approach will contribute to a more detailed understanding of protein-protein interactions in neuronal cultures.

5.3 Bioorthogonal labeling to advance trafficking approaches

In addition to the previously mentioned fields of application, bioorthogonal labeling can be utilized to investigate the diffusional behavior of receptors as well. Synaptic receptors are highly mobile in synaptic and extrasynaptic areas¹¹. Investigations on these trafficking behavior of synaptic proteins is often performed with antibodies coupled to bright quantum dots (~ 12

nm). While this allows specific binding and easy detection of the targeted receptor, application of this method can entail accessibility issues in the synaptic cleft caused by label size⁵³. In contrast, the application of bioorthogonal labeling (~1 nm) in neuronal studies allows target binding at limited space in the synaptic cleft. For instance, the molecular organization of clickable $\gamma 2$ and $\gamma 8$ TARPs could be analyzed in extrasynaptic and synaptic areas, revealing aggregation of $\gamma 2$ TARPs in synapses. It should be mentioned, that the molecular weight of a tetrazine-dye (826 g/mol for H-Tet-Cy5) compared to an antibody (~150.000 g/mol) is substantially lower. As receptor diffusion is influenced by the attached fluorescent label, this quality can be especially advantageous in tracking experiments. FRAP experiments on clickable GABA-ARs confirmed that incorporation of the unnatural amino acid TCO*-K does not negatively affect the diffusional behavior of the receptors. On that basis, it would be intriguing to know whether tetrazine-dyes could be utilized for tracking experiments over a longer period of time as well. Preliminary tracking data of GABA-ARs with photostable Pyr-Tet-ATTO643 exhibited fast bleaching of the fluorophore. To achieve a trade-off between smaller label size and fluorophore brightness/stability, tetrazines coupled to quantum dots instead of fluorophores might therefore be a suitable alternative to antibody-quantum dot conjugates.

Crosslinking experiments, connecting multiple AMPARs via neutravidin, resulted in trapping of these surface exposed receptors. Additionally, these studies confirmed that an intracellular pool of AMPARs contributes to AMPAR trafficking to the cell membrane⁹⁸. Similar crosslinking could also be achieved by using GCE and bioorthogonal labeling with bistetrazines as demonstrated previously²⁶². In neuronal cultures, this system could be exploited to understand GABA-AR diffusion between synaptic and extrasynaptic terminals and exocytosis of GABA-ARs to the cell surface. Since crosslinking of receptors via autoantibodies can induce receptor internalization³¹⁹, crosslinking experiments utilizing GCE and bioorthogonal labeling will give insights into transport of newly synthesized GABA-ARs in synaptic areas.

5.4 Optimization of bioorthogonal labeling in neuronal cultures

Expression of clickable proteins in neuronal cultures remains challenging and requires optimization of standard transfection procedures and transfected DNA. Clickable GABA-ARs were successfully transfected in adult primary neurons with effectene at DIV14. At this point, all necessary interaction partners of GABA-ARs are expressed ensuring successful incorporation of GABA-ARs in neuronal membranes. Nevertheless, the expression efficiency

of clickable GABA-ARs in adult neurons was very low. For the transfection of clickable TARPs, a different approach was utilized. Here, the primary hippocampal neurons were transfected early at DIV3-4 with one plasmid encoding the PylRS together with the clickable TARP and a second plasmid carrying the tRNA^{Pyl} under the doxycycline inducible promoter TetON3G. Doxycycline and unnatural amino acid TCO*-K were added to adult neurons at DIV16-18 to induce tRNA^{Pyl} expression and subsequent incorporation of TCO*-K into the clickable TARP for a limited time period. This procedure allowed better-established synapses with efficient expression of interaction partners and limited toxicity for the neurons, which overall boosted the expression efficiency of clickable TARPs. Moreover, using the same plasmids for single-cell electroporation of organotypic hippocampal slices allowed bioorthogonal labeling of clickable $\gamma 2$ and $\gamma 8$ TARPs in CA1 pyramidal cells with high specificity³⁰⁸. In the future, it will be also advantageous to control the expression of the plasmid with the PylRS and the clickable TARP. Otherwise, the high levels of truncated TARPs and expressed PylRS might cause toxicity for the neurons even before the unnatural amino acid and doxycycline will be supplied at DIV16-18. Additionally, utilizing adeno-associated viruses (AAV) or lentiviruses for the transduction of neuronal cells with plasmids encoding the tRNA^{Pyl}/PylRS and the clickable protein appears promising to enhance the transfection efficiency even further. Vectors commonly used for transfection of mammalian often contain the CMV promoter. Since the CMV promoter is silenced in adult neurons, which can impede the protein expression in these cells³³⁰, it is advisable to exchange the CMV promoter to the neuronal hSynapsin or CaMKII promoter. This ensures a more native protein expression without silencing. Furthermore, the insufficient incorporation of unnatural amino acids at click sites during translation is another step limiting the expression of clickable proteins. Improving the incorporation of unnatural amino acids by using orthogonal ribosomes can also help optimizing expression efficiencies^{331,332}. Alternatively, all endogenous amber stop codons (UAG) could be replaced with ochre stop codons (UAA), which allows deletion of the RF1 competing for binding to the UAG codon. This would also improve the incorporation of unnatural amino acids at the selected clicking position. While this method was established for E.coli, it is hardly applicable on more complex organisms³³³. Finally, GCE requires an overexpressed cell system. This might influence the native characteristics of the expressed proteins in the cellular context. To avoid this artificial system a future approach might exploit the CRISPR/Cas9 machinery to knock-in specific click sites into endogenous proteins of interest³³⁴.

5.5 Advancing click chemistry to investigate multimeric receptors

Bioorthogonal labeling offers a small linkage error between fluorophore and target (~1 nm). Regarding this advantage, the click system is suited to investigate multimeric receptors in cases where antibodies face difficulties labeling every single subunit due to steric hindrance. FRET experiments confirmed binding of one tetrazine to clickable $\gamma 2$ GABA-ARs (monomer) and of more than one tetrazine to clickable $\alpha 2$ GABA-ARs (dimer) or clickable KARs (tetramer). However, *d*STORM experiments revealed no dimeric or tetrameric character of these receptors based on the localizations per cluster. Measurements of click site distances in α^{S181} GABA-ARs revealed a distance of ~4.8 nm between two α subunits (PDB 6HUG). Distances in the GluK2^{S309} homo-tetramer (A, B, C, D) were determined to be ~1.8 nm (B-D), ~5.8 nm (A-B), ~5.6 nm (C-D), ~7.4 nm (A-D), ~7.4 nm (B-C) and ~11.9 nm (A-C) (Figure 8) (PDB 5KUF). Considering the occurrence of HOMO-FRET events within the range of ~5 nm, it is expectable that GABA-AR $\alpha 2$ dimers show similar localizations per cluster compared to $\gamma 2$ monomers. Concerning the KAR GluK2^{S309} homo-tetramer, at least the two click sites A and C with a distance of about 12 nm should be detectable by a higher amount of localizations per cluster. In these experiments, all *d*STORM images were acquired with an exposure time of 15 ms per frame. Preliminary investigations in collaboration with Dominic Helmerich using lower exposure times (5 ms per frame) indicate, that multimeric receptors exhibit a higher number of on-events (tracked localizations) with a reduced off-time compared to monomeric membrane proteins. With an exposure time of 15 ms per frame and an average on-time of ~9 ms, the on and off-times of each fluorophore cannot be separated precisely. As a consequence, the higher number of on-events cannot be deciphered. Imaging with 5 ms exposure time seems to be a potential adjustment in *d*STORM measurements in order to reveal multiple fluorophores even if they are separated by only a few nanometers. To conclude, bioorthogonal labeling via tetrazine functionalized fluorophores enables labeling of multimeric receptors, which could be verified by FRET and *d*STORM experiments. In *d*STORM recordings, only the use of low exposure times allowed visualization of the receptors multimeric character via a higher amount of on-events. However, reconstructed *d*STORM images could not pinpoint isolated emitters in a multimeric receptor due to the resolution limit of ~20 nm. To achieve sub-10 nm resolution, the combination of click chemistry labeling with expansion microscopy (click-ExM) might be an alternative approach. For this purpose, a promising way to label the sample are tetrazine functionalized fluorophores such as Pyr-Tet-ATTO643. Commercially available Pyr-Tet-ATTO643 comprises only one fluorophore attached to the tetrazine (DOL 1), which results in undetectable fluorescence signal in 8-fold expanded hydrogels. Novel and brighter

fluorophores could potentially survive the gelation and in this case will help to promote the approach of click-ExM. Additionally, dyes such as the CF568, which are suitable for *d*STORM and ExM, could be utilized for click-ExM protocols. Samples could be pre-labeled with H-Tet-CF568 followed by 4-fold expansion and subsequent re-embedding. This would allow a click-ExM approach in combination with *d*STORM as demonstrated previously for antibody labeling²⁹⁵. Since the unnatural amino acid TCO*-K seems to get lost during the gelation process, a post-labeling approach with tetrazine-dyes is not possible at the moment. However, protecting Cy5 fluorophores via phosphine quenching with TCEP can allow survival of pre-labeled Cy5 samples for expansion microscopy³³⁵. A similar approach modified for TCO*-K tagged specimen might enable post-labeling with tetrazine-dyes. Another crucial point concerning expansion microscopy is the crosslinking of the specimen into the polyacrylamide gel. Studies showed that this can be achieved by glutaraldehyde or AcX^{288,289}. Clickable samples exhibited the best gel incorporation, when treated with AcX. The AcX reacts with free amino groups of lysines, which will be linked in the hydrogel. However it is not guaranteed that all amino groups are reacted with the AcX. Furthermore, since the crosslinker is not attached directly to the fluorophore, it is possible that the fluorescent label is cut during the Proteinase K digest depending on the amino acid sequence next to the attached fluorophore. To ensure site-specific labeling of target structures with fluorescent labels as well as crosslinking in the expansion gel tri-functional linkers may be a promising strategy³³⁶. Such a linker can consist of a tetrazine molecule binding the clickable target structure, a photostable fluorophore that can survive ExM processing (e.g. ATTO643) and an acryloyl group for crosslinking in the hydrogel. Initial experiments performed with this tri-functional linker showed incorporation of the sample in the hydrogel but revealed lower fluorescence signal compared to AcX linked specimen. Another potential approach may use a trifunctional linker exploiting multiple acryloyl groups to promote the incorporation of the label into the hydrogel. Since the DOL 1 of the tetrazine functionalized fluorophore showed no fluorescence in fully expanded gels (8x), signal amplification methods were tested. For this, either tetrazine functionalized biotins were combined with streptavidin-dyes or tetrazines carrying a digoxigenin tag were utilized. The signal of the latter was subsequently amplified by anti-digoxigenin antibody binding. Both approaches enabled fluorescence detection of clickable multimeric receptors in 8-fold expanded gels. However, preliminary data obtained from SIM imaging revealed dimeric structures not only for dimeric but also for monomeric receptors. These artifacts might be caused by the strong fixation using glutaraldehyde, clustering of antibodies/streptavidins or anisotropic expansion

after digestion with Proteinase K. Optimization of expansion protocols by using milder fixation or heat denaturation instead of enzymatic protein digestion might reduce these labeling artifacts.

5.6 Bioorthogonal labeling to tackle pathologies

Bioorthogonal labeling can provide a powerful tool for understanding and even treating pathologies. Limbic encephalitis for instance is associated with GABA-AR autoantibodies^{337,338}. These pathogenic autoantibodies might influence the mobility of GABA-ARs in synaptic and extrasynaptic areas. Clickable GABA-ARs labeled with tetrazine-dyes will allow visualization of these receptors in pathological conditions and thereby help to understand the impact of autoantibodies in limbic encephalitis without inducing a bulky label.

Cancer therapies are another important field of application for bioorthogonal click chemistry. Genetically modified patient T cells expressing a chimeric antigen receptor (CAR) are utilized for cellular immunotherapy of blood cancer. Through recognition of specific tumor associated antigens (TAAs) via CARs, these T cells are able to identify and target tumor cells. However, CAR-T cells showed severe side-effects due to on-target/off-tumor binding, which leads to targeting and killing of healthy cells. Furthermore it should be also noted, that CAR-T cells often struggle to infiltrate solid tumors³³⁹. Click chemistry can potentially promote CAR-T cell mediated immunotherapy by addressing these issues. For instance, anti-CD19 directed CAR-T cells were additionally azide-modified via incorporation of Ac₄GalNAz sugars into the cell surface. Simultaneously, the tumor cells were incubated with Ac₄ManN-BCN sugars to introduce the unnatural amino acid BCN to the cell membrane. The click reaction between BCN and azide will then promote efficient binding of CAR-T cells to and killing of the respective tumor cells and hence minimize on-target/off-tumor effects. Furthermore, this method can help infiltration and accumulation of CAR-T cells at solid tumors³⁴⁰. Concerning clickable CAR-T cells it is also a possibility to advance GCE to introduce an unnatural amino acid such as TCO*-K into the CAR. Local injection of tetrazine molecules into the solid tumor will then promote direction of clickable CAR-T cells to the cancer cells. Another novel application relies on TCO molecules carrying a prodrug. Upon tetrazine binding to TCO, cleavage and activation of the attached prodrug are induced³⁴¹. A clinical study (phase 1) utilizes this principle via a TCO-modified Doxorubicin prodrug and a locally injected tetrazine-modified biopolymer³⁴². This method exhibited a 83-fold lower toxicity compared to standard Doxorubicin in vitro. Since click chemistry components are orthogonal, there should be nearly no interactions with biomolecules in the human body. Due to that, the toxicity of these approaches is expected to

be very low in general. In conclusion, bioorthogonal labeling provides a wide range of opportunities for various applications. In basic research, the method facilitates site-specific targeting of proteins, investigation of protein-protein interactions and analysis of multimeric receptors. Ultimately, bioorthogonal labeling will contribute to advanced therapies addressing severe pathologies in the future.

6 References

1. Olsen RW, Sieghart W. GABA A receptors: subtypes provide diversity of function and pharmacology. *Neuropharmacology*. 2009;56(1):141–148.
2. Dutertre S, Becker C-M, Betz H. Inhibitory glycine receptors: an update. *J Biol Chem*. 2012;287(48):40216–40223.
3. Bliss TV, Lomo T. Long-lasting potentiation of synaptic transmission in the dentate area of the anaesthetized rabbit following stimulation of the perforant path. *J Physiol*. 1973;232(2):331–356.
4. Collingridge GL, Peineau S, Howland JG, Wang YT. Long-term depression in the CNS. *Nat Rev Neurosci*. 2010;11(7):459–473.
5. Enoki R, Hu Y-L, Hamilton D, Fine A. Expression of long-term plasticity at individual synapses in hippocampus is graded, bidirectional, and mainly presynaptic: optical quantal analysis. *Neuron*. 2009;62(2):242–253.
6. Bliss TV, Collingridge GL. A synaptic model of memory: long-term potentiation in the hippocampus. *Nature*. 1993;361(6407):31–39.
7. Scannevin RH, Huganir RL. Postsynaptic organization and regulation of excitatory synapses. *Nat Rev Neurosci*. 2000;1(2):133–141.
8. Derkach V, Barria A, Soderling TR. Ca²⁺/calmodulin-kinase II enhances channel conductance of alpha-amino-3-hydroxy-5-methyl-4-isoxazolepropionate type glutamate receptors. *Proc Natl Acad Sci U S A*. 1999;96(6):3269–3274.
9. Borgdorff AJ, Choquet D. Regulation of AMPA receptor lateral movements. *Nature*. 2002;417(6889):649–653.
10. Dahan M, Lévi S, Luccardini C, Rostaing P, Riveau B, Triller A. Diffusion dynamics of glycine receptors revealed by single-quantum dot tracking. *Science*. 2003;302(5644):442–445.
11. Triller A, Choquet D. New concepts in synaptic biology derived from single-molecule imaging. *Neuron*. 2008;59(3):359–374.
12. Daniel Choquet, Antoine Triller. The Dynamic Synapse. *Neuron*. 2013;80(3):691–703.
13. Nair D, Hosity E, Petersen JD, Constals A, Giannone G, Choquet D, Sibarita J-B. Super-resolution imaging reveals that AMPA receptors inside synapses are dynamically organized in nanodomains regulated by PSD95. *J Neurosci*. 2013;33(32):13204–13224.
14. Biederer T, Kaeser PS, Blanpied TA. Transcellular Nanoalignment of Synaptic Function. *Neuron*. 2017;96(3):680–696.
15. Hruska M, Henderson N, Le Marchand SJ, Jafri H, Dalva MB. Synaptic nanomodules underlie the organization and plasticity of spine synapses. *Nat Neurosci*. 2018;21(5):671–682.
16. Liauw J, Hoang S, Choi M, Eroglu C, Choi M, Sun G, Percy M, Wildman-Tobriner B, Bliss T, Guzman RG, et al. Thrombospondins 1 and 2 are necessary for synaptic plasticity and functional recovery after stroke. *J Cereb Blood Flow Metab*. 2008;28(10):1722–1732.
17. Hennekinne L, Colasse S, Triller A, Renner M. Differential control of thrombospondin over synaptic glycine and AMPA receptors in spinal cord neurons. *J Neurosci*. 2013;33(28):11432–11439.
18. Charrier C, Machado P, Tweedie-Cullen RY, Rutishauser D, Mansuy IM, Triller A. A crosstalk between β 1 and β 3 integrins controls glycine receptor and gephyrin trafficking at synapses. *Nat Neurosci*. 2010;13(11):1388–1395.
19. Zhang H, Etherington L-A, Hafner A-S, Belelli D, Coussen F, Delagrèze P, Chaouloff F, Spedding M, Lambert JJ, Choquet D, et al. Regulation of AMPA receptor surface trafficking and synaptic plasticity by a cognitive enhancer and antidepressant molecule. *Mol Psychiatry*. 2013;18(4):471–484.
20. Khayenko V, Maric HM. Targeting GABAAR-Associated Proteins: New Modulators, Labels and Concepts. *Front. Mol. Neurosci*. 2019;12:162.

21. Traynelis SF, Wollmuth LP, McBain CJ, Menniti FS, Vance KM, Ogden KK, Hansen KB, Yuan H, Myers SJ, Dingledine R. Glutamate receptor ion channels: structure, regulation, and function. *Pharmacol Rev.* 2010;62(3):405–496.
22. Greger IH, Mayer ML. Structural biology of glutamate receptor ion channels: towards an understanding of mechanism. *Curr Opin Struct Biol.* 2019;57:185–195.
23. Ayalon G, Stern-Bach Y. Functional Assembly of AMPA and Kainate Receptors Is Mediated by Several Discrete Protein-Protein Interactions. *Neuron.* 2001;31(1):103–113.
24. Meyerson JR, Kumar J, Chittori S, Rao P, Pierson J, Bartesaghi A, Mayer ML, Subramaniam S. Structural mechanism of glutamate receptor activation and desensitization. *Nature.* 2014;514(7522):328–334.
25. Kumar J, Schuck P, Mayer ML. Structure and assembly mechanism for heteromeric kainate receptors. *Neuron.* 2011;71(2):319–331.
26. Meyerson JR, Chittori S, Merk A, Rao P, Han TH, Serpe M, Mayer ML, Subramaniam S. Structural basis of kainate subtype glutamate receptor desensitization. *Nature.* 2016;537(7621):567–571.
27. Dürr KL, Chen L, Stein RA, Zorzi R de, Folea IM, Walz T, Mchaourab HS, Gouaux E. Structure and dynamics of AMPA receptor GluA2 in resting, pre-open, and desensitized states. *Cell.* 2014;158(4):778–792.
28. Kumari J, Vinnakota R, Kumar J. Structural and Functional Insights into GluK3-kainate Receptor Desensitization and Recovery. *Sci Rep.* 2019;9(1):10254.
29. Greger IH, Watson JF, Cull-Candy SG. Structural and Functional Architecture of AMPA-Type Glutamate Receptors and Their Auxiliary Proteins. *Neuron.* 2017;94(4):713–730.
30. Wollmuth LP, Sobolevsky AI. Structure and gating of the glutamate receptor ion channel. *Trends Neurosci.* 2004;27(6):321–328.
31. Twomey EC, Sobolevsky AI. Structural Mechanisms of Gating in Ionotropic Glutamate Receptors. *Biochemistry.* 2018;57(3):267–276.
32. Jackson AC, Nicoll RA. The expanding social network of ionotropic glutamate receptors: TARPs and other transmembrane auxiliary subunits. *Neuron.* 2011;70(2):178–199.
33. Shanks NF, Savas JN, Maruo T, Cais O, Hirao A, Oe S, Ghosh A, Noda Y, Greger IH, Yates JR, et al. Differences in AMPA and kainate receptor interactomes facilitate identification of AMPA receptor auxiliary subunit GSG1L. *Cell Rep.* 2012;1(6):590–598.
34. McGee TP, Bats C, Farrant M, Cull-Candy SG. Auxiliary Subunit GSG1L Acts to Suppress Calcium-Permeable AMPA Receptor Function. *J Neurosci.* 2015;35(49):16171–16179.
35. Sigel E, Steinmann ME. Structure, function, and modulation of GABA(A) receptors. *J Biol Chem.* 2012;287(48):40224–40231.
36. Zhu S, Noviello CM, Teng J, Walsh RM, Kim JJ, Hibbs RE. Structure of a human synaptic GABAA receptor. *Nature.* 2018;559(7712):67–72.
37. Masiulis S, Desai R, Uchański T, Serna Martin I, Laverty D, Karia D, Malinauskas T, Zivanov J, Pardon E, Kotecha A, et al. GABAA receptor signalling mechanisms revealed by structural pharmacology. *Nature.* 2019;565(7740):454–459.
38. Bradley RJ, Harris RA, editors. *International review of neurobiology*, v. 38. San Diego: Academic Press; 1995. 372 p. (International Review of Neurobiology). ISBN: 9780123668387.
39. Whiting PJ, McKernan RM, Wafford KA. Structure and Pharmacology of Vertebrate GABAA Receptor Subtypes. In: Bradley RJ, Harris RA, editors. *International review of neurobiology*, v. 38. Vol. 38. San Diego: Academic Press; 1995. p. 95–138 (International Review of Neurobiology).
40. Sigel E. The benzodiazepine binding site of GABAA receptors. *Trends in Pharmacological Sciences.* 1997;18(11):425–429.
41. Wagner DA, Czajkowski C. Structure and Dynamics of the GABA Binding Pocket: A Narrowing Cleft that Constricts during Activation. *J Neurosci.* 2001;21(1):67–74.
42. Chen Z-W, Olsen RW. GABAA receptor associated proteins: a key factor regulating GABAA receptor function. *J Neurochem.* 2007;100(2):279–294.

43. Jacob TC, Moss SJ, Jurd R. GABA(A) receptor trafficking and its role in the dynamic modulation of neuronal inhibition. *Nat Rev Neurosci.* 2008;9(5):331–343.
44. Zuber B, Nikonenko I, Klauser P, Muller D, Dubochet J. The mammalian central nervous synaptic cleft contains a high density of periodically organized complexes. *Proc Natl Acad Sci U S A.* 2005;102(52):19192–19197.
45. Gray EG. Electron microscopy of synaptic contacts on dendrite spines of the cerebral cortex. *Nature.* 1959;183(4675):1592–1593.
46. Hussey AM, Chambers JJ. Methods to locate and track ion channels and receptors expressed in live neurons. *ACS Chem Neurosci.* 2015;6(1):189–198.
47. Choquet D, Sainlos M, Sibarita J-B. Advanced imaging and labelling methods to decipher brain cell organization and function. *Nat Rev Neurosci.* 2021;22(4):237–255.
48. Masugi-Tokita M, Shigemoto R. High-resolution quantitative visualization of glutamate and GABA receptors at central synapses. *Curr Opin Neurobiol.* 2007;17(3):387–393.
49. Saxton MJ, Jacobson K. Single-particle tracking: applications to membrane dynamics. *Annu Rev Biophys Biomol Struct.* 1997;26:373–399.
50. Guo S-M, Veneziano R, Gordonov S, Li L, Danielson E, Perez de Arce K, Park D, Kulesa AB, Wamhoff E-C, Blainey PC, et al. Multiplexed and high-throughput neuronal fluorescence imaging with diffusible probes. *Nat Commun.* 2019;10(1):4377.
51. Klevanski M, Herrmannsdoerfer F, Sass S, Venkataramani V, Heilemann M, Kuner T. Automated highly multiplexed super-resolution imaging of protein nano-architecture in cells and tissues. *Nat Commun.* 2020;11(1):1552.
52. Chamma I, Letellier M, Butler C, Tessier B, Lim K-H, Gauthereau I, Choquet D, Sibarita J-B, Park S, Sainlos M, et al. Mapping the dynamics and nanoscale organization of synaptic adhesion proteins using monomeric streptavidin. *Nat Commun.* 2016;7(1):10773.
53. Giannone G, Mondin M, Grillo-Bosch D, Tessier B, Saint-Michel E, Czöndör K, Sainlos M, Choquet D, Thoumine O. Neurexin-1 β binding to neuroligin-1 triggers the preferential recruitment of PSD-95 versus gephyrin through tyrosine phosphorylation of neuroligin-1. *Cell Rep.* 2013;3(6):1996–2007.
54. Helma J, Cardoso MC, Muyltermans S, Leonhardt H. Nanobodies and recombinant binders in cell biology. *J Cell Biol.* 2015;209(5):633–644.
55. Bedford R, Tiede C, Hughes R, Curd A, McPherson MJ, Peckham M, Tomlinson DC. Alternative reagents to antibodies in imaging applications. *Biophys Rev.* 2017;9(4):299–308.
56. Tamura T, Hamachi I. Chemistry for Covalent Modification of Endogenous/Native Proteins: From Test Tubes to Complex Biological Systems. *J Am Chem Soc.* 2019;141(7):2782–2799.
57. Wakayama S, Kiyonaka S, Arai I, Kakegawa W, Matsuda S, Ibata K, Nemoto YL, Kusumi A, Yuzaki M, Hamachi I. Chemical labelling for visualizing native AMPA receptors in live neurons. *Nat Commun.* 2017;8(1):14850.
58. Arttamangkul S, Plazek A, Platt EJ, Jin H, Murray TF, Birdsong WT, Rice KC, Farrens DL, Williams JT. Visualizing endogenous opioid receptors in living neurons using ligand-directed chemistry. *Elife.* 2019;8.
59. Brecht DS, Nicoll RA. AMPA Receptor Trafficking at Excitatory Synapses. *Neuron.* 2003;40(2):361–379.
60. Rodriguez EA, Campbell RE, Lin JY, Lin MZ, Miyawaki A, Palmer AE, Shu X, Zhang J, Tsien RY. The Growing and Glowing Toolbox of Fluorescent and Photoactive Proteins. *Trends Biochem Sci.* 2017;42(2):111–129.
61. Lambert TJ. FPbase: a community-editable fluorescent protein database. *Nat Methods.* 2019;16(4):277–278.
62. Jradi FM, Lavis LD. Chemistry of Photosensitive Fluorophores for Single-Molecule Localization Microscopy. *ACS Chem Biol.* 2019;14(6):1077–1090.
63. Li H, Vaughan JC. Switchable Fluorophores for Single-Molecule Localization Microscopy. *Chem Rev.* 2018;118(18):9412–9454.

64. Keppler A, Pick H, Arrivoli C, Vogel H, Johnsson K. Labeling of fusion proteins with synthetic fluorophores in live cells. *Proc Natl Acad Sci U S A*. 2004;101(27):9955–9959.
65. Gautier A, Juillerat A, Heinis C, Corrêa IR, Kindermann M, Beaufils F, Johnsson K. An engineered protein tag for multiprotein labeling in living cells. *Chem Biol*. 2008;15(2):128–136.
66. Maurel D, Comps-Agrar L, Brock C, Rives M-L, Bourrier E, Ayoub MA, Bazin H, Tinel N, Durroux T, Prézeau L, et al. Cell-surface protein-protein interaction analysis with time-resolved FRET and snap-tag technologies: application to GPCR oligomerization. *Nat Methods*. 2008;5(6):561–567.
67. Kern A, Albarran-Zeckler R, Walsh HE, Smith RG. Apo-ghrelin receptor forms heteromers with DRD2 in hypothalamic neurons and is essential for anorexigenic effects of DRD2 agonism. *Neuron*. 2012;73(2):317–332.
68. Brizzard B. Epitope tagging. *Biotechniques*. 2008;44(5):693–695.
69. Zhao N, Kamijo K, Fox PD, Oda H, Morisaki T, Sato Y, Kimura H, Stasevich TJ. A genetically encoded probe for imaging nascent and mature HA-tagged proteins in vivo. *Nat Commun*. 2019;10(1):2947.
70. Götzke H, Kilisch M, Martínez-Carranza M, Sograte-Idrissi S, Rajavel A, Schlichthaerle T, Engels N, Jungmann R, Stenmark P, Opazo F, et al. The ALFA-tag is a highly versatile tool for nanobody-based bioscience applications. *Nat Commun*. 2019;10(1):4403.
71. Howarth M, Ting AY. Imaging proteins in live mammalian cells with biotin ligase and monovalent streptavidin. *Nat Protoc*. 2008;3(3):534–545.
72. Lang K, Chin JW. Bioorthogonal reactions for labeling proteins. *ACS Chem Biol*. 2014;9(1):16–20.
73. Liu CC, Schultz PG. Adding new chemistries to the genetic code. *Annu Rev Biochem*. 2010;79:413–444.
74. Nikić I, Kang JH, Girona GE, Aramburu IV, Lemke EA. Labeling proteins on live mammalian cells using click chemistry. *Nat Protoc*. 2015;10(5):780–791.
75. Neubert F, Beliu G, Terpitz U, Werner C, Geis C, Sauer M, Doose S. Bioorthogonal Click Chemistry Enables Site-specific Fluorescence Labeling of Functional NMDA Receptors for Super-Resolution Imaging. *Angew Chem Int Ed Engl*. 2018;57(50):16364–16369.
76. Ernst RJ, Krogager TP, Maywood ES, Zanchi R, Beránek V, Elliott TS, Barry NP, Hastings MH, Chin JW. Genetic code expansion in the mouse brain. *Nat Chem Biol*. 2016;12(10):776–778.
77. Levinson JN, El-Husseini A. Building excitatory and inhibitory synapses: balancing neuroligin partnerships. *Neuron*. 2005;48(2):171–174.
78. Rouach N, Byrd K, Petralia RS, Elias GM, Adesnik H, Tomita S, Karimzadegan S, Kealey C, Brecht DS, Nicoll RA. TARP gamma-8 controls hippocampal AMPA receptor number, distribution and synaptic plasticity. *Nat Neurosci*. 2005;8(11):1525–1533.
79. Shaikh SA, Dolino DM, Lee G, Chatterjee S, MacLean DM, Flatebo C, Landes CF, Jayaraman V. Stargazin Modulation of AMPA Receptors. *Cell Rep*. 2016;17(2):328–335.
80. Henley JM, Wilkinson KA. Synaptic AMPA receptor composition in development, plasticity and disease. *Nat Rev Neurosci*. 2016;17(6):337–350.
81. Lu W, Shi Y, Jackson AC, Bjorgan K, During MJ, Sprengel R, Seeburg PH, Nicoll RA. Subunit composition of synaptic AMPA receptors revealed by a single-cell genetic approach. *Neuron*. 2009;62(2):254–268.
82. Shi S-H, Hayashi Y, Esteban JA, Malinow R. Subunit-Specific Rules Governing AMPA Receptor Trafficking to Synapses in Hippocampal Pyramidal Neurons. *Cell*. 2001;105(3):331–343.
83. Zhu JJ, Esteban JA, Hayashi Y, Malinow R. Postnatal synaptic potentiation: delivery of GluR4-containing AMPA receptors by spontaneous activity. *Nat Neurosci*. 2000;3(11):1098–1106.
84. Choquet D. Linking Nanoscale Dynamics of AMPA Receptor Organization to Plasticity of Excitatory Synapses and Learning. *J Neurosci*. 2018;38(44):9318–9329.
85. Anggono V, Huganir RL. Regulation of AMPA receptor trafficking and synaptic plasticity. *Curr Opin Neurobiol*. 2012;22(3):461–469.

86. Shepherd JD, Huganir RL. The cell biology of synaptic plasticity: AMPA receptor trafficking. *Annu Rev Cell Dev Biol.* 2007;23:613–643.
87. Zamanillo D, Sprengel R, Hvalby O, Jensen V, Burnashev N, Rozov A, Kaiser KM, Köster HJ, Borchardt T, Worley P, et al. Importance of AMPA receptors for hippocampal synaptic plasticity but not for spatial learning. *Science.* 1999;284(5421):1805–1811.
88. Hayashi Y, Shi SH, Esteban JA, Piccini A, Poncer JC, Malinow R. Driving AMPA receptors into synapses by LTP and CaMKII: requirement for GluR1 and PDZ domain interaction. *Science.* 2000;287(5461):2262–2267.
89. Granger AJ, Nicoll RA. LTD expression is independent of glutamate receptor subtype. *Front Synaptic Neurosci.* 2014;6:15.
90. Granger AJ, Shi Y, Lu W, Cerpas M, Nicoll RA. LTP requires a reserve pool of glutamate receptors independent of subunit type. *Nature.* 2013;493(7433):495–500.
91. MacGillavry HD, Song Y, Raghavachari S, Blanpied TA. Nanoscale scaffolding domains within the postsynaptic density concentrate synaptic AMPA receptors. *Neuron.* 2013;78(4):615–622.
92. Araki Y, Zeng M, Zhang M, Huganir RL. Rapid dispersion of SynGAP from synaptic spines triggers AMPA receptor insertion and spine enlargement during LTP. *Neuron.* 2015;85(1):173–189.
93. Walkup WG, Mastro TL, Schenker LT, Vielmetter J, Hu R, Iancu A, Reghunathan M, Bannon BD, Kennedy MB. Correction: A model for regulation by SynGAP- α 1 of binding of synaptic proteins to PDZ-domain 'Slots' in the postsynaptic density. *Elife.* 2016;5.
94. Choquet D, Hosy E. AMPA receptor nanoscale dynamic organization and synaptic plasticities. *Curr Opin Neurobiol.* 2020;63:137–145.
95. Schwenk J, Harmel N, Brechet A, Zolles G, Berkefeld H, Müller CS, Bildl W, Baehrens D, Hüber B, Kulik A, et al. High-resolution proteomics unravel architecture and molecular diversity of native AMPA receptor complexes. *Neuron.* 2012;74(4):621–633.
96. Sheng M, Hoogenraad CC. The postsynaptic architecture of excitatory synapses: a more quantitative view. *Annu Rev Biochem.* 2007;76:823–847.
97. Pandya NJ, Seeger C, Babai N, Gonzalez-Lozano MA, Mack V, Lodder JC, Gouwenberg Y, Mansvelter HD, Danielson UH, Li KW, et al. Noelin1 Affects Lateral Mobility of Synaptic AMPA Receptors. *Cell Rep.* 2018;24(5):1218–1230.
98. Penn AC, Zhang CL, Georges F, Royer L, Breillat C, Hosy E, Petersen JD, Humeau Y, Choquet D. Hippocampal LTP and contextual learning require surface diffusion of AMPA receptors. *Nature.* 2017;549(7672):384–388.
99. Wu D, Bacaj T, Morishita W, Goswami D, Arendt KL, Xu W, Chen L, Malenka RC, Südhof TC. Postsynaptic synaptotagmins mediate AMPA receptor exocytosis during LTP. *Nature.* 2017;544(7650):316–321.
100. Awasthi A, Ramachandran B, Ahmed S, Benito E, Shinoda Y, Nitzan N, Heukamp A, Rannio S, Martens H, Barth J, et al. Synaptotagmin-3 drives AMPA receptor endocytosis, depression of synapse strength, and forgetting. *Science.* 2019;363(6422).
101. Wagner W, Lippmann K, Heisler FF, Gromova KV, Lombino FL, Roesler MK, Pechmann Y, Hornig S, Schweizer M, Polo S, et al. Myosin VI Drives Clathrin-Mediated AMPA Receptor Endocytosis to Facilitate Cerebellar Long-Term Depression. *Cell Rep.* 2019;28(1):11-20.e9.
102. Rosendale M, Jullié D, Choquet D, Perrais D. Spatial and Temporal Regulation of Receptor Endocytosis in Neuronal Dendrites Revealed by Imaging of Single Vesicle Formation. *Cell Rep.* 2017;18(8):1840–1847.
103. Raghavachari S, Lisman JE. Properties of quantal transmission at CA1 synapses. *J Neurophysiol.* 2004;92(4):2456–2467.
104. Helassa N, Dürst CD, Coates C, Kerruth S, Arif U, Schulze C, Wiegert JS, Geeves M, Oertner TG, Török K. Ultrafast glutamate sensors resolve high-frequency release at Schaffer collateral synapses. *Proc Natl Acad Sci U S A.* 2018;115(21):5594–5599.

105. Zeng M, Shang Y, Araki Y, Guo T, Hugarir RL, Zhang M. Phase Transition in Postsynaptic Densities Underlies Formation of Synaptic Complexes and Synaptic Plasticity. *Cell*. 2016;166(5):1163-1175.e12.
106. Zeng M, Díaz-Alonso J, Ye F, Chen X, Xu J, Ji Z, Nicoll RA, Zhang M. Phase Separation-Mediated TARP/MAGUK Complex Condensation and AMPA Receptor Synaptic Transmission. *Neuron*. 2019;104(3):529-543.e6.
107. Tang A-H, Chen H, Li TP, Metzbower SR, MacGillavry HD, Blanpied TA. A trans-synaptic nanocolumn aligns neurotransmitter release to receptors. *Nature*. 2016;536(7615):210-214.
108. Reddy-Alla S, Böhme MA, Reynolds E, Beis C, Grasskamp AT, Mampell MM, Maglione M, Jusyte M, Rey U, Babikir H, et al. Stable Positioning of Unc13 Restricts Synaptic Vesicle Fusion to Defined Release Sites to Promote Synchronous Neurotransmission. *Neuron*. 2017;95(6):1350-1364.e12.
109. Südhof TC. Towards an Understanding of Synapse Formation. *Neuron*. 2018;100(2):276-293.
110. Mondin M, Labrousse V, Hosy E, Heine M, Tessier B, Levet F, Poujol C, Blanchet C, Choquet D, Thoumine O. Neurexin-neuroigin adhesions capture surface-diffusing AMPA receptors through PSD-95 scaffolds. *J Neurosci*. 2011;31(38):13500-13515.
111. Haas KT, Compans B, Letellier M, Bartol TM, Grillo-Bosch D, Sejnowski TJ, Sainlos M, Choquet D, Thoumine O, Hosy E. Pre-post synaptic alignment through neuroigin-1 tunes synaptic transmission efficiency. *Elife*. 2018;7.
112. Chen L, Chetkovich DM, Petralia RS, Sweeney NT, Kawasaki Y, Wenthold RJ, Brecht DS, Nicoll RA. Stargazin regulates synaptic targeting of AMPA receptors by two distinct mechanisms. *Nature*. 2000;408(6815):936-943.
113. Kato AS, Siuda ER, Nisenbaum ES, Brecht DS. AMPA receptor subunit-specific regulation by a distinct family of type II TARPs. *Neuron*. 2008;59(6):986-996.
114. Tomita S, Adesnik H, Sekiguchi M, Zhang W, Wada K, Howe JR, Nicoll RA, Brecht DS. Stargazin modulates AMPA receptor gating and trafficking by distinct domains. *Nature*. 2005;435(7045):1052-1058.
115. Schwenk J, Baehrens D, Haupt A, Bildl W, Boudkazi S, Roeper J, Fakler B, Schulte U. Regional diversity and developmental dynamics of the AMPA-receptor proteome in the mammalian brain. *Neuron*. 2014;84(1):41-54.
116. Zhao Y, Chen S, Yoshioka C, Bacongus I, Gouaux E. Architecture of fully occupied GluA2 AMPA receptor-TARP complex elucidated by cryo-EM. *Nature*. 2016;536(7614):108-111.
117. Twomey EC, Yelshanskaya MV, Sobolevsky AI. Structural and functional insights into transmembrane AMPA receptor regulatory protein complexes. *J Gen Physiol*. 2019;151(12):1347-1356.
118. Herguedas B, Watson JF, Ho H, Cais O, García-Nafria J, Greger IH. Architecture of the heteromeric GluA1/2 AMPA receptor in complex with the auxiliary subunit TARP γ 8. *Science*. 2019;364(6438).
119. Kamalova A, Nakagawa T. AMPA receptor structure and auxiliary subunits. *J Physiol*. 2021;599(2):453-469.
120. Chen S, Gouaux E. Structure and mechanism of AMPA receptor - auxiliary protein complexes. *Curr Opin Struct Biol*. 2019;54:104-111.
121. Dawe GB, Kadir MF, Venskutonytė R, Perozzo AM, Yan Y, Alexander RPD, Navarrete C, Santander EA, Arsénault M, Fuentes C, et al. Nanoscale Mobility of the Apo State and TARP Stoichiometry Dictate the Gating Behavior of Alternatively Spliced AMPA Receptors. *Neuron*. 2019;102(5):976-992.e5.
122. Shi Y, Lu W, Milstein AD, Nicoll RA. The stoichiometry of AMPA receptors and TARPs varies by neuronal cell type. *Neuron*. 2009;62(5):633-640.
123. Twomey EC, Yelshanskaya MV, Grassucci RA, Frank J, Sobolevsky AI. Channel opening and gating mechanism in AMPA-subtype glutamate receptors. *Nature*. 2017;549(7670):60-65.

124. Chen S, Zhao Y, Wang Y, Shekhar M, Tajkhorshid E, Gouaux E. Activation and Desensitization Mechanism of AMPA Receptor-TARP Complex by Cryo-EM. *Cell*. 2017;170(6):1234-1246.e14.
125. Dawe GB, Musgaard M, Arousseau MRP, Nayeem N, Green T, Biggin PC, Bowie D. Distinct Structural Pathways Coordinate the Activation of AMPA Receptor-Auxiliary Subunit Complexes. *Neuron*. 2016;89(6):1264-1276.
126. Hawken NM, Zaika EI, Nakagawa T. Engineering defined membrane-embedded elements of AMPA receptor induces opposing gating modulation by cornichon 3 and stargazin. *J Physiol*. 2017;595(20):6517-6539.
127. Sheng N, Bemben MA, Díaz-Alonso J, Tao W, Shi YS, Nicoll RA. LTP requires postsynaptic PDZ-domain interactions with glutamate receptor/auxiliary protein complexes. *Proc Natl Acad Sci U S A*. 2018;115(15):3948-3953.
128. Sumioka A, Brown TE, Kato AS, Brecht DS, Kauer JA, Tomita S. PDZ binding of TARP γ -8 controls synaptic transmission but not synaptic plasticity. *Nat Neurosci*. 2011;14(11):1410-1412.
129. Hamdan FF, Gauthier J, Araki Y, Lin D-T, Yoshizawa Y, Higashi K, Park A-R, Spiegelman D, Dobrzyniecka S, Piton A, et al. Excess of de novo deleterious mutations in genes associated with glutamatergic systems in nonsyndromic intellectual disability. *Am J Hum Genet*. 2011;88(3):306-316.
130. Lee MR, Gardinier KM, Gernert DL, Schober DA, Wright RA, Wang H, Qian Y, Witkin JM, Nisenbaum ES, Kato AS. Structural Determinants of the γ -8 TARP Dependent AMPA Receptor Antagonist. *ACS Chem Neurosci*. 2017;8(12):2631-2647.
131. Kato AS, Burris KD, Gardinier KM, Gernert DL, Porter WJ, Reel J, Ding C, Tu Y, Schober DA, Lee MR, et al. Forebrain-selective AMPA-receptor antagonism guided by TARP γ -8 as an antiepileptic mechanism. *Nat Med*. 2016;22(12):1496-1501.
132. Gardinier KM, Gernert DL, Porter WJ, Reel JK, Ornstein PL, Spinazze P, Stevens FC, Hahn P, Hollinshead SP, Mayhugh D, et al. Discovery of the First α -Amino-3-hydroxy-5-methyl-4-isoxazolepropionic Acid (AMPA) Receptor Antagonist Dependent upon Transmembrane AMPA Receptor Regulatory Protein (TARP) γ -8. *J Med Chem*. 2016;59(10):4753-4768.
133. Evans AJ, Gurung S, Henley JM, Nakamura Y, Wilkinson KA. Exciting Times: New Advances Towards Understanding the Regulation and Roles of Kainate Receptors. *Neurochem Res*. 2019;44(3):572-584.
134. Carta M, Fièvre S, Gorlewicz A, Mulle C. Kainate receptors in the hippocampus. *Eur J Neurosci*. 2014;39(11):1835-1844.
135. Sihra TS, Flores G, Rodríguez-Moreno A. Kainate receptors: multiple roles in neuronal plasticity. *Neuroscientist*. 2014;20(1):29-43.
136. Sihra TS, Rodríguez-Moreno A. Presynaptic kainate receptor-mediated bidirectional modulatory actions: mechanisms. *Neurochem Int*. 2013;62(7):982-987.
137. Werner P, Voigt M, Keinänen K, Wisden W, Seeburg PH. Cloning of a putative high-affinity kainate receptor expressed predominantly in hippocampal CA3 cells. *Nature*. 1991;351(6329):742-744.
138. Herb A, Burnashev N, Werner P, Sakmann B, Wisden W, Seeburg PH. The KA-2 subunit of excitatory amino acid receptors shows widespread expression in brain and forms ion channels with distantly related subunits. *Neuron*. 1992;8(4):775-785.
139. Fièvre S, Carta M, Chamma I, Labrousse V, Thoumine O, Mulle C. Molecular determinants for the strictly compartmentalized expression of kainate receptors in CA3 pyramidal cells. *Nat Commun*. 2016;7(1):12738.
140. Coussen F, Normand E, Marchal C, Costet P, Choquet D, Lambert M, Mège R-M, Mulle C. Recruitment of the Kainate Receptor Subunit Glutamate Receptor 6 by Cadherin/Catenin Complexes. *J Neurosci*. 2002;22(15):6426-6436.
141. Hirbec H, Francis JC, Lauri SE, Braithwaite SP, Coussen F, Mulle C, Dev KK, Couthino V, Meyer G, Isaac JT, et al. Rapid and Differential Regulation of AMPA and Kainate Receptors at Hippocampal Mossy Fibre Synapses by PICK1 and GRIP. *Neuron*. 2003;37(4):625-638.

142. Suzuki E, Kamiya H. PSD-95 regulates synaptic kainate receptors at mouse hippocampal mossy fiber-CA3 synapses. *Neurosci Res.* 2016;107:14–19.
143. Matsuda K, Budisantoso T, Mitakidis N, Sugaya Y, Miura E, Kakegawa W, Yamasaki M, Konno K, Uchigashima M, Abe M, et al. Transsynaptic Modulation of Kainate Receptor Functions by C1q-like Proteins. *Neuron.* 2016;90(4):752–767.
144. Matsuda K. Synapse organization and modulation via C1q family proteins and their receptors in the central nervous system. *Neurosci Res.* 2017;116:46–53.
145. Lerma J. Roles and rules of kainate receptors in synaptic transmission. *Nat Rev Neurosci.* 2003;4(6):481–495.
146. Frerking M, Schmitz D, Zhou Q, Johansen J, Nicoll RA. Kainate Receptors Depress Excitatory Synaptic Transmission at CA3→CA1 Synapses in the Hippocampus via a Direct Presynaptic Action. *J Neurosci.* 2001;21(9):2958–2966.
147. Andrade-Talavera Y, Duque-Feria P, Sihra TS, Rodríguez-Moreno A. Pre-synaptic kainate receptor-mediated facilitation of glutamate release involves PKA and Ca(2+) -calmodulin at thalamocortical synapses. *J Neurochem.* 2013;126(5):565–578.
148. Chamberlain SEL, González-González IM, Wilkinson KA, Konopacki FA, Kantamneni S, Henley JM, Mellor JR. SUMOylation and phosphorylation of GluK2 regulate kainate receptor trafficking and synaptic plasticity. *Nat Neurosci.* 2012;15(6):845–852.
149. González-González IM, Henley JM. Postsynaptic kainate receptor recycling and surface expression are regulated by metabotropic autoreceptor signalling. *Traffic.* 2013;14(7):810–822.
150. Martin S, Bouschet T, Jenkins EL, Nishimune A, Henley JM. Bidirectional regulation of kainate receptor surface expression in hippocampal neurons. *J Biol Chem.* 2008;283(52):36435–36440.
151. Petrovic MM, Da Viana Silva S, Clement JP, Vyklicky L, Mulle C, González-González IM, Henley JM. Metabotropic action of postsynaptic kainate receptors triggers hippocampal long-term potentiation. *Nat Neurosci.* 2017;20(4):529–539.
152. Rodríguez-Moreno A, Lerma J. Kainate Receptor Modulation of GABA Release Involves a Metabotropic Function. *Neuron.* 1998;20(6):1211–1218.
153. Jiang L, Kang D, Kang J. Potentiation of tonic GABAergic inhibition by activation of postsynaptic kainate receptors. *Neuroscience.* 2015;298:448–454.
154. Crépel V, Mulle C. Physiopathology of kainate receptors in epilepsy. *Current Opinion in Pharmacology.* 2015;20:83–88.
155. Griswold AJ, Ma D, Cukier HN, Nations LD, Schmidt MA, Chung R-H, Jaworski JM, Salyakina D, Konidari I, Whitehead PL, et al. Evaluation of copy number variations reveals novel candidate genes in autism spectrum disorder-associated pathways. *Hum Mol Genet.* 2012;21(15):3513–3523.
156. Milanese E, Bonvicini C, Congiu C, Bortolomasi M, Gainelli G, Gennarelli M, Minelli A. The role of GRIK4 gene in treatment-resistant depression. *Genet Res (Camb).* 2015;97:e14.
157. Pickard BS, Malloy MP, Christoforou A, Thomson PA, Evans KL, Morris SW, Hampson M, Porteous DJ, Blackwood DHR, Muir WJ. Cytogenetic and genetic evidence supports a role for the kainate-type glutamate receptor gene, GRIK4, in schizophrenia and bipolar disorder. *Mol Psychiatry.* 2006;11(9):847–857.
158. Matute C. Therapeutic potential of kainate receptors. *CNS Neurosci Ther.* 2011;17(6):661–669.
159. Fritschy J-M, Panzanelli P. GABAA receptors and plasticity of inhibitory neurotransmission in the central nervous system. *Eur J Neurosci.* 2014;39(11):1845–1865.
160. Belelli D, Harrison NL, Maguire J, Macdonald RL, Walker MC, Cope DW. Extrasynaptic GABAA receptors: form, pharmacology, and function. *J Neurosci.* 2009;29(41):12757–12763.
161. Brickley SG, Mody I. Extrasynaptic GABA(A) receptors: their function in the CNS and implications for disease. *Neuron.* 2012;73(1):23–34.
162. Fritschy J-M, Panzanelli P, Tyagarajan SK. Molecular and functional heterogeneity of GABAergic synapses. *Cell Mol Life Sci.* 2012;69(15):2485–2499.
163. Tretter V, Mukherjee J, Maric H-M, Schindelin H, Sieghart W, Moss SJ. Gephyrin, the enigmatic organizer at GABAergic synapses. *Front Cell Neurosci.* 2012;6:23.

164. Tretter V, Jacob TC, Mukherjee J, Fritschy J-M, Pangalos MN, Moss SJ. The clustering of GABA(A) receptor subtypes at inhibitory synapses is facilitated via the direct binding of receptor alpha 2 subunits to gephyrin. *J Neurosci*. 2008;28(6):1356–1365.
165. Mukherjee J, Kretschmannova K, Gouzer G, Maric H-M, Ramsden S, Tretter V, Harvey K, Davies PA, Triller A, Schindelin H, et al. The residence time of GABA(A)Rs at inhibitory synapses is determined by direct binding of the receptor $\alpha 1$ subunit to gephyrin. *J Neurosci*. 2011;31(41):14677–14687.
166. Maric H-M, Mukherjee J, Tretter V, Moss SJ, Schindelin H. Gephyrin-mediated γ -aminobutyric acid type A and glycine receptor clustering relies on a common binding site. *J Biol Chem*. 2011;286(49):42105–42114.
167. Kowalczyk S, Winkelmann A, Smolinsky B, Förstera B, Neundorf I, Schwarz G, Meier JC. Direct binding of GABAA receptor $\beta 2$ and $\beta 3$ subunits to gephyrin. *Eur J Neurosci*. 2013;37(4):544–554.
168. Sander B, Tria G, Shkumatov AV, Kim E-Y, Grossmann JG, Tessmer I, Svergun DI, Schindelin H. Structural characterization of gephyrin by AFM and SAXS reveals a mixture of compact and extended states. *Acta Crystallogr D Biol Crystallogr*. 2013;69(Pt 10):2050–2060.
169. Tyagarajan SK, Fritschy J-M. Gephyrin: a master regulator of neuronal function? *Nat Rev Neurosci*. 2014;15(3):141–156.
170. Mayer S, Kumar R, Jaiswal M, Soykan T, Ahmadian MR, Brose N, Betz H, Rhee J-S, Papadopoulos T. Collybistin activation by GTP-TC10 enhances postsynaptic gephyrin clustering and hippocampal GABAergic neurotransmission. *Proc Natl Acad Sci U S A*. 2013;110(51):20795–20800.
171. Papadopoulos T, Eulenburg V, Reddy-Alla S, Mansuy IM, Li Y, Betz H. Collybistin is required for both the formation and maintenance of GABAergic postsynapses in the hippocampus. *Mol Cell Neurosci*. 2008;39(2):161–169.
172. Papadopoulos T, Korte M, Eulenburg V, Kubota H, Retiounskaia M, Harvey RJ, Harvey K, O'Sullivan GA, Laube B, Hülsmann S, et al. Impaired GABAergic transmission and altered hippocampal synaptic plasticity in collybistin-deficient mice. *EMBO J*. 2007;26(17):3888–3899.
173. Bogdanov Y, Michels G, Armstrong-Gold C, Haydon PG, Lindstrom J, Pangalos M, Moss SJ. Synaptic GABAA receptors are directly recruited from their extrasynaptic counterparts. *EMBO J*. 2006;25(18):4381–4389.
174. Houston CM, He Q, Smart TG. CaMKII phosphorylation of the GABA(A) receptor: receptor subtype- and synapse-specific modulation. *J Physiol*. 2009;587(Pt 10):2115–2125.
175. Vithlani M, Terunuma M, Moss SJ. The dynamic modulation of GABA(A) receptor trafficking and its role in regulating the plasticity of inhibitory synapses. *Physiol Rev*. 2011;91(3):1009–1022.
176. Connelly WM, Fyson SJ, Errington AC, McCafferty CP, Cope DW, Di Giovanni G, Crunelli V. GABAB Receptors Regulate Extrasynaptic GABAA Receptors. *J Neurosci*. 2013;33(9):3780–3785.
177. Tao W, Higgs MH, Spain WJ, Ransom CB. Postsynaptic GABAB receptors enhance extrasynaptic GABAA receptor function in dentate gyrus granule cells. *J Neurosci*. 2013;33(9):3738–3743.
178. Connelly WM, Errington AC, Di Giovanni G, Crunelli V. Metabotropic regulation of extrasynaptic GABAA receptors. *Front Neural Circuits*. 2013;7:171.
179. Abramian AM, Comenencia-Ortiz E, Vithlani M, Tretter EV, Sieghart W, Davies PA, Moss SJ. Protein kinase C phosphorylation regulates membrane insertion of GABAA receptor subtypes that mediate tonic inhibition. *J Biol Chem*. 2010;285(53):41795–41805.
180. Dieni CV, Chancey JH, Overstreet-Wadiche LS. Dynamic functions of GABA signaling during granule cell maturation. *Front Neural Circuits*. 2012;6:113.
181. Platel J-C, Lacar B, Bordey A. GABA and glutamate signaling: homeostatic control of adult forebrain neurogenesis. *J Mol Histol*. 2007;38(6):602–610.
182. Galanopoulou AS. Mutations affecting GABAergic signaling in seizures and epilepsy. *Pflugers Arch*. 2010;460(2):505–523.
183. Lewis DA, Hashimoto T, Volk DW. Cortical inhibitory neurons and schizophrenia. *Nat Rev Neurosci*. 2005;6(4):312–324.

-
184. Pizzarelli R, Cherubini E. Alterations of GABAergic signaling in autism spectrum disorders. *Neural Plast.* 2011;2011:297153.
185. Vithlani M, Hines RM, Zhong P, Terunuma M, Hines DJ, Revilla-Sanchez R, Jurd R, Haydon P, Rios M, Brandon N, et al. The ability of BDNF to modify neurogenesis and depressive-like behaviors is dependent upon phosphorylation of tyrosine residues 365/367 in the GABA(A)-receptor $\gamma 2$ subunit. *J Neurosci.* 2013;33(39):15567–15577.
186. Bouthour W, Leroy F, Emmanuelli C, Carnaud M, Dahan M, Poncer JC, Lévi S. A human mutation in Gabrg2 associated with generalized epilepsy alters the membrane dynamics of GABA receptors. *Cereb Cortex.* 2012;22(7):1542–1553.
187. Bembem MA, Shipman SL, Nicoll RA, Roche KW. The cellular and molecular landscape of neuroligins. *Trends Neurosci.* 2015;38(8):496–505.
188. Craig AM, Kang Y. Neurexin-neuroligin signaling in synapse development. *Curr Opin Neurobiol.* 2007;17(1):43–52.
189. Krueger DD, Tuffly LP, Papadopoulos T, Brose N. The role of neurexins and neuroligins in the formation, maturation, and function of vertebrate synapses. *Curr Opin Neurobiol.* 2012;22(3):412–422.
190. Graf ER, Zhang X, Jin S-X, Linhoff MW, Craig AM. Neurexins induce differentiation of GABA and glutamate postsynaptic specializations via neuroligins. *Cell.* 2004;119(7):1013–1026.
191. Chih B, Engelman H, Scheiffele P. Control of excitatory and inhibitory synapse formation by neuroligins. *Science.* 2005;307(5713):1324–1328.
192. Varoqueaux F, Jamain S, Brose N. Neuroligin 2 is exclusively localized to inhibitory synapses. *Eur J Cell Biol.* 2004;83(9):449–456.
193. Ichtchenko K, Nguyen T, Südhof TC. Structures, alternative splicing, and neurexin binding of multiple neuroligins. *J Biol Chem.* 1996;271(5):2676–2682.
194. Ali H, Marth L, Krueger-Burg D. Neuroligin-2 as a central organizer of inhibitory synapses in health and disease. *Sci. Signal.* 2020;13(663):eabd8379.
195. Pouloupoulos A, Aramuni G, Meyer G, Soykan T, Hoon M, Papadopoulos T, Zhang M, Paarmann I, Fuchs C, Harvey K, et al. Neuroligin 2 drives postsynaptic assembly at perisomatic inhibitory synapses through gephyrin and collybistin. *Neuron.* 2009;63(5):628–642.
196. Papadopoulos T, Soykan T. The role of collybistin in gephyrin clustering at inhibitory synapses: facts and open questions. *Front Cell Neurosci.* 2011;5:11.
197. Sumita K, Sato Y, Iida J, Kawata A, Hamano M, Hirabayashi S, Ohno K, Peles E, Hata Y. Synaptic scaffolding molecule (S-SCAM) membrane-associated guanylate kinase with inverted organization (MAGI)-2 is associated with cell adhesion molecules at inhibitory synapses in rat hippocampal neurons. *J Neurochem.* 2007;100(1):154–166.
198. Chubykin AA, Atasoy D, Etherton MR, Brose N, Kavalali ET, Gibson JR, Südhof TC. Activity-dependent validation of excitatory versus inhibitory synapses by neuroligin-1 versus neuroligin-2. *Neuron.* 2007;54(6):919–931.
199. Hines RM, Wu L, Hines DJ, Steenland H, Mansour S, Dahlhaus R, Singaraja RR, Cao X, Sammler E, Hormuzdi SG, et al. Synaptic imbalance, stereotypies, and impaired social interactions in mice with altered neuroligin 2 expression. *J Neurosci.* 2008;28(24):6055–6067.
200. Sun C, Cheng M-C, Qin R, Liao D-L, Chen T-T, Koong F-J, Chen G, Chen C-H. Identification and functional characterization of rare mutations of the neuroligin-2 gene (NLGN2) associated with schizophrenia. *Hum Mol Genet.* 2011;20(15):3042–3051.
201. Parente DJ, Garriga C, Baskin B, Douglas G, Cho MT, Araujo GC, Shinawi M. Neuroligin 2 nonsense variant associated with anxiety, autism, intellectual disability, hyperphagia, and obesity. *Am J Med Genet A.* 2017;173(1):213–216.
202. Heshmati M, Aleyasin H, Menard C, Christoffel DJ, Flanigan ME, Pfau ML, Hodes GE, Lepack AE, Bicks LK, Takahashi A, et al. Cell-type-specific role for nucleus accumbens neuroligin-2 in depression and stress susceptibility. *Proc Natl Acad Sci U S A.* 2018;115(5):1111–1116.

203. Kathuria A, Lopez-Lengowski K, Watmuff B, McPhie D, Cohen BM, Karmacharya R. Synaptic deficits in iPSC-derived cortical interneurons in schizophrenia are mediated by NLGN2 and rescued by N-acetylcysteine. *Transl Psychiatry*. 2019;9(1):321.
204. SHIMOMURA O, JOHNSON FH, SAIGA Y. Extraction, purification and properties of aequorin, a bioluminescent protein from the luminous hydromedusan, *Aequorea*. *J Cell Comp Physiol*. 1962;59:223–239.
205. Heim R, Prasher DC, Tsien RY. Wavelength mutations and posttranslational autoxidation of green fluorescent protein. *Proc Natl Acad Sci U S A*. 1994;91(26):12501–12504.
206. Lippincott-Schwartz J, Snapp E, Kenworthy A. Studying protein dynamics in living cells. *Nat Rev Mol Cell Biol*. 2001;2(6):444–456.
207. Jung S, Aliberti J, Graemmel P, Sunshine MJ, Kreutzberg GW, Sher A, Littman DR. Analysis of fractalkine receptor CX(3)CR1 function by targeted deletion and green fluorescent protein reporter gene insertion. *Mol Cell Biol*. 2000;20(11):4106–4114.
208. Zimmer M. Green fluorescent protein (GFP): applications, structure, and related photophysical behavior. *Chem Rev*. 2002;102(3):759–781.
209. Day RN, Davidson MW. The fluorescent protein palette: tools for cellular imaging. *Chem Soc Rev*. 2009;38(10):2887–2921.
210. Sankaranarayanan S, Angelis D de, Rothman JE, Ryan TA. The Use of pHluorins for Optical Measurements of Presynaptic Activity. *Biophys J*. 2000;79(4):2199–2208.
211. Patterson GH, Lippincott-Schwartz J. A photoactivatable GFP for selective photolabeling of proteins and cells. *Science*. 2002;297(5588):1873–1877.
212. Betzig E, Patterson GH, Sougrat R, Lindwasser OW, Olenych S, Bonifacino JS, Davidson MW, Lippincott-Schwartz J, Hess HF. Imaging intracellular fluorescent proteins at nanometer resolution. *Science*. 2006;313(5793):1642–1645.
213. Gust A, Zander A, Gietl A, Holzmeister P, Schulz S, Lalkens B, Tinnefeld P, Grohmann D. A starting point for fluorescence-based single-molecule measurements in biomolecular research. *Molecules*. 2014;19(10):15824–15865.
214. Lavis LD, Raines RT. Bright ideas for chemical biology. *ACS Chem Biol*. 2008;3(3):142–155.
215. Baeyer A. Ueber eine neue Klasse von Farbstoffen. *Ber. Dtsch. Chem. Ges*. 1871;4(2):555–558.
216. Graber ML, DiLillo DC, Friedman BL, Pastoriza-Munoz E. Characteristics of fluoroprobes for measuring intracellular pH. *Analytical Biochemistry*. 1986;156(1):202–212.
217. Minta A, Kao JPY, Tsien RY. Fluorescent indicators for cytosolic calcium based on rhodamine and fluorescein chromophores. *Journal of Biological Chemistry*. 1989;264(14):8171–8178.
218. Martin VV, Rothe A, Gee KR. Fluorescent metal ion indicators based on benzoannelated crown systems: a green fluorescent indicator for intracellular sodium ions. *Bioorganic & Medicinal Chemistry Letters*. 2005;15(7):1851–1855.
219. Koide Y, Urano Y, Kenmoku S, Kojima H, Nagano T. Design and synthesis of fluorescent probes for selective detection of highly reactive oxygen species in mitochondria of living cells. *J Am Chem Soc*. 2007;129(34):10324–10325.
220. Uno S, Kamiya M, Yoshihara T, Sugawara K, Okabe K, Tarhan MC, Fujita H, Funatsu T, Okada Y, Tobita S, et al. A spontaneously blinking fluorophore based on intramolecular spirocyclization for live-cell super-resolution imaging. *Nature Chem*. 2014;6(8):681–689.
221. Larsen TA, Goodsell DS, Cascio D, Grzeskowiak K, Dickerson RE. The structure of DAPI bound to DNA. *J Biomol Struct Dyn*. 1989;7(3):477–491.
222. Petit J-M, Denis-Gay M, Ratinaud M-H. Assessment of fluorochromes for cellular structure and function studies by flow cytometry. *Biology of the Cell*. 1993;78(1-2):1–13.
223. Crissman HA, Hirons GT. Chapter 13 Staining of DNA in Live and Fixed Cells. In: Darzynkiewicz Z, Paul Robinson J, Crissman HA, editors. *Methods in Cell Biology: Flow Cytometry Second Edition, Part A*. Vol. 41.
224. Zimmerman M, Ashe B, Yurewicz EC, Patel G. Sensitive assays for trypsin, elastase, and chymotrypsin using new fluorogenic substrates. *Analytical Biochemistry*. 1977;78(1):47–51.

225. Babiak P, Reymond J-L. A high-throughput, low-volume enzyme assay on solid support. *Anal Chem.* 2005;77(2):373–377.
226. Schobel U, Egelhaaf HJ, Brecht A, Oelkrug D, Gauglitz G. New donor-acceptor pair for fluorescent immunoassays by energy transfer. *Bioconjug Chem.* 1999;10(6):1107–1114.
227. Heilemann M, van de Linde S, Schüttpelz M, Kasper R, Seefeldt B, Mukherjee A, Tinnefeld P, Sauer M. Subdiffraction-resolution fluorescence imaging with conventional fluorescent probes. *Angew Chem Int Ed Engl.* 2008;47(33):6172–6176.
228. van de Linde S, Löschberger A, Klein T, Heidbreder M, Wolter S, Heilemann M, Sauer M. Direct stochastic optical reconstruction microscopy with standard fluorescent probes. *Nat Protoc.* 2011;6(7):991–1009.
229. Kaplon H, Reichert JM. Antibodies to watch in 2021. *MAbs.* 2021;13(1):1860476.
230. Löschberger A, van de Linde S, Dabauvalle M-C, Rieger B, Heilemann M, Krohne G, Sauer M. Super-resolution imaging visualizes the eightfold symmetry of gp210 proteins around the nuclear pore complex and resolves the central channel with nanometer resolution. *J Cell Sci.* 2012;125(Pt 3):570–575.
231. Chiu ML, Goulet DR, Teplyakov A, Gilliland GL. *Antibody Structure and Function: The Basis for Engineering Therapeutics.* Antibodies (Basel). 2019;8(4):55.
232. Mattson G, Conklin E, Desai S, Nielander G, Savage MD, Morgensen S. A practical approach to crosslinking. *Mol Biol Rep.* 1993;17(3):167–183.
233. Lau L, Lee YL, Sahl SJ, Stearns T, Moerner WE. STED microscopy with optimized labeling density reveals 9-fold arrangement of a centriole protein. *Biophys J.* 2012;102(12):2926–2935.
234. Berg. *Stryer Biochemie.* Berlin, Heidelberg: Springer Berlin Heidelberg; 2018. ISBN: 978-3-662-54619-2.
235. Chin JW. Expanding and reprogramming the genetic code of cells and animals. *Annu Rev Biochem.* 2014;83:379–408.
236. Neumann H, Peak-Chew SY, Chin JW. Genetically encoding N(epsilon)-acetyllysine in recombinant proteins. *Nat Chem Biol.* 2008;4(4):232–234.
237. Lemke EA. The exploding genetic code. *Chembiochem.* 2014;15(12):1691–1694.
238. Chin JW, Cropp TA, Anderson JC, Mukherji M, Zhang Z, Schultz PG. An expanded eukaryotic genetic code. *Science.* 2003;301(5635):964–967.
239. Sakamoto K, Hayashi A, Sakamoto A, Kiga D, Nakayama H, Soma A, Kobayashi T, Kitabatake M, Takio K, Saito K, et al. Site-specific incorporation of an unnatural amino acid into proteins in mammalian cells. *Nucleic Acids Res.* 2002;30(21):4692–4699.
240. Xie J, Schultz PG. Adding amino acids to the genetic repertoire. *Curr Opin Chem Biol.* 2005;9(6):548–554.
241. Chen PR, Groff D, Guo J, Ou W, Cellitti S, Geierstanger BH, Schultz PG. A facile system for encoding unnatural amino acids in mammalian cells. *Angew Chem Int Ed Engl.* 2009;48(22):4052–4055.
242. Greiss S, Chin JW. Expanding the genetic code of an animal. *J Am Chem Soc.* 2011;133(36):14196–14199.
243. Mukai T, Lajoie MJ, Englert M, Söll D. Rewriting the Genetic Code. *Annu Rev Microbiol.* 2017;71:557–577.
244. Lang K, Chin JW. Cellular incorporation of unnatural amino acids and bioorthogonal labeling of proteins. *Chem Rev.* 2014;114(9):4764–4806.
245. Tsao M-L, Tian F, Schultz PG. Selective Staudinger modification of proteins containing p-azidophenylalanine. *Chembiochem.* 2005;6(12):2147–2149.
246. Prescher JA, Dube DH, Bertozzi CR. Chemical remodelling of cell surfaces in living animals. *Nature.* 2004;430(7002):873–877.
247. Hangauer MJ, Bertozzi CR. A FRET-Based Fluorogenic Phosphine for Live-Cell Imaging with the Staudinger Ligation. *Angew. Chem.* 2008;120(13):2428–2431.

248. Lin FL, Hoyt HM, van Halbeek H, Bergman RG, Bertozzi CR. Mechanistic investigation of the Staudinger ligation. *J Am Chem Soc.* 2005;127(8):2686–2695.
249. Rostovtsev VV, Green LG, Fokin VV, Sharpless KB. A Stepwise Huisgen Cycloaddition Process: Copper(I)-Catalyzed Regioselective “Ligation” of Azides and Terminal Alkynes. *Angew. Chem.* 2002;114(14):2708–2711.
250. Agard NJ, Baskin JM, Prescher JA, Lo A, Bertozzi CR. A comparative study of bioorthogonal reactions with azides. *ACS Chem Biol.* 2006;1(10):644–648.
251. Hong V, Steinmetz NF, Manchester M, Finn MG. Labeling live cells by copper-catalyzed alkyne-azide click chemistry. *Bioconjug Chem.* 2010;21(10):1912–1916.
252. Agard NJ, Prescher JA, Bertozzi CR. A strain-promoted 3 + 2 azide-alkyne cycloaddition for covalent modification of biomolecules in living systems. *J Am Chem Soc.* 2004;126(46):15046–15047.
253. Baskin JM, Prescher JA, Laughlin ST, Agard NJ, Chang PV, Miller IA, Lo A, Codelli JA, Bertozzi CR. Copper-free click chemistry for dynamic in vivo imaging. *Proc Natl Acad Sci U S A.* 2007;104(43):16793–16797.
254. Laughlin ST, Baskin JM, Amacher SL, Bertozzi CR. In vivo imaging of membrane-associated glycans in developing zebrafish. *Science.* 2008;320(5876):664–667.
255. Letschert S, Göhler A, Franke C, Bertleff-Zieschang N, Memmel E, Doose S, Seibel J, Sauer M. Super-resolution imaging of plasma membrane glycans. *Angew Chem Int Ed Engl.* 2014;53(41):10921–10924.
256. Mateos-Gil P, Letschert S, Doose S, Sauer M. Super-Resolution Imaging of Plasma Membrane Proteins with Click Chemistry. *Front Cell Dev Biol.* 2016;4:98.
257. Blackman ML, Royzen M, Fox JM. Tetrazine ligation: fast bioconjugation based on inverse-electron-demand Diels-Alder reactivity. *J Am Chem Soc.* 2008;130(41):13518–13519.
258. Lang K, Davis L, Wallace S, Mahesh M, Cox DJ, Blackman ML, Fox JM, Chin JW. Genetic Encoding of bicyclononynes and trans-cyclooctenes for site-specific protein labeling in vitro and in live mammalian cells via rapid fluorogenic Diels-Alder reactions. *J Am Chem Soc.* 2012;134(25):10317–10320.
259. Beliu G, Kurz AJ, Kuhlemann AC, Behringer-Pliess L, Meub M, Wolf N, Seibel J, Shi Z-D, Schnermann M, Grimm JB, et al. Bioorthogonal labeling with tetrazine-dyes for super-resolution microscopy. *Commun Biol.* 2019;2(1):261.
260. Devaraj NK, Hilderbrand S, Upadhyay R, Mazitschek R, Weissleder R. Bioorthogonal turn-on probes for imaging small molecules inside living cells. *Angew Chem Int Ed Engl.* 2010;49(16):2869–2872.
261. Kozma E, Estrada Girona G, Paci G, Lemke EA, Kele P. Bioorthogonal double-fluorogenic siliconrhodamine probes for intracellular super-resolution microscopy. *Chem Commun (Camb).* 2017;53(50):6696–6699.
262. Kormos A, Koehler C, Fodor EA, Rutkai ZR, Martin ME, Mező G, Lemke EA, Kele P. Bistetrazine-Cyanines as Double-Clicking Fluorogenic Two-Point Binder or Crosslinker Probes. *Chemistry.* 2018;24(35):8841–8847.
263. Plass T, Milles S, Koehler C, Szymański J, Mueller R, Wiessler M, Schultz C, Lemke EA. Amino acids for Diels-Alder reactions in living cells. *Angew Chem Int Ed Engl.* 2012;51(17):4166–4170.
264. Jabłoński A. Über den Mechanismus der Photolumineszenz von Farbstoffphosphoren. *Z. Physik.* 1935;94(1-2):38–46.
265. Brinks D, Hildner R, van Dijk EMHP, Stefani FD, Nieder JB, Hernando J, van Hulst NF. Ultrafast dynamics of single molecules. *Chem. Soc. Rev.* 2014;43(8):2476–2491.
266. Stokes G. XXX. On the change of refrangibility of light. *Phil. Trans. R. Soc.* 1852;142:463–562.
267. Jonkman J, Brown CM, Wright GD, Anderson KI, North AJ. Tutorial: guidance for quantitative confocal microscopy. *Nat Protoc.* 2020;15(5):1585–1611.
268. White JG, Amos WB. Confocal microscopy comes of age. *Nature.* 1987;328(6126):183–184.

269. Cole RW, Jinadasa T, Brown CM. Measuring and interpreting point spread functions to determine confocal microscope resolution and ensure quality control. *Nat Protoc.* 2011;6(12):1929–1941.
270. Abbe E. Beiträge zur Theorie des Mikroskops und der mikroskopischen Wahrnehmung. *Archiv f. mikrosk. Anatomie.* 1873;9(1):413–468.
271. Hell SW, Wichmann J. Breaking the diffraction resolution limit by stimulated emission: stimulated-emission-depletion fluorescence microscopy. *Opt Lett.* 1994;19(11):780–782.
272. Rust MJ, Bates M, Zhuang X. Sub-diffraction-limit imaging by stochastic optical reconstruction microscopy (STORM). *Nat Methods.* 2006;3(10):793–795.
273. van de Linde S, Aufmkolk S, Franke C, Holm T, Klein T, Löschberger A, Proppert S, Wolter S, Sauer M. Investigating cellular structures at the nanoscale with organic fluorophores. *Chem Biol.* 2013;20(1):8–18.
274. Heilemann M, van de Linde S, Mukherjee A, Sauer M. Super-resolution imaging with small organic fluorophores. *Angew Chem Int Ed Engl.* 2009;48(37):6903–6908.
275. Wolter S, Löschberger A, Holm T, Aufmkolk S, Dabauvalle M-C, van de Linde S, Sauer M. rapidSTORM: accurate, fast open-source software for localization microscopy. *Nat Methods.* 2012;9(11):1040–1041.
276. Sauer M, Heilemann M. Single-Molecule Localization Microscopy in Eukaryotes. *Chem Rev.* 2017;117(11):7478–7509.
277. Klein T, van de Linde S, Sauer M. Live-cell super-resolution imaging goes multicolor. *Chembiochem.* 2012;13(13):1861–1863.
278. Winterflood CM, Platonova E, Albrecht D, Ewers H. Dual-color 3D superresolution microscopy by combined spectral-demixing and biplane imaging. *Biophys J.* 2015;109(1):3–6.
279. Löschberger A, Franke C, Krohne G, van de Linde S, Sauer M. Correlative super-resolution fluorescence and electron microscopy of the nuclear pore complex with molecular resolution. *J Cell Sci.* 2014;127(Pt 20):4351–4355.
280. Gustafsson MG. Surpassing the lateral resolution limit by a factor of two using structured illumination microscopy. *Journal of microscopy.* 2000;198(Pt 2):82–87.
281. Hirvonen LM, Wicker K, Mandula O, Heintzmann R. Structured illumination microscopy of a living cell. *Eur Biophys J.* 2009;38(6):807–812.
282. Kner P, Chhun BB, Griffis ER, Winoto L, Gustafsson MGL. Super-resolution video microscopy of live cells by structured illumination. *Nat Methods.* 2009;6(5):339–342.
283. Gustafsson MGL, Shao L, Carlton PM, Wang CJR, Golubovskaya IN, Cande WZ, Agard DA, Sedat JW. Three-dimensional resolution doubling in wide-field fluorescence microscopy by structured illumination. *Biophys J.* 2008;94(12):4957–4970.
284. Li D, Shao L, Chen B-C, Zhang X, Zhang M, Moses B, Milkie DE, Beach JR, Hammer JA, Pasham M, et al. ADVANCED IMAGING. Extended-resolution structured illumination imaging of endocytic and cytoskeletal dynamics. *Science.* 2015;349(6251):aab3500.
285. Nixon-Abell J, Obara CJ, Weigel AV, Li D, Legant WR, Xu CS, Pasolli HA, Harvey K, Hess HF, Betzig E, et al. Increased spatiotemporal resolution reveals highly dynamic dense tubular matrices in the peripheral ER. *Science.* 2016;354(6311).
286. Schermelleh L, Carlton PM, Haase S, Shao L, Winoto L, Kner P, Burke B, Cardoso MC, Agard DA, Gustafsson MGL, et al. Subdiffraction multicolor imaging of the nuclear periphery with 3D structured illumination microscopy. *Science.* 2008;320(5881):1332–1336.
287. Chen F, Tillberg PW, Boyden ES. Optical imaging. Expansion microscopy. *Science.* 2015;347(6221):543–548.
288. Chozinski TJ, Halpern AR, Okawa H, Kim H-J, Tremel GJ, Wong ROL, Vaughan JC. Expansion microscopy with conventional antibodies and fluorescent proteins. *Nat Methods.* 2016;13(6):485–488.
289. Tillberg PW, Chen F, Piatkevich KD, Zhao Y, Yu C-CJ, English BP, Gao L, Martorell A, Suk H-J, Yoshida F, et al. Protein-retention expansion microscopy of cells and tissues labeled using standard fluorescent proteins and antibodies. *Nat Biotechnol.* 2016;34(9):987–992.

-
290. Ku T, Swaney J, Park J-Y, Albanese A, Murray E, Cho JH, Park Y-G, Mangena V, Chen J, Chung K. Multiplexed and scalable super-resolution imaging of three-dimensional protein localization in size-adjustable tissues. *Nat Biotechnol.* 2016;34(9):973–981.
291. Zwettler FU, Spindler M-C, Reinhard S, Klein T, Kurz A, Benavente R, Sauer M. Tracking down the molecular architecture of the synaptonemal complex by expansion microscopy. *Nat Commun.* 2020;11(1):3222.
292. Gambarotto D, Zwettler FU, Le Guennec M, Schmidt-Cernohorska M, Fortun D, Borgers S, Heine J, Schloetel J-G, Reuss M, Unser M, et al. Imaging cellular ultrastructures using expansion microscopy (U-ExM). *Nat Methods.* 2019;16(1):71–74.
293. Sun D, Fan X, Shi Y, Zhang H, Huang Z, Cheng B, Tang Q, Li W, Zhu Y, Bai J, et al. Click-ExM enables expansion microscopy for all biomolecules. *Nat Methods.* 2021;18(1):107–113.
294. Kim D, Kim T, Lee J, Shim S-H. Amplified Expansion Stimulated Emission Depletion Microscopy. *Chembiochem.* 2019;20(10):1260–1265.
295. Zwettler FU, Reinhard S, Gambarotto D, Bell TDM, Hamel V, Guichard P, Sauer M. Molecular resolution imaging by post-labeling expansion single-molecule localization microscopy (Ex-SMLM). *Nat Commun.* 2020;11(1):3388.
296. Chang J-B, Chen F, Yoon Y-G, Jung EE, Babcock H, Kang JS, Asano S, Suk H-J, Pak N, Tillberg PW, et al. Iterative expansion microscopy. *Nat Methods.* 2017;14(6):593–599.
297. Truckenbrodt S, Sommer C, Rizzoli SO, Danzl JG. A practical guide to optimization in X10 expansion microscopy. *Nat Protoc.* 2019;14(3):832–863.
298. Truckenbrodt S, Maidorn M, Crzan D, Wildhagen H, Kabatas S, Rizzoli SO. X10 expansion microscopy enables 25-nm resolution on conventional microscopes. *EMBO reports.* 2018;19(9):e45836.
299. Yu C-CJ, Barry NC, Wassie AT, Sinha A, Bhattacharya A, Asano S, Zhang C, Chen F, Hobert O, Goodman MB, et al. Expansion microscopy of *C. elegans*. *Elife.* 2020;9.
300. Gao R, Asano SM, Upadhyayula S, Pisarev I, Milkie DE, Liu T-L, Singh V, Graves A, Huynh GH, Zhao Y, et al. Cortical column and whole-brain imaging with molecular contrast and nanoscale resolution. *Science.* 2019;363(6424).
301. Nikić I, Estrada Girona G, Kang JH, Paci G, Mikhaleva S, Koehler C, Shymanska NV, Ventura Santos C, Spitz D, Lemke EA. Debugging Eukaryotic Genetic Code Expansion for Site-Specific Click-PAINT Super-Resolution Microscopy. *Angew Chem Int Ed Engl.* 2016;55(52):16172–16176.
302. Serfling R, Lorenz C, Etzel M, Schicht G, Böttke T, Mörl M, Coin I. Designer tRNAs for efficient incorporation of non-canonical amino acids by the pyrrolysine system in mammalian cells. *Nucleic Acids Res.* 2018;46(1):1–10.
303. Rimbault C, Maruthi K, Breillat C, Genuer C, Crespillo S, Puente-Muñoz V, Chamma I, Gauthereau I, Antoine S, Thibaut C, et al. Engineering selective competitors for the discrimination of highly conserved protein-protein interaction modules. *Nat Commun.* 2019;10(1):4521.
304. Polenghi A, Nieuws T, Guazzi S, Gorostiza P, Petrini EM, Barberis A. Kainate Receptor Activation Shapes Short-Term Synaptic Plasticity by Controlling Receptor Lateral Mobility at Glutamatergic Synapses. *Cell Reports.* 2020;31(10):107735.
305. Kaech S, Banker G. Culturing hippocampal neurons. *Nat Protoc.* 2006;1(5):2406–2415.
306. Schindelin J, Arganda-Carreras I, Frise E, Kaynig V, Longair M, Pietzsch T, Preibisch S, Rueden C, Saalfeld S, Schmid B, et al. Fiji: an open-source platform for biological-image analysis. *Nat Methods.* 2012;9(7):676–682.
307. Arganda-Carreras I, Sorzano COS, Marabini R, Carazo JM, Ortiz-de-Solorzano C, Kybic J. Consistent and Elastic Registration of Histological Sections Using Vector-Spline Regularization. In: Hutchison D, Kanade T, Kittler J, Kleinberg JM, Mattern F, Mitchell JC, Naor M, Nierstrasz O, Pandu Rangan C, Steffen B, et al., editors. *Computer Vision Approaches to Medical Image Analysis*. Vol. 4241. Berlin, Heidelberg: Springer Nature; 2006. p. 85–95 (Lecture Notes in Computer Science).

-
308. Bessa-Neto D, Kuhlemann A, Beliu G, Pecoraro V, Doose S, Retailleau N, Chevrier N, Perrais D, Sauer M, Choquet D. Bioorthogonal labeling of transmembrane proteins with non-canonical amino acids allows access to masked epitopes in live neurons. *bioRxiv*. 2021.
309. Twomey EC, Yelshanskaya MV, Grassucci RA, Frank J, Sobolevsky AI. Elucidation of AMPA receptor-stargazin complexes by cryo-electron microscopy. *Science*. 2016;353(6294):83–86.
310. Tomita S, Fukata M, Nicoll RA, Brecht DS. Dynamic interaction of stargazin-like TARPs with cycling AMPA receptors at synapses. *Science*. 2004;303(5663):1508–1511.
311. Louros SR, Caldeira GL, Carvalho AL. Stargazin Dephosphorylation Mediates Homeostatic Synaptic Downscaling of Excitatory Synapses. *Front Mol Neurosci*. 2018;11:328.
312. Bats C, Groc L, Choquet D. The interaction between Stargazin and PSD-95 regulates AMPA receptor surface trafficking. *Neuron*. 2007;53(5):719–734.
313. Fukaya M, Tsujita M, Yamazaki M, Kushiya E, Abe M, Akashi K, Natsume R, Kano M, Kamiya H, Watanabe M, et al. Abundant distribution of TARP gamma-8 in synaptic and extrasynaptic surface of hippocampal neurons and its major role in AMPA receptor expression on spines and dendrites. *Eur J Neurosci*. 2006;24(8):2177–2190.
314. Inamura M, Itakura M, Okamoto H, Hoka S, Mizoguchi A, Fukazawa Y, Shigemoto R, Yamamori S, Takahashi M. Differential localization and regulation of stargazin-like protein, gamma-8 and stargazin in the plasma membrane of hippocampal and cortical neurons. *Neurosci Res*. 2006;55(1):45–53.
315. Schnell E, Sizemore M, Karimzadegan S, Chen L, Brecht DS, Nicoll RA. Direct interactions between PSD-95 and stargazin control synaptic AMPA receptor number. *Proc Natl Acad Sci U S A*. 2002;99(21):13902–13907.
316. Waterhouse A, Bertoni M, Bienert S, Studer G, Tauriello G, Gumienny R, Heer FT, Beer TAP de, Rempfer C, Bordoli L, et al. SWISS-MODEL: homology modelling of protein structures and complexes. *Nucleic Acids Res*. 2018;46(W1):W296–W303.
317. Luca E de, Ravasenga T, Petrini EM, Polenghi A, Nieuws T, Guazzi S, Barberis A. Inter-Synaptic Lateral Diffusion of GABAA Receptors Shapes Inhibitory Synaptic Currents. *Neuron*. 2017;95(1):63–69.e5.
318. Crosby KC, Gookin SE, Garcia JD, Hahn KM, Dell'Acqua ML, Smith KR. Nanoscale Subsynaptic Domains Underlie the Organization of the Inhibitory Synapse. *Cell Rep*. 2019;26(12):3284–3297.e3.
319. Dalmau J, Geis C, Graus F. Autoantibodies to Synaptic Receptors and Neuronal Cell Surface Proteins in Autoimmune Diseases of the Central Nervous System. *Physiol Rev*. 2017;97(2):839–887.
320. Schnell U, Dijk F, Sjollem KA, Giepmans BNG. Immunolabeling artifacts and the need for live-cell imaging. *Nat Methods*. 2012;9(2):152–158.
321. Olsen RW, Sieghart W. International Union of Pharmacology. LXX. Subtypes of gamma-aminobutyric acid(A) receptors: classification on the basis of subunit composition, pharmacology, and function. Update. *Pharmacol Rev*. 2008;60(3):243–260.
322. Fisher JL, Macdonald RL. The Role of an α Subtype M 2 -M 3 His in Regulating Inhibition of GABA A Receptor Current by Zinc and Other Divalent Cations. *J Neurosci*. 1998;18(8):2944–2953.
323. Yoon KW, Covey DF, Rothman SM. Multiple mechanisms of picrotoxin block of GABA-induced currents in rat hippocampal neurons. *J Physiol*. 1993;464:423–439.
324. Kang J-Y, Kawaguchi D, Coin I, Xiang Z, O'Leary DDM, Slesinger PA, Wang L. In vivo expression of a light-activatable potassium channel using unnatural amino acids. *Neuron*. 2013;80(2):358–370.
325. Bader AN, Hofman EG, Voortman J, van en Henegouwen PMPB, Gerritsen HC. Homo-FRET imaging enables quantification of protein cluster sizes with subcellular resolution. *Biophys J*. 2009;97(9):2613–2622.
326. Westermarck J, Ivaska J, Corthals GL. Identification of protein interactions involved in cellular signaling. *Mol Cell Proteomics*. 2013;12(7):1752–1763.

327. Yasuda R. Imaging spatiotemporal dynamics of neuronal signaling using fluorescence resonance energy transfer and fluorescence lifetime imaging microscopy. *Curr Opin Neurobiol.* 2006;16(5):551–561.
328. Wyeth MS, Pelkey KA, Yuan X, Vargish G, Johnston AD, Hunt S, Fang C, Abebe D, Mahadevan V, Fisahn A, et al. Neto Auxiliary Subunits Regulate Interneuron Somatodendritic and Presynaptic Kainate Receptors to Control Network Inhibition. *Cell Reports.* 2017;20(9):2156–2168.
329. Neumann H, Wang K, Davis L, Garcia-Alai M, Chin JW. Encoding multiple unnatural amino acids via evolution of a quadruplet-decoding ribosome. *Nature.* 2010;464(7287):441–444.
330. Klein RL, Meyer EM, Peel AL, Zolotukhin S, Meyers C, Muzyczka N, King MA. Neuron-specific transduction in the rat septohippocampal or nigrostriatal pathway by recombinant adeno-associated virus vectors. *Exp Neurol.* 1998;150(2):183–194.
331. Rackham O, Chin JW. A network of orthogonal ribosome x mRNA pairs. *Nat Chem Biol.* 2005;1(3):159–166.
332. Wang K, Neumann H, Peak-Chew SY, Chin JW. Evolved orthogonal ribosomes enhance the efficiency of synthetic genetic code expansion. *Nat Biotechnol.* 2007;25(7):770–777.
333. Lajoie MJ, Rovner AJ, Goodman DB, Aerni H-R, Haimovich AD, Kuznetsov G, Mercer JA, Wang HH, Carr PA, Mosberg JA, et al. Genomically recoded organisms expand biological functions. *Science.* 2013;342(6156):357–360.
334. Willems J, Jong APH de, Scheefhals N, Mertens E, Catsburg LAE, Poorthuis RB, Winter F de, Verhaagen J, Meye FJ, MacGillavry HD. ORANGE: A CRISPR/Cas9-based genome editing toolbox for epitope tagging of endogenous proteins in neurons. *PLoS Biol.* 2020;18(4):e3000665.
335. Vaughan JC, Dempsey GT, Sun E, Zhuang X. Phosphine quenching of cyanine dyes as a versatile tool for fluorescence microscopy. *J Am Chem Soc.* 2013;135(4):1197–1200.
336. Wen G, Vanheusden M, Acke A, Valli D, Neely RK, Leen V, Hofkens J. Evaluation of Direct Grafting Strategies via Trivalent Anchoring for Enabling Lipid Membrane and Cytoskeleton Staining in Expansion Microscopy. *ACS Nano.* 2020;14(7):7860–7867.
337. Spatola M, Petit-Pedrol M, Simabukuro MM, Armangue T, Castro FJ, Barcelo Artigues MI, Julià Benique MR, Benson L, Gorman M, Felipe A, et al. Investigations in GABAA receptor antibody-associated encephalitis. *Neurology.* 2017;88(11):1012–1020.
338. Guo C-Y, Gelfand JM, Geschwind MD. Anti-gamma-aminobutyric acid receptor type A encephalitis: a review. *Curr Opin Neurol.* 2020;33(3):372–380.
339. June CH, O'Connor RS, Kawalekar OU, Ghassemi S, Milone MC. CAR T cell immunotherapy for human cancer. *Science.* 2018;359(6382):1361–1365.
340. Pan H, Li W, Chen Z, Luo Y, He W, Wang M, Tang X, He H, Liu L, Zheng M, et al. Click CAR-T cell engineering for robustly boosting cell immunotherapy in blood and subcutaneous xenograft tumor. *Bioactive Materials.* 2021;6(4):951–962.
341. Wang Y, Zhang C, Wu H, Feng P. Activation and Delivery of Tetrazine-Responsive Bioorthogonal Prodrugs. *Molecules.* 2020;25(23).
342. Wu K, Yee NA, Srinivasan S, Mahmoodi A, Zakharian M, Mejia Oneto JM, Royzen M. Click activated prodrugs against cancer increase the therapeutic potential of chemotherapy through local capture and activation. *Chem. Sci.* 2021;12(4):1259–1271.

7 Appendix

List of primers

Table 9 – Primers for introduction of TAG-click sites into GluK2 subunits of KARs by site-directed mutagenesis

| Primer GluK2 | Sequence (5' - 3') |
|-----------------|---|
| forward-S47TAG | GTATATTTGAATATGTGGAATAGGGCCCCATGGGAGCAG |
| reverse-S47TAG | CTGCTCCCATGGGGCCCTATTCCACATATTCAAATATAC |
| forward-S272TAG | GAGCCCTACAGATACTAGGGCGTAAATATGACAGG |
| reverse-S272TAG | CCTGTCATATTTACGCCCTAGTATCTGTAGGGCTC |
| forward-S309TAG | CCTCCAAAACCTGACTAGGGTTTGCTGGATGGATTTATG |
| reverse-S309TAG | CATAAATCCATCCAGCAAACCCTAGTCAGGTTTGGAGG |
| forward-S343TAG | CCAGATGACAGTCTAGTCCTTGCAATGCAATCGAC |
| reverse-S343TAG | GTCGATTGCATTGCAAGGACTAGACTGTCATCTGG |

Table 10 - Primers for introduction of TAG-click sites into TARP γ 2 and γ 8 by site-directed mutagenesis

| Primer γ 2 TARP | Sequence (5' - 3') |
|------------------------|--|
| forward-S44TAG | GGGTTTGCAAGACCAAATAGGTCAGTGAGAATGAAACC |
| reverse-S44TAG | GGTTTCATTCTCACTGACCTATTTGGTCTTGCAAACCC |
| forward-S51TAG | GTGTCAGTGAGAATGAAACCTAGAAAAAGAACGAGGAAGTTATG |
| reverse-S51TAG | CATAACTTCCTCGTTCTTTTTCTAGGTTTCATTCTCACTGACAC |
| forward-S61TAG | GGAAGTTATGACCCATTAGGGATTATGGAGAACCTGC |
| reverse-S61TAG | GCAGGTTCTCCATAATCCCTAATGGGTCATAACTTCC |
| Primer γ 8 TARP | Sequence (5' - 3') |
| forward-S72TAG | GTGGGGGCAGTGGCTAGTCAGAGAAGAAGGAC |
| reverse- S72TAG | GTCCTTCTTCTCTGACTAGCCACTGCCCCAC |
| forward-S84TAG | GCCTCACACATTAGGGCCTCTGGCGGATATG |
| reverse-S84TAG | CATATCCGCCAGAGGCCCTAATGTGTGAGGC |
| forward-K102TAG | GAGGTGTCTGCGTGTAGATCAACCACTTCCC |
| reverse-K102TAG | GGGAAGTGGTTGATCTACACGCAGACACCTC |

Table 11 - Primers for introduction of TAG-click sites into GABA-AR α -subunits by site-directed mutagenesis

| Primer $\alpha 2$ GABA-AR | Sequence (5' - 3') |
|---------------------------|---|
| forward-K73TAG | GGAAAGATGAACGTTTAAAATTTTAGGGTCCTATGAATATCCT TCGAC |
| reverse- K73TAG | GTCGAAGGATATTCATAGGACCCTAAAATTTTAAACGTTTCATC TTTCC |
| forward-S171TAG | CTTATATTTGGACTTACAATGCATAGGATTCAGTACAGGTTGC TC |
| reverse-S171TAG | GAGCAACCTGTACTGAATCCTATGCATTGTAAGTCCAAATATA AG |
| forward-S173TAG | GACTTACAATGCATCTGATTAGGTACAGGTTGCTCCTGATG |
| reverse-S173TAG | CATCAGGAGCAACCTGTACCTAATCAGATGCATTGTAAGTC |
| forward-S181TAG | CAGGTTGCTCCTGATGGCTAGAGGTTAAATCAATATGAC |
| reverse- S181TAG | GTCATATTGATTTAACCTCTAGCCATCAGGAGCAACCTG |
| forward-S201TAG | CGGAAAGGAGACAATTAATCCTAGACAGGTGAATATACTGT AATG |
| reverse-S201TAG | CATTACAGTATATTCACCTGTCTAGGATTTAATTGTCTCCTTTC CG |
| forward-K274TAG | GAATTCTCTCCCCTAGGTGGCTTATGCAAC |
| reverse-K274TAG | GTTGCATAAGCCACCTAGGGGAGAGAATTC |
| Primer $\alpha 1$ GABA-AR | Sequence (5' - 3') |
| forward-K73TAG | GATGAAAGATTA AAAATTCTAGGGACCCATGACAGTGCTC |
| reverse- K73TAG | GAGCACTGTCATGGGTCCCTAGAATTTTAATCTTTCATC |
| forward-A171TAG | GACCAGAGAGCCATAGCGTTCAGTGGTTGTAG |
| reverse-A171TAG | CTACAACCACTGAACGCTATGGCTCTCTGGTC |
| forward-S173TAG | GAGAGCCAGCCGTTAGGTGGTTGTAGCAG |
| reverse-S173TAG | CTGCTACAACCACCTAACGGGCTGGCTCTC |
| forward-S181TAG | GTTGTAGCAGAAGATGGGTAGCGTTTAAACCAGTATGAC |
| reverse- S181TAG | GTCATACTGGTTTAAACGCTACCCATCTTCTGCTACAAC |
| forward-S201TAG | CTCTGGAATTGTTCACTCCTAGACTGGAGAATATGTGGTTATG |
| reverse-S201TAG | CATAACCACATATTCTCCAGTCTAGGACTGAACAATCCAGAG |
| forward-K274TAG | GAAATTCCCTCCCGTAGGTGGCTTATGCAAC |
| reverse-K274TAG | GTTGCATAAGCCACCTACGGGAGGGAATTC |

Table 12 - Primers for introduction of TAG-click sites into NL2by site-directed mutagenesis

| Primer NL2 | Sequence (5' - 3') |
|-----------------|--|
| forward-E61TAG | GAGCTCAACAACCTAGATCCTGGGCCCCG |
| reverse-E61TAG | CGGGCCCAGGATCTAGTTGTTGAGCTC |
| forward-A113TAG | GAACCTGCACGGGTAGCTGCCGGCCATC |
| reverse-A113TAG | GATGGCCGGCAGCTACCCGTGCAGGTTC |
| forward-Q227TAG | CTTTCTCAGCACTGGTGACTAGGCTGCAAAGGCAACTAC |
| reverse-Q227TAG | GTAGTTGCCTTTTGCAGCCTAGTCACCAGTGCTGAGAAAG |

List of abbreviations

| | |
|------------------------|---|
| Ac ₄ GalNAz | N-azidoacetylgalactosamine-tetraacylated |
| Ac ₄ ManNAz | N-azidoacetylmannosamine-tetraacylated |
| AcX | 6-((acryloyl)amino)hexanoic acid - succinimidyl ester |
| AMPA | α -amino-3-hydroxy-5-methyl-4-isoxazolepropionic acid receptor |
| ATD | amino-terminal domain |
| BCN | biclononyne |
| BG | Benzylguanine |
| BSA | Bovine serum albumin |
| CaMKII | calcium/calmodulin-dependent protein kinase II |
| CAR | chimeric antigen receptor |
| Cb | collybistin |
| CCD | charged coupled device |
| click-ExM | click expansion microscopy |
| CLSM | confocal laser scanning microscope |
| CMV | Human cytomegalovirus |
| CNS | central nervous system |
| CoA | coenzyme-A |
| CTD | c-terminal domain |
| DAPI | 4',6-diamidino-2-phenylindole |
| DBSCAN | density-based spatial clustering of applications with noise |
| DIPEA | Diisopropylethylamine |
| DIV | days in vitro |
| DMEM | Dulbecco's Modified Eagle's Medium |
| DMSO | dimethylsulfoxide |
| DNA | deoxyribonucleic acid |
| dNTP | deoxynucleotid triphosphate |
| DOL | degree of labeling |
| DRD2 | dopamine receptor D2 |
| dSTORM | <i>direct</i> stochastic optical reconstruction microscopy |
| ECD | extracellular domain |
| ECH | extracellular helix |

| | |
|---------|---|
| EM | electron microscopy |
| EPSC | excitatory postsynaptic currents |
| FA | formaldehyde |
| Fab | fragment antigen binding |
| Fc | fragment crystallizable |
| FLIM | fluorescence lifetime imaging |
| FRAP | fluorescence recovery after photobleaching |
| FRET | fluorescence resonance energy transfer |
| GA | glutaraldehyde |
| GABA-AR | γ -aminobutyric acid type A receptor |
| GABA-BR | γ -aminobutyric acid type B receptor |
| GCE | genetic code expansion |
| GFP | green fluorescent protein |
| GHSR1a | Growth hormone secretagogue receptor 1a |
| HA | hemagglutinin |
| HC | heavy chain |
| HF | high-fidelity |
| IC | internal conversion |
| iGluRs | ionotropic glutamate receptors |
| IPSC | inhibitory postsynaptic currents |
| KAR | kainate receptor |
| LBD | ligand binding domain |
| LC | light chain |
| LTD | long-term depression |
| LTP | long-term potentiation |
| MEA | β -mercaptoethylamine |
| MF | mossy fibers |
| mGluRs | metabotropic glutamate receptors |
| NHS | N-hydroxysuccinimide |
| NL2 | neuroligin 2 |
| NMDAR | N-methyl-D-aspartate receptor |
| NRXN | neurexin |
| PALM | photoactivated localization microscopy |
| PBS | phosphate buffered saline |

| | |
|---------------------|---|
| PDB | protein data base |
| PDF | probability density function |
| PKC | protein kinase C |
| PLC | phospholipase C |
| PSD95 | postsynaptic density protein 95 |
| PylRS | pyrrolysyl-tRNA synthetase |
| Pyr | pyrimidyl |
| ROI | region of interest |
| RT | room temperature |
| scFv | short chain variable fragment |
| SIM | structured illumination microscope |
| SMLM | single molecule localization microscopy |
| SPAAC | strain-promoted alkyne-azide cycloaddition |
| SPIEDAC | strain-promoted inverse-electron demand Diels-Alder cycloaddition |
| S-SCAM | synaptic scaffolding molecule |
| STED | stimulated emission depletion |
| TARP | transmembrane-AMPA-regulatory-protein |
| TCO*-K | trans-cyclo-octene coupled lysine |
| Tet | tetrazine |
| TMD | transmembrane domain |
| tRNA ^{Pyl} | pyrrolysyl-tRNA |
| uAA | unnatural amino acid |
| WT | wildtype |

List of publications

FIRST AUTHORSHIP

(#) Diogo Bessa-Neto*, **Alexander Kuhlemann***, Gerti Beliu*, Valeria Pecoraro, Sören Doose, Natacha Retailleau, Nicolas Chevrier, David Perrais, Markus Sauer, Daniel Choquet. Bioorthogonal labeling of transmembrane proteins with non-canonical amino acids allows access to masked epitopes in live neurons (2021). *BioRxiv*. <https://doi.org/10.1101/2021.02.27.433189>. (*co-first authors)

(#) **Alexander Kuhlemann***, Gerti Beliu*, Dieter Janzen, Enrica Maria Petrini, Sören Doose, Martina Bruno, Andrea Barberis, Carmen Villmann, Markus Sauer, Christian Werner. Genetic code expansion and click-chemistry labeling to visualize GABA-A receptors by super-resolution microscopy (2021). (under review) (* co-first authors)

CO-AUTHORSHIP

Gerti Beliu, Steffen Altrichter, Ramon Guixà-González, Mareike Hemberger, Ina Brauer, Anne-Kristin Dahse, Nicole Scholz, Robert Wieduwild, **Alexander Kuhlemann**, Hossein Batebi, Florian Seufert, Guillermo Pérez-Hernández, Peter W Hildebrand, Markus Sauer, Tobias Langenhan. Tethered agonist exposure in intact adhesion/class B2 GPCRs through intrinsic structural flexibility of the GAIN domain (2021). *Molecular Cell*. <https://doi.org/10.1016/j.molcel.2020.12.042>.

(#) Gerti Beliu, Andreas J. Kurz, **Alexander C. Kuhlemann**, Lisa Behringer-Pliess, Mara Meub, Natalia Wolf, Jürgen Seibel, Zhen-Dan Shi, Martin Schnermann, Jonathan B. Grimm, Luke D. Lavis, Sören Doose & Markus Sauer. Bioorthogonal labeling with tetrazine-dyes for super-resolution microscopy (2019). *Communications Biology*. <https://doi.org/10.1101/2021.02.27.433189>.

Charlene Börtlein, Annette Draeger, Roman Schoenauer, **Alexander Kuhlemann**, Markus Sauer, Sibylle Schneider-Schaulies, Elita Avota. The Neutral Sphingomyelinase 2 Is Required to Polarize and Sustain T Cell Receptor Signaling. (2018). *Front. Immunol.* <https://doi.org/10.3389/fimmu.2018.00815>.

(#) **publication is associated with the dissertation.**

Acknowledgements

I want to thank all the colleagues, friends and collaboration partners who supported me throughout my dissertation:

First, I want to thank Prof. Dr. Markus Sauer, who gave me the opportunity to conduct my dissertation at his department. Your optimism and candor helped me to stay on track and encouraged me. I am fascinated by your leadership, which is not only based on knowledge but also on friendship and fun. I am grateful for your supervision.

I thank Prof. Dr. med. Anna Leena Sirén, who consented to be my second supervisor, for supervision during my dissertation and the valuable input and discussions at the annual reports.

I want to thank PD Dr. Sören Doose for all the help with cluster analysis and your support concerning the GABA-AR and TARP projects or any other questions.

I especially thank Dr. Gerti Beliu for introducing me to the field of bioorthogonal labeling. Thank you for your patience and time. Your continuous drive to push this field of science inspired and motivated me.

I thank Dr. Christian Werner for all the help concerning neurobiological questions, for valuable discussions and collaboration on the GABA-AR project.

I want to thank Dominic Helmerich and Danush Taban for the cooperation on multimeric receptors.

I thank Prof. Dr. Carmen Villmann and Dieter Janzen for their support with electrophysiological experiments in the GABA-AR project.

I thank Prof. Dr. Daniel Choquet and Diogo Neto for the great collaboration on clickable TARPs and the research stay at the CNRS in Bordeaux.

I thank Dr. Andrea Barberis and Dr. Enrica Petrini for the support with the GABA-AR project and the research stay at the IIT in Genova.

I thank my family and my girlfriend Laura for their constant support and love.

Finally, I am grateful for all the people at the Department of Biotechnology and Biophysics. Due to the great team mentality, it was always fun working with you and over the years I made numerous friends at the department.

Affidavit

Eidesstattliche Erklärungen nach §7 Abs. 2 Satz 3, 4, 5 der Promotionsordnung der Fakultät für Biologie

Eidesstattliche Erklärung

Hiermit erkläre ich an Eides statt, die Dissertation: „**Bioorthogonale Markierung von neuronalen Proteinen mittels hochauflösender Fluoreszenzmikroskopie**“, eigenständig, d. h. insbesondere selbständig und ohne Hilfe eines kommerziellen Promotionsberaters, angefertigt und keine anderen, als die von mir angegebenen Quellen und Hilfsmittel verwendet zu haben. Ich erkläre außerdem, dass die Dissertation weder in gleicher noch in ähnlicher Form bereits in einem anderen Prüfungsverfahren vorgelegen hat. Weiterhin erkläre ich, dass bei allen Abbildungen und Texten bei denen die Verwertungsrechte (Copyright) nicht bei mir liegen, diese von den Rechtsinhabern eingeholt wurden und die Textstellen bzw. Abbildungen entsprechend den rechtlichen Vorgaben gekennzeichnet sind sowie bei Abbildungen, die dem Internet entnommen wurden, der entsprechende Hypertextlink angegeben wurde.

Affidavit

I hereby declare that my thesis entitled: „**Bioorthogonal labeling of neuronal proteins using super-resolution fluorescence microscopy**” is the result of my own work. I did not receive any help or support from commercial consultants. All sources and / or materials applied are listed and specified in the thesis. Furthermore I verify that the thesis has not been submitted as part of another examination process neither in identical nor in similar form. Besides, I declare that if I do not hold the copyright for figures and paragraphs, I obtained it from the rights holder and that paragraphs and figures have been marked according to law or for figures taken from the internet the hyperlink has been added accordingly.

Würzburg, den _____

Alexander Kuhlemann

Curriculum Vitae

PERSONAL DATA

Name Alexander Kuhlemann
Date of Birth: 31.01.1993
Place of Birth: Bamberg
Nationality: German

EDUCATION

- 12/2016 - Present** **PhD Student, Biology**
University of Wuerzburg
Department of Biotechnology and Biophysics
- Advancing new labeling strategies for super-resolution microscopy using unnatural amino acids and click chemistry
 - Application of click chemistry on relevant targets in neuroscience and oncology
 - Addressing multimeric organization of receptors by combination of click chemistry with Expansion Microscopy
- 10/2014 – 11/2016** **Master of Science, Biology**
University of Wuerzburg, degree M.Sc. (1.2)
Thesis at the Department of Biotechnology and Biophysics
- Characterization of CD molecules on human T lymphocytes (CD3) and fibrosarcoma cells (CD120a)
 - Interdisciplinary collaboration with leading scientist in the fields of molecular internal medicine and virology
- 10/2011 – 08/2014** **Bachelor of Science, Biology**
University of Wuerzburg, degree B.Sc. (2.0)
Thesis at the Department of Structural Biology
- Biochemical characterization of human cystathionase
 - Interdisciplinary cooperation with leading researchers in biochemical oncology
- 09/2003 – 06/2011** **General higher education entrance qualification**
Clavius Gymnasium Bamberg